INVESTIGATION OF ADDITIVELY MANUFACTURED TI-6AL-4V AND TI-6AL-4V-TA ALLOYS LATTICE FOR LOAD-BEARING IMPLANT APPLICATION

Anel Zhumabekova, MSc.

Submitted in fulfillment of the requirements
for the degree of Master of Science
in Mechanical & Aerospace Engineering

School of Engineering and Digital Sciences
Department of Mechanical & Aerospace Engineering
Nazarbayev University

53 Kabanbay Batyr Avenue,
Astana, Kazakhstan, 010000

Supervisor: Associate Professor Didier Talamona
Co-supervisor: Associate Professor Asma Perveen

April 2024

DECLARATION

I hereby, declare that this manuscript, entitled “*INVESTIGATION OF ADDITIVELY MANUFACTURED TI-6AL-4V AND TI-6AL-4V-TA ALLOYS LATTICE FOR LOAD-BEARING IMPLANT APPLICATION*”, is the result of my own work except for quotations and citations, which have been duly acknowledged.

I also declare that, to the best of my knowledge and belief, it has not been previously or concurrently submitted, in whole or in part, for any other degree or diploma at Nazarbayev University or any other national or international institution.

_ _ _ _ _ _ _ _ _ _ _ _ _ _ _ _ _

Name: Anel Zhumabekova

Date: 05.04.2024

Abstract

Bone implants have been a critical solution for addressing bone defects and disorders, with recent advancements in Additive Manufacturing (AM) allowing for creating customized implants using materials like Titanium and its alloys. This study focuses on lattice structures manufactured through Selective Laser Melting (SLM) technology, exploring the mechanical properties and biocompatibility of Titanium alloys, specifically Ti–6Al–4V and Ti–6Al–4V–Ta, for potential use in load-bearing applications. The lattice structures aim to mimic natural bone architecture, offering improved strength-to-weight ratios and promoting osseointegration.

A comparison between Ti–6Al–4V and Ti–6Al–4V-Ta results is conducted, covering mechanical analysis, powder characterization, electrochemical corrosion, and biomedical compatibility. The literature review highlights the increasing interest in Ti-Ta alloys, especially in lattice structures, with a scarcity of research in this area.

The methodology encompasses powder characterization, lattice structure design, SLM process parameters, post-processing, and detailed characterization techniques. The mechanical analysis involves compression, tensile testing, and hardness measurements. Morphological analysis and crack investigation contribute to a comprehensive understanding of lattice structures. An electrochemical corrosion test checks corrosion resistance, which is essential for medical implant applications. Biomedical compatibility is assessed through measurements for bacterial adhesion on SLM-printed surfaces.

The research aims to bridge the gap in understanding Ti–6Al–4V–Ta alloys manufactured with SLM, providing insights into their mechanical properties and potential applications in load-bearing implants. The outcomes of this study contribute to advancing the field of additive manufacturing for biomedical applications, offering valuable data for the development of safer and more effective bone implants.

Acknowledgments

I sincerely appreciate my supervisors, Associate Professors Didier Talamona and Asma Perveen, for their excellent advice and assistance with this academic endeavor. Their knowledge and perception have been invaluable to my work. Extra gratitude is also owed to Malika Toleubekova, whose assistance was crucial to our achievement, and Professor Tri Pham for his essential contributions to the biocompatibility side of this thesis. Their joint knowledge and support have tremendously enhanced my academic career and shaped this thesis. Also, I would like to express my gratitude to all other RA's and the whole research team of our professors who shared this journey and helped during it. Nevertheless, I also appreciate the Ministry of Science and Higher Education of the Republic of Kazakhstan and Nazarbayev University for providing the opportunity to work under the thesis under the following grants: «SEDS2020007 Cost-effective hybrid casting methods for cellular structures», «Additive Manufacturing Systems and Metal Powders for the Kazakhstani industry OP2021004», «Design, fabrication & characterization of metal lattice structures using ultrasonically atomized powder OPCRP2024011».

Table of Contents

List of Abbreviations & Symbols

AM	Additive Manufacturing
EDS	Energy Dispersive Spectroscopy
FEA	Finite Element Analysis
SEM	Scanning Electron Microscopy
SLM	Selective Laser Melting
TPMS	Triply Periodic Minimal Surface
UCS	Unit Cell Size
F	Applied Force
A_0	Area of the lattice bounding box cross section
$\varDelta$	Traverse Displacement
h_0	Initial height of the lattice
σ	Stress
ε	Strain
ρ/ρ_s	Relative Density
σ_s	Yield Stress
σ_p	Plateau Stress
E	Elastic Modulus
ψ	Energy Absorption
η	Energy Absorption Efficiency
ε_d	Densification Strain of the lattice
i_{corr}(A/cm^2)	Current density
β	Stern Geary coefficient
Rp (Ohms/cm^2)	polarization resistance
R_S	solution resistance
C	charge capacitance

List of Tables

List of Figures

Chapter 1 – Introduction

1.1. Outline the problem/area of application

For many years, bone implants have been utilized to address bone defects and disorders. In the past decades, Additive Manufacturing has made it feasible to create customized and intricate implants closely matching a patient's anatomy [1]. Among all materials, Titanium and its alloys have outstanding biocompatibility, corrosion resistance, and a high strength-to-weight ratio, making them the preferred biomaterials for implants compared to other biomaterials such as stainless steel and Co-based alloys [1,2]. Furthermore, titanium alloys have also shown beneficial physiochemical properties. Titanium forms a protective layer that provides biocompatibility and corrosion resistance with an almost negligible corrosion rate in a physiological milieu [2]. It should be noted that numerous biomaterials, such as ceramics and polymers, are used to implant medical devices. However, the problem is that they are either excessively brittle or fail to provide the appropriate strength for load-bearing applications [3].

Ti–6Al–4V alloys are the most common applications in the biomedical field, which have Grades 5 and 23. The elastic modulus of these dense alloys is 113 GPa [4]. In contrast to them, the elastic modulus of human bone is 1.5 GPa for the trabecular bone and 30 GPa for the cortical bone [5, 6]. However, applying a lattice structure offers an advantageous combination of strength and weight. The interconnected lattice pattern distributes loads more evenly across the implant, mimicking the mechanical properties of natural bone. This feature reduces stress concentrations and the risk of implant failure due to excessive forces. For instance, in the study of Suresh et al. [7], the Elastic modulus of the dense and lattice parts was reported to be 120 GPa and 80 GPa, respectively.

A lattice structure is an ideal choice for designing to obtain mechanical properties like human bones. Nevertheless, lattice structures promote osseointegration compared to solid implants, when the bone grows and integrates with the implant. The porous nature of lattice structures allows for improved nutrient and oxygen flow, facilitating the infiltration of bone cells into the implant. This results in better bone ingrowth and long-term stability of the implant. It should be noted that incorporating a porous structure allows the implant to be lighter and use less material without compromising its integrity. This reduces manufacturing costs and makes the implant more biocompatible and less likely to cause adverse reactions. At some point, lattice implants could simplify the surgical procedure by providing improved visibility and accessibility during implant placement. Surgeons can use instruments like screws, wires, or sutures to secure the implant, taking advantage of the lattice's interconnected structure.

Manufacturing lattice titanium bone implants involves utilizing advanced technologies, typically 3D printers, to construct intricate lattice structures that imitate the natural architecture of bone tissue [1]. They make it possible to design implants customized to each patient, considering their anatomy and pathology. However, several additive manufacturing (AM) technologies are available. Among them, LPBF stands out as it offers better advantages in terms of machinery cost, printing accuracy, and mechanical properties. It plays an integral role in manufacturing the samples since implants need high accuracy when applied to the human body [4].

Nevertheless, mechanical properties should be good, in other words, equal or similar to the human bone [1, 4, 5]. That is why this investigation focuses on the LPBF type 3D printer. Moreover, one of the widespread and often used LPBF-based printers is Selective Laser Melting (SLM). The working principle of SLM and printed products is shown in Figure 1.1.

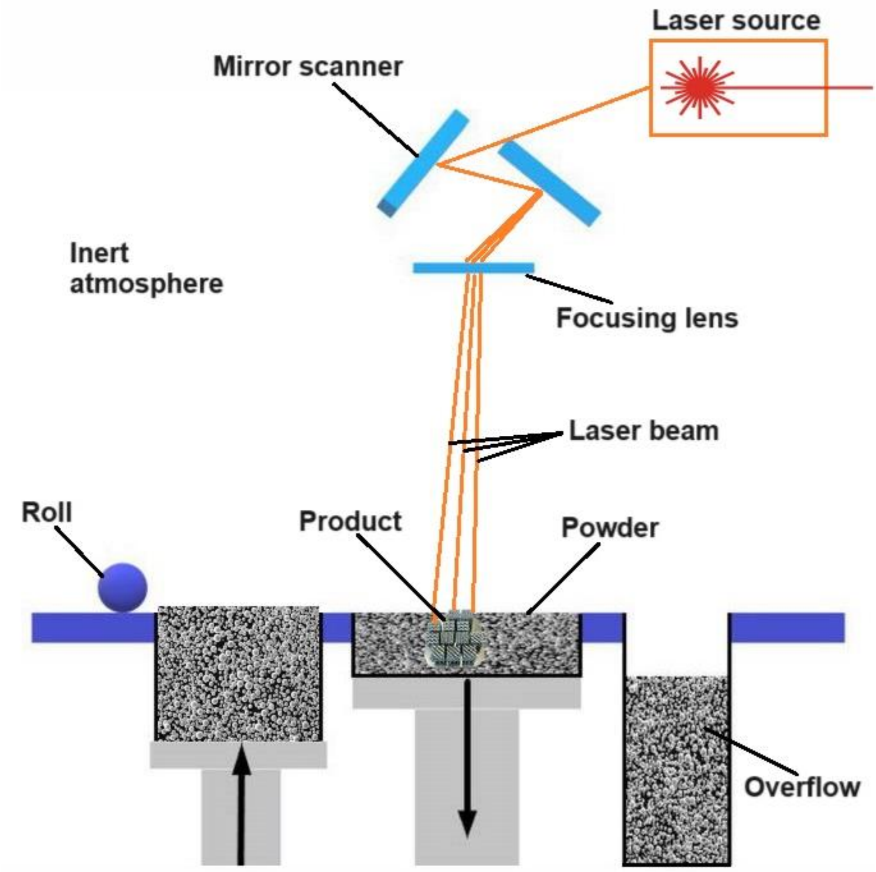

Figure 1.1: Working principle of Selective Laser Melting (SLM) technique.

As previously noted, Ti–6Al–4V alloys have a high strength-to-weight ratio and excellent corrosion resistance, which make them suitable for use in medical implant applications (Figure 1.2). While aluminum (Al) and vanadium (V) ions are widely accepted as industry standards, new research has raised serious concerns about their potential toxicity in the body [2, 3]. Instead of these harmful elements, alloying with Niobium (Nb), Tantalum (Ta), or Zirconium (Zr) has been attempted recently [4, 5, 6]. As a result, these materials have been found to perform better than Ti-6Al-4V, which has motivated researchers to create new biocompatible metals with different alloying components.

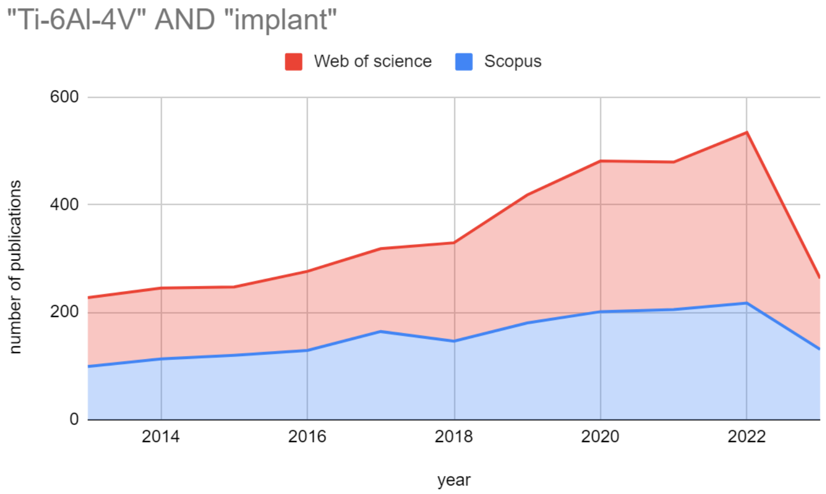

Figure 1.2: Annual number of publications on Ti-6Al-4V implants in recent years

Tantalum (Ta) is gaining interest because of its exceptional biocompatibility and excellent corrosion resistance; nonetheless, applications are confined to surface coatings due to its high cost and machining difficulty [7]. For biomedical applications, it is a promising alloying complement to pure titanium. When standard, irregular tantalum powders are utilized, mixing Ta and Ti powders is an effective technique to lower the material's cost and increase the flowability of the powder mixture [8]. Furthermore, tantalum can stabilize titanium's β, which is advantageous for biomedical applications (i.e., low modulus and high strength) [9]. Sing et al. [10] report that compared to commercially pure titanium (cp-Ti), titanium-tantalum (Ti–Ta) alloys exhibit higher relative strength (for comparable stiffness) and lower elastic modulus, as well as superior corrosion resistance and superior biocompatibility properties. As a result, the research interest in Ti-Ta implants has been growing significantly, as demonstrated by the number of publications published in journals indexed by Scopus and Web of Science, shown in Figure 1.3.

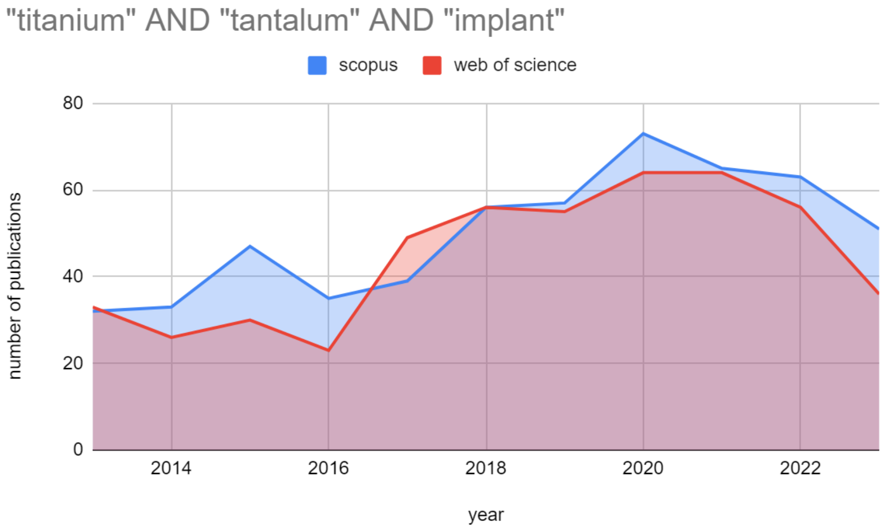

Figure 1.3: Annual number of publications on Ti-Ta implants in recent years

As shown in Figure 1.4, lattice structures can be divided into two categories based on their topology: strut-based lattice structures and Triply Periodic Minimal Surface-based structures—multiple struts connected at nodes in various orientations form strut-based cells. Different strut-based lattices, such as the BCC, BCCZ, FCC, FCCZ, rhombic dodecahedron, octet truss, and Kelvin, have been proposed in the literature. Adding or removing struts to or from the preexisting topologies can create new strut-based lattices. The connectedness of the lattices has a significant impact on the mechanical characteristics of strut-based lattices. The mechanical qualities of the strut-based lattices dramatically improve as the number of struts increases. Additionally, the mechanical performance of struts aligned with the loading direction is significantly improved [15], which compromises the isotropy.

a) Strut-based cellular structures

b) Skeletal-TPMS based cellular structures

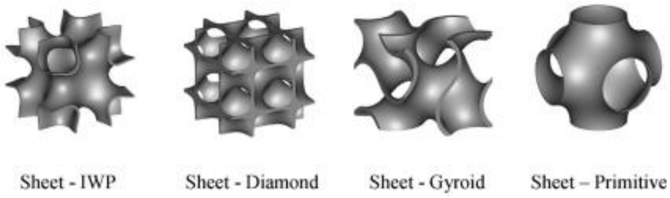

c) Sheet-TPMS based cellular structures

Figure 1.4: Classification of lattice structures by topology [16]

In general, triply periodic minimal surfaces (TPMS) have recently received significant interest as base geometries for the design of lattice structures [17]. The literature review around Ti-6Al-4V lattice structures shows that the Diamond structure exhibits the best overall performance in energy absorption, porosity, and stiffness, similar to human bones [18-23]. For this structure, an 80% porosity is recommended [24]. The gyroid structure is the most suitable for load-bearing bone replacement due to its high stiffness and porosity [24]. Primitive structure fulfills the requirements for tibia pore structure. It has superior mechanical properties, including a high elastic modulus and yield strength [23]. Finally, Structure C has a longer fatigue life than Structure D, indicating a longer product lifespan [21]. All four structures are suitable for designing lattice implants.

The mathematically generated surfaces with mean curvature equal to zero are used to build TPMS lattice structures. TPMS lattices with skeletal and sheet-based structures are then included in the classification. The mathematical surface is given thickness to create sheet-based TPMS cells. By encapsulating the volumes that TPMS surfaces produce, skeletal TPMS is generated. They can be created without support and have smoother geometry than strut-based lattices [26].

Even though additive manufacturing (AM) makes it easier to produce functioning lattice structures, most mechanical testing on lattice structures focuses on their compressive and impact properties. At the same time, there is far less focus on their tensile, shear, and fatigue characteristics. This is the main reason lattices deflect impact and absorb energy. Lattice deformation modes under compression can be divided into bending-dominated and stretch-dominated behavior. The stress-strain curves of the bending and stretch-dominated lattices are shown in Figure 1.5. The elastic deformation zone, which has a linear stress-strain relationship, initially precedes the plastic deformation zone. The behavior of lattices in the plastic deformation zone is characterized by stress fluctuations brought on by local layer-wise buckling failure of the struts. On the other hand, the bending-dominated lattices produce a smooth stress-strain profile due to the bending of the struts around their nodes. When neighboring layers encounter each other, the densification of the lattice occurs, and it starts to behave as a solid material.

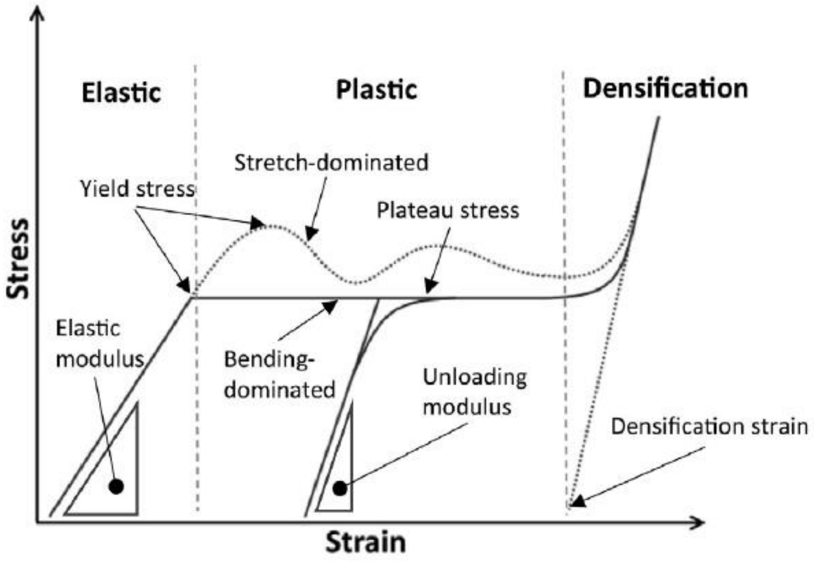

Figure 1.5: Deformation behaviours of stretch and bending dominated lattice structures [29]

When an individual is standing or walking, their entire upper body is supported by load-bearing bones, which comprise the sacrum and the lumbar area of the spine [30]. That is why the load can vary depending on factors such as body weight, activity level, and posture. During everyday activities like walking on level ground, the load on the femur is estimated to be around 2-3 times body weight [31]. For example, a person weighing 70 kilograms (154 pounds) would experience a compressive force on their femur of approximately 140-210 kilograms (308-462 pounds) during walking. It is important to note that this estimate can increase during activities that involve running, jumping, or other high-impact movements.

So, excessive body weight or obesity can increase the load on the load-bearing implant, potentially leading to increased stress on the bone and joints. On the other hand, physical conditioning, muscle strength, and proper alignment during movement can help distribute the load more evenly and reduce stress on the implant. Nevertheless, it is worth mentioning that these estimates are based on averages and can differ among individuals. Additionally, specific conditions such as osteoporosis or bone diseases can affect bone strength and alter the load-bearing capacity of the implant.

1.2. Research Aims and objectives

The research aims to estimate the mechanical properties of the triply periodic lattice structures (generated in MSLattice software) by Selective Laser Melting (SLM) machine to obtain mechanical properties closer to human being of lattice implant material of Ti-6Al-4V-Ta alloy. Also, an initial investigation will be conducted on Ti-6Al-4V to choose optimal density and cell size in MSLattice software for Ti-6Al-4V-Ta alloys. There are several objectives established to complete the aim of the project:

1. To study different alloying options (Ti-6Al-4V and Ti-6Al-4V-Ta).

Tasks: This section investigates the mechanical properties of identical specimens but with different powder compositions.

2. To study the powder characterization

Tasks: This section examines the powder size distribution investigation using Mastersizer and the chemical composition of the powders using SEM. After SEM, images of the powder will be included to check and demonstrate its spherical characteristics.

3. To study the mechanical performance, hardness test, and energy absorption characteristics of different lattice structures made of Ti-6Al-4V and Ti-6Al-4V-Ta alloys.

Tasks: This section identifies the elastic moduli, yield strengths, energy absorption values, and energy absorption efficiencies of various stretch and bending-dominated lattice structures. Lattice structures will be manufactured, their stresses will be relieved, and lattices will be tested under quasistatic compression with no additional heat treatment. The resulting properties will be compared with those of modified lattice structures. Different alloying options will also be explored here for Ti-6Al-4V -Ta.

4. To investigate the corrosion resistance of Ti-6Al-4V and Ti-6Al-4V-Ta alloys

Tasks: This test is intended to investigate the corrosion resistance of the alloys using OCP (Open Circuit Potential), EIS (Electrochemical Impedance Spectroscopy) vs frequency, and Potentiodynamic analysis.

5. To study the biomedical compatibility of Ti-6Al-4V and Ti-6Al-4V-Ta alloys.

Tasks: This part aims to use the adhesion of bacteria on the SLM-printed surface.

Chapter 2 – Literature Review

2.1 Overview

As far as the research was done using keywords from databases such as Scopus and Web of Science, there are no papers investigating lattice structures made of Ti-6Al-4V by adding Ta. However, there are three main works around SLM-printed lattice-structured Ti-Ta implants in Web of Science and Scopus. They all investigate mechanical performance and compatibility but with different weight ratios of materials. Two studies by Chua et al. [32, 33] investigate mechanical performance only using FEA analysis with the 1:1 weight ratio of pure Ti-Ta. However, another study by Soro et al. [1] uses 75% of pure Ti and 20% of pure Ta. The more Ta than Ti, the less value of mechanical properties. Also, regarding the design of the lattice structures, the two studies [32, 33] use FCC structure, as seen in Figure 2.1. In contrast, the study by Soro et al. [1] uses TPMS, to be precise, Schwartz's primitive unit cell (Figure 2.2).

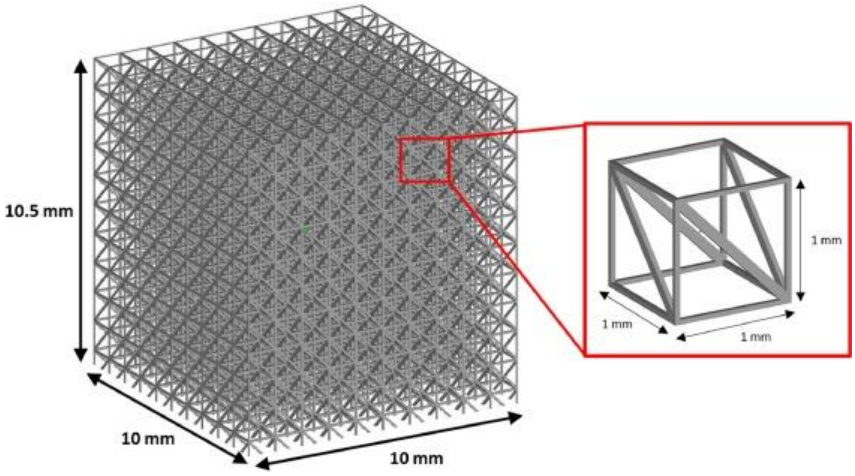

Figure 2.1: CAD file of cellular lattice structures [32].

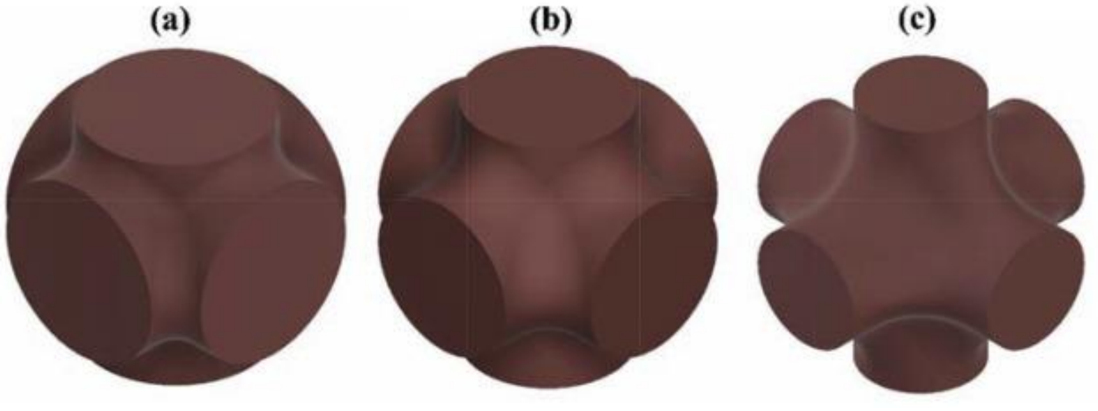

Figure 2.2: Schwartz primitive unit-cells used for the scaffolds models. (a) 25% porosity (b) 42% porosity and (c) 64% porosity [1].

Finite Element Analysis (FEA) is used in both studies [32, 33] to examine the mechanical characteristics of titanium-tantalum alloy lattice structures made by selective laser melting (SLM). ANSYS uses two methods to replicate and evaluate the geometry: the beam and full-3D models. While yield strength estimates are between 50% and 65% lower than experimental data, both models can reliably predict elastic modulus. The results of the full-3D FEA model are followed by the Gibson-Ashby model, which is utilized to validate design factors like porosity levels. In order to provide additional validation for the FEA model, full-3D simulations of uniform lattice structures with porosities ranging from 50% to 90% reveal that the mechanical properties closely match the Gibson-Ashby model. According to one research [32], the elastic modulus of the Ti-Ta lattice structure made with the in-situ alloying SLM technique may be effectively approximated by the current FEA models. Accurate yield strength prediction requires other parameters, such as residual stress and powder adhesion state. Another work [33] suggests investigating defect information, such as surface roughness and strut waviness, that may be retrieved from the experiment samples and used in the simulation models in order to further improve the forecast accuracy of the FEA models.

Soro et al.'s work [1] successfully used the selective laser melting technique to create innovative porous materials composed of a Ti–25Ta combination. In addition to compressive mechanical parameters, macrostructural and microstructural data were used to evaluate the process's manufacturability and repeatability. The titanium-tantalum combination shown here has much better ductility, which may be advantageous for surgical operations and improved implant adaptability. If the compression strength of the cortical bone (load-bearing bone) is 205±12.6 MPa, in this work with 42% density, the yield strength was 233 ± 2 MPa and 319 ± 8 MPa with 25% density. As a result, the suggested work will utilize a density of around 30% to obtain data closer to human bone.

Considering the works around Ti-6Al-4V-Ta, there is an investigation on applying Ti-6Al-4V by adding Ta with different weight ratios (0%, 2%, 4%, AND 6% of Ta) [34]. The results showed that strength and ductility increase when Ta is added to the Ti-6Al-4V alloy. The alloy Ti-6Al-4V–4Ta has a weaker selection of α-variants and the most consistent basketweave microstructure. A four percent weight addition of Ta significantly improves mechanical performance (UTS - 1042 MPa, YS - 956 MPa, and elongation - 10.8%) compared to Ti-6Al-4V–0Ta without Ta. The improved mechanical properties are ascribed to higher dislocation density, solid Ta element solution, weaker α-variants selection, and refined microstructure.

Table 2.1 represents the investigation results on the common lattice bone implant configurations, their properties made of Ti-6Al-4V. The table also includes the cell structures of the lattices to give an understanding of how they look. Cube (C), Diamond (D), Gyroid (G), and Primitive (P) are more widely studied cell structures.

Table 2.1: Common lattice bone implant configurations made of Ti-6Al-4V and their properties

№	Pore Size(µm)	Porosity (%)	Findings	Cell Structure
[35]	500 1000	65	Triangular (T) - more beneficial for cell growth & differentiation than the hexagonal (H). Rectangular (R) - lead to cell blockage.	
[36]	650	65	Diamond (D) - the most appropriate configuration for bone growth = least difference in fluid velocity, the longest path for flow, & promotes the development of blood vessels, nutrient transportation, & bone creation	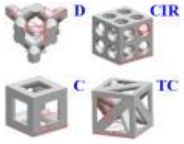
[37]	560–1600 480–1450	80–95	Gyroid (G) and Diamond (D) - higher porosity and stiffness than human bone.	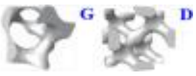
[38]	500-1000	-	Cube (C) - fatigue life greater than for Diamond (D); porosity can enhance its fatigue life. Triangular (T) - no exceptional characteristics.	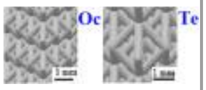
[39]	574 679 882	65	Gyroid (G) - optimal choice for bone substitute materials that bear weight; Body-centered cubic (BCC) - the highest level of permeability.	
[40]	600–1000	50–82	Primitive (P) - more resistable for deformation than Gyroid (G) and Diamond (D).	

Summarizing the represented table 2.1, structure D exhibits the best overall performance in terms of energy absorption, porosity, and stiffness, similar to human bones [35-40]. For structure D, an 80% porosity is recommended [41]. Structure G is the most suitable for load-bearing bone replacement due to its high stiffness and porosity [41]. Structure P fulfills the requirements for tibia pore structure and has superior mechanical properties, including a high elastic modulus and yield strength [40]. Structure C has a longer fatigue life than structure D, indicating a longer product lifespan [38]. All four structures are suitable for designing lattice implants.

Nevertheless, studies have shown that an optimal range of pore size and porosity exists to maximize lattice titanium bone implants' mechanical properties and biocompatibility. Selective laser melting (SLM) produces lattice implants with improved bone ingrowth performance at a porosity level of 60% to 70% and a pore size of 500 to 700 µm. In contrast, some authors state that a range of 300-600 µm pore size and 50-70% porosity has been reported as ideal for promoting bone ingrowth, osseointegration (structural-functional connection of bones and implants), and mechanical stability [40,42-43]. However, the optimal range may vary depending on the specific application and patient needs. That is why there is still a necessity in the investigation of the optimal mechanical and morphological characteristics of lattice implants.

2.2 Research gap identification

In summary, there is not much literature on Ti–Ta alloys produced overall using SLM (Figure 2.3), and examining the databases of Scopus and Web of Science using specific keywords yields no findings regarding SLM-printed lattice structures made of Ti-6Al-4V. The impact of SLM settings on the mechanical characteristics and part quality of a dense Ti–50Ta alloy (containing 50% of both Ti and Ta) has been documented by Sing et al. [8, 10]. In comparison to cp-Ti and Ti-6Al-4V parts, the tantalum particles demonstrated notable densification and good mechanical characteristics, despite difficulties in totally melting them. Printing parameter handling (e.g., laser power and scanning speed) affected the mechanical properties and dimensional accuracy.

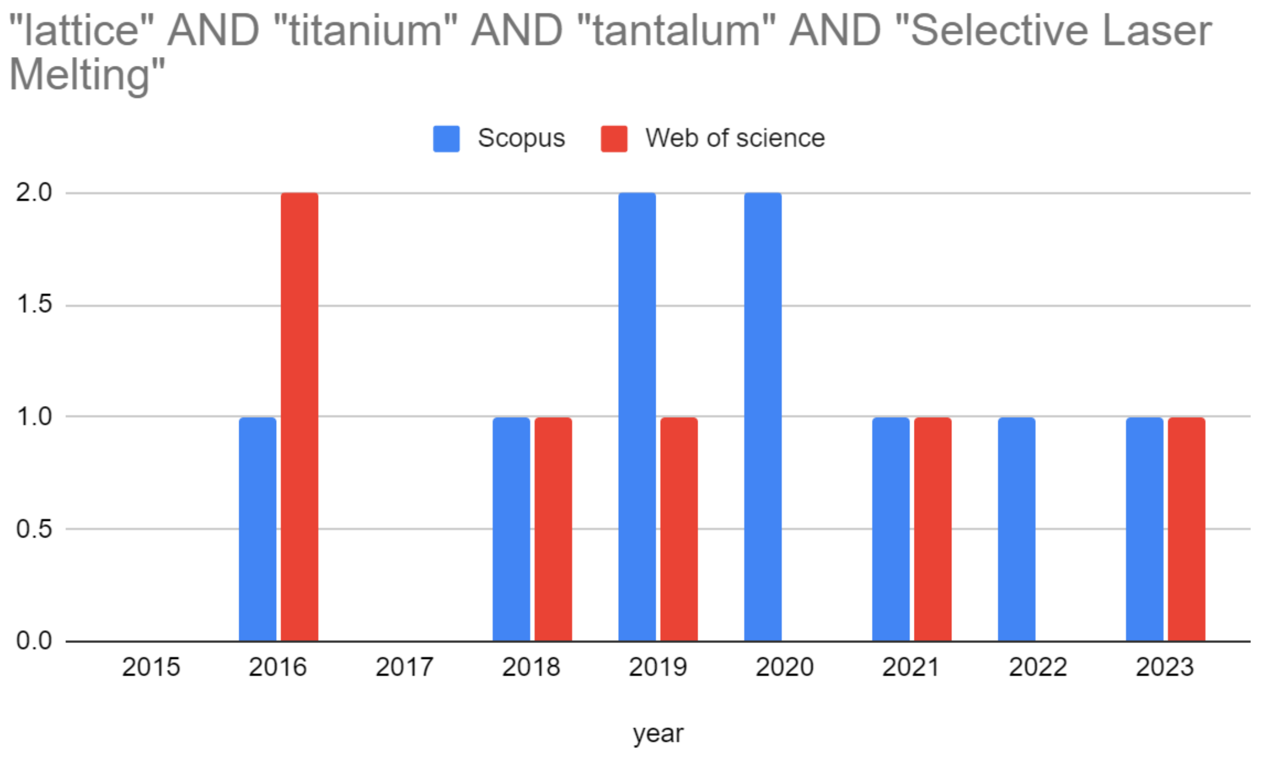

Figure 2.3: Annual number of publications on Additively manufactured lattice Ti-Ta implants in recent years

However, there has also been a study on SLM-printed pure tantalum, and highly porous tantalum implants have been created [44]. Tantalum exhibits good mechanical response and biocompatibility, as confirmed by investigations into mechanical qualities and the in-vivo reaction in a rat femur design. On the other hand, applying pure tantalum to implants the size of humans is thought to be a costly alternative. As a result, it is better to investigate the mixture of Ti-Ta powders. At the same time, it is possible to modify the properties of the metals by heat treatment. Reviewing that, the effect of heat treatment on mechanical properties of lattice structures produced from Ti-Ta alloy needed to be better studied.

Chapter 3 – Methodology

3.1 Overview

This section covers powder characterization, the design and manufacturing processes for the chosen material, mechanical analysis and characterization for printed and tested, corrosion resistance, and bacteria adhesion methodology for Ti-6AL-4V and Ti-6AL-4V-Ta alloys.

3.2 Powder characterization

The specimens used in this study were lattice-printed and dense-printed Ti-6Al-4V ELI and Ti-6Al-4V-Ta alloys, commonly known as DTi and LTi, respectively. The powder Ti–6Al–4V ELI with a grade size of 20–53μm was acquired from Sino-Euro Materials of Xi' and Co, Ltd. (Sino-Euro), a Northwest Institute for Non-ferrous Metal Research division. Also, as an alloying option for this study, Ti–6Al-4V powder was mixed with Ta powder. It intricates a mixture of 92 wt% Ti-6Al-4V and 8 wt% pure tantalum (Ta). Ta powder has a grain size of 15-53 μm and is bought from Luoyang Tongrun Info Technology Co., Ltd. A mixture machine was used to mix the powders. The Ti–6Al-4V-Ta powder was tumbled and mixed for 7.5 hours at 60 rpm. The EDS analysis was conducted by scanning electron microscopy (SEM) JEOL JSM-IT200(LA) to identify the chemical composition of the virgin powders and dense structure, and a Mastersizer 3000 was used to detect particle size distribution of the used powders as well. The optical parameters were an absorption coefficient of - 1.413 and a refractive index of - 2.51.

3.3 Lattice structures

The design of the lattice specimens was mainly implemented using MSLattice for triply periodic minimal surface (TPMS) structures. A literature review showed that Diamond, Cube, and Primitive lattice structures perform best overall in energy absorption, contain porosity, and stiffness similar to the human bones [2-7]. Therefore, in this proposed research, 20% density along with a unit cell size of 3 mm for the Gyroid structure and 20 and 30% density along with a unit cell size of 5 mm for the Diamond and Primitive structures were utilized (table 3.1). Different unit cell sizes were used for the Gyroid structure (3 mm, not 5 mm) because of the structure's strut thickness around the facial part. It is known that at that edge, the cell size has half of the cells to create a flat surface. Hence, if 5 mm is chosen as a UCS, then the strut size around the surfaces becomes less than 1 mm. This could lead to printing failures since the printer can print the specimens with a strut size of at least 0.5 mm thick. A 3 mm UCS was utilized for the Gyroid structure to eliminate the printing failure. The overall size of the TPMS lattice structures was 15x15 mm, as shown in Table 3.1. Figure 3.1 illustrates lattice structures that are used in this investigation.

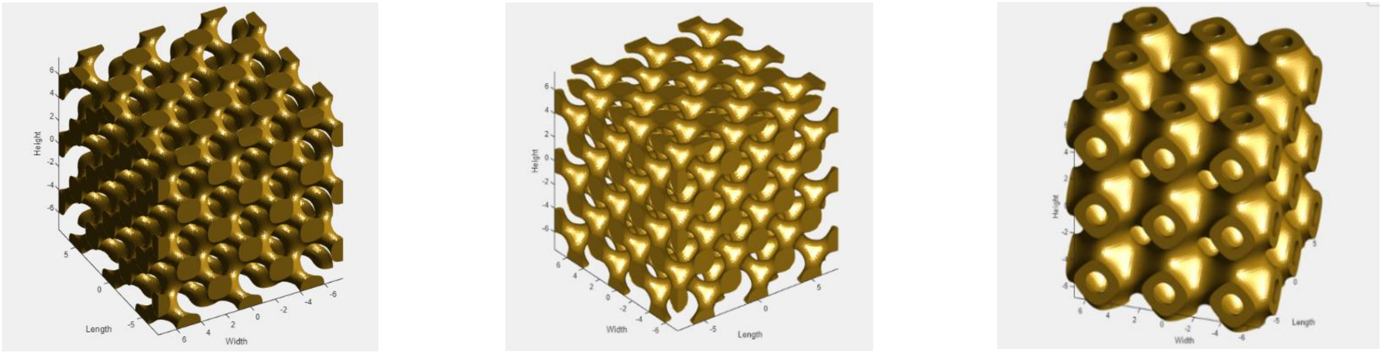

a **b** **c**

Figure 3.1: Types of lattice structures that were investigated: (a) diamond; b) gyroid; (c) primitive

Table 3.1: The density and size of the lattice structures generated in MSLattice made of Ti-6Al-4V

Models	Density, %	UCS, mm	Height, mm	Width, mm
Diamond	20, 30, 35, 40	3, 5	15	15
Gyroid	30, 35, 40	3, 5	15	15
Primitive	20, 30, 35, 40	3, 5	15	15

Table 3.2 represents the density and size of the lattice structures generated in MSLattice made of Ti-6Al-4V-Ta.

Table 3.2: The density and size of the lattice structures generated in MSLattice made of Ti-6Al-4V-Ta

Models	Density, %	UCS, mm	Height, mm	Width, mm
Diamond	30, 35, 40	3	15	15
Gyroid	30, 35, 40	3	15	15
Primitive	30, 35, 40	3	15	15

3.4 SLM process parameters and manufacturing

The Renishaw AM 400 was utilized to produce the specimens using the SLM principle. The manufactured samples were chosen to be either porous or dense. Dense samples were later tested for bulk material characterization. The process parameters were selected as the default of Renishaw suggestions, chosen from the software library for Ti-6Al-4V. Hence, both dense and lattice samples were manufactured with the laser power of 200 W, hatch spacing of 0.08 mm, scanning speed rate of 1112 mm/s, and layer thickness of 0.03 mm, as demonstrated in Table 3.2. All printing was done using the reduced build volume (RBV) platform. Table 3.3 represents the SLM-printing process parameters used for both alloying options.

made of Ti-6Al-4V-Ta.

Table 3.3: Process Parameters used for SLM printing of Ti-6Al-4V

laser power, W	scanning speed, mm/s	hatch spacing, mm	layer thickness, mm
200	1112	0.08	0.03

3.5 Lattice structure characterization

The compressive behavior of lattice structures has been extensively studied and is well-documented. It is notably more straightforward than a tensile test, necessitating a specialized testing setup to prevent potential stress concentration.

Regarding deformation modes under compression, lattice structures are categorized into stretch-dominated and bending-dominated types. The main difference between them is that for stretch-dominated lattice structures, struts deform axially, while for bending-dominated lattice structures, they deform primarily due to bending. Both types of lattice structures exhibit elastic, plastic, and densification regions. Stretch-dominated lattices display fluctuating plastic zones, while bending-dominated lattice structures exhibit weaker but stable plastic zones.

The values of stress (represented by σ) and strain (represented by ε) are determined based on factors such as the force applied by the compression platen on the lattice (F), the initial area of the lattice base (A_0), the amount of deformation (Δ), and the original height of the structure (h_0). These calculations can be expressed as follows:

$$\sigma = \frac{F}{A_0} \tag{3.1}$$

$$\varepsilon = \frac{\Delta}{h_0} \tag{3.2}$$

The energy absorption at a specific strain level could be obtained by integrating the stress-strain curve, starting from zero and extending to the point of densification strain. Thus

$$\psi = \int_0^{\varepsilon_d} \sigma(\varepsilon) d\varepsilon \tag{3.3}$$

The efficiency of energy absorption is provided by

$$\eta = \frac{\int_0^{\varepsilon_d} \sigma(\varepsilon)\mathrm{d}\varepsilon}{\sigma_m \times \varepsilon_d} \tag{3.4}$$

Where σ_m is the maximum stress on the stress-strain curve, the efficiency of the bending-dominated lattice structures is higher than that of the stretch-based lattice structures due to the smooth stress-strain profile of the bending-dominated lattices [17].

Plateau stress is calculated by:

$$\sigma_p = \frac{\int_0^{\varepsilon_d} \sigma(\varepsilon)\mathrm{d}\varepsilon}{\varepsilon_d - \varepsilon_y} \tag{3.5}$$

Where ε_y is the strain when the first peak occurs.

3.6 Mechanical analysis

For the tensile and compression tests at ambient temperature, a universal testing machine with a 50 kN load cell was used (Figure 3.2). The dense specimens were designed using the Solidworks software.

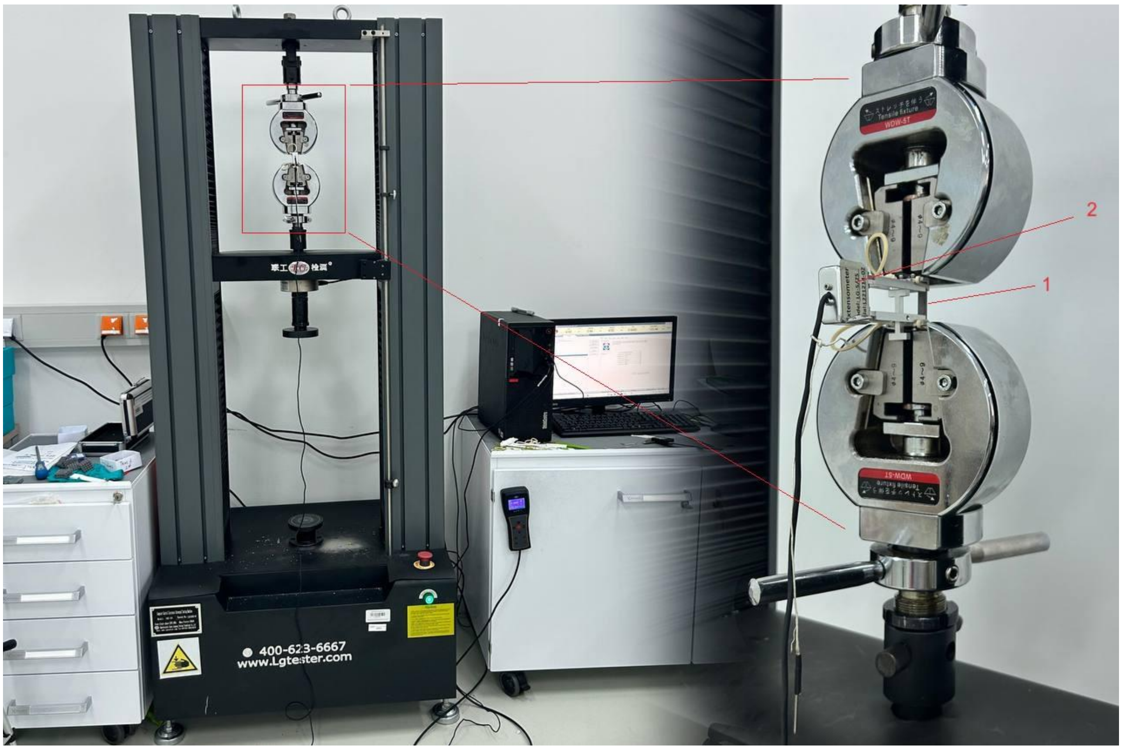

Figure 3.2: Tensile test setup: 1 - sample, 2 - extensometer

Tensile tests were performed according to ASTM E8M-13a (American Society for Testing and Materials, 2013). The tensile bulks have a gauge length (G) of 30 mm, a diameter (D) of 6 mm, a radius (R) of 6 mm, and a length of reduced section (A) of 36 mm (Figure 3.3). The tensile tests were conducted at a strain rate of 3 mm/min until fracture. After the test, using a SEM, the fractography of the broken specimens was examined. The broken tensile bulks were cut by water abrasive jet machining and inserted into the SEM for fractographical investigations. All these procedures were applied in order to investigate the material surface.

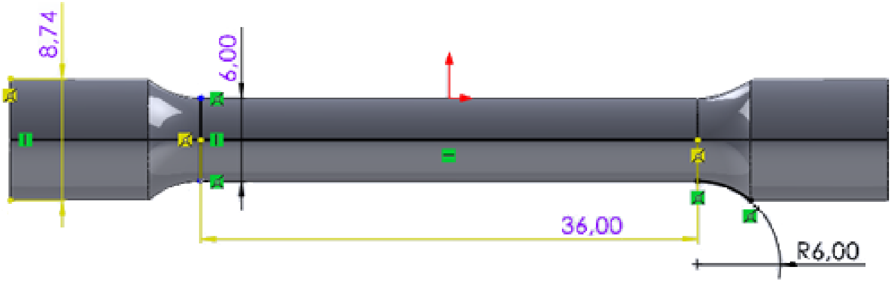

Figure 3.3: Tensile test specimen

Compression tests were performed on the TPMS lattice structures highlighted in tables 3.1 and 3.2 as depicted in Figure 3.4. The compression tests were conducted at a strain rate of 1 mm/min until the UTS value reached from the up to the downside direction.

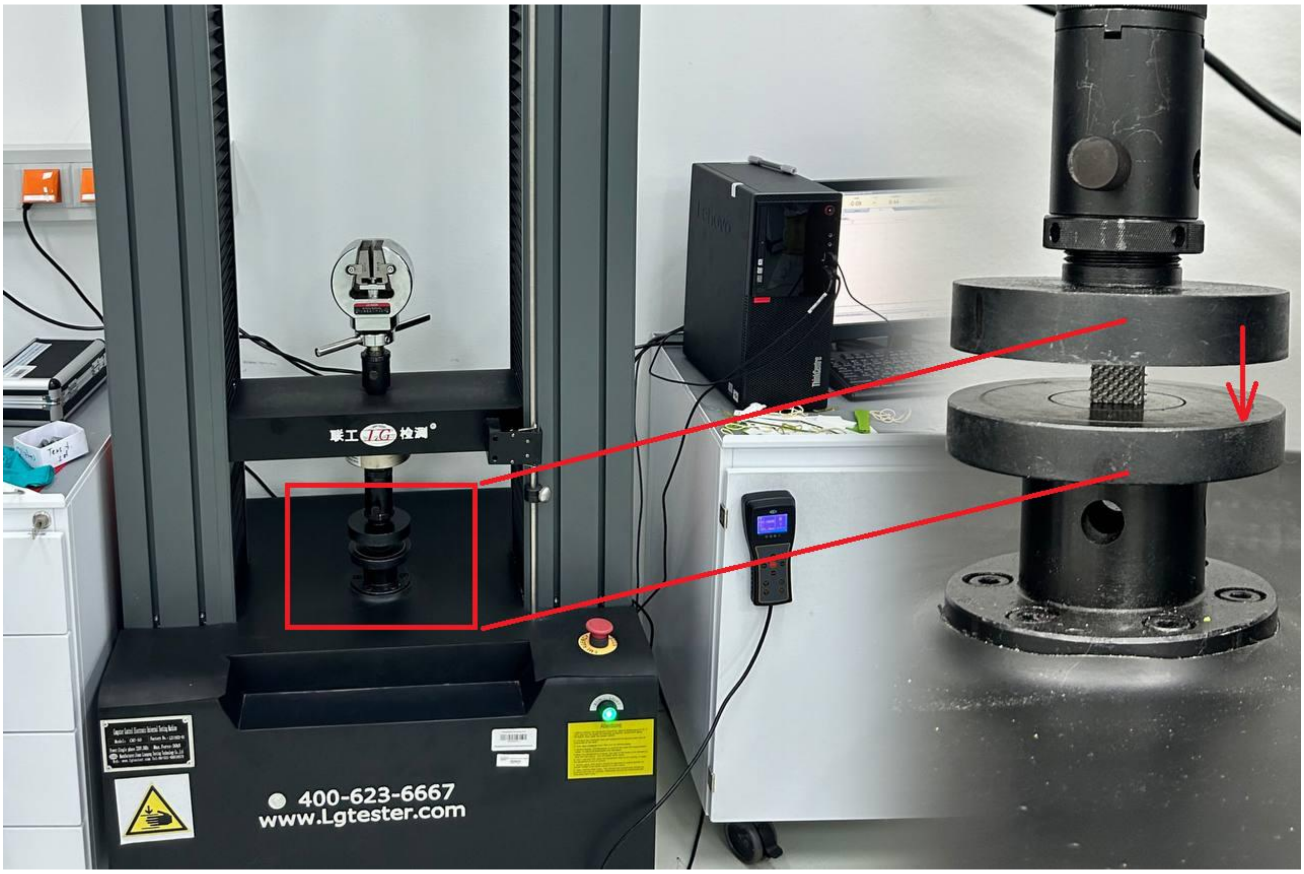

Figure 3.4: Compression test setup

Vickers microhardness on cross-sectioned specimens with 0-degree and 90-degree inclinations in the print was measured using the 1G-62.5KGF Micro/Macro Vickers Knoop & Brinell hardness tester machine. Figure 3.5 represents the setup for the hardness test. For each angle print, three tests were performed. The hardness load was 200 g with a Dwell time of 12 seconds. Table 3.3 shows the procedure for preparing the material for the hardness testing. The specimen was ground and polished in advance before testing.

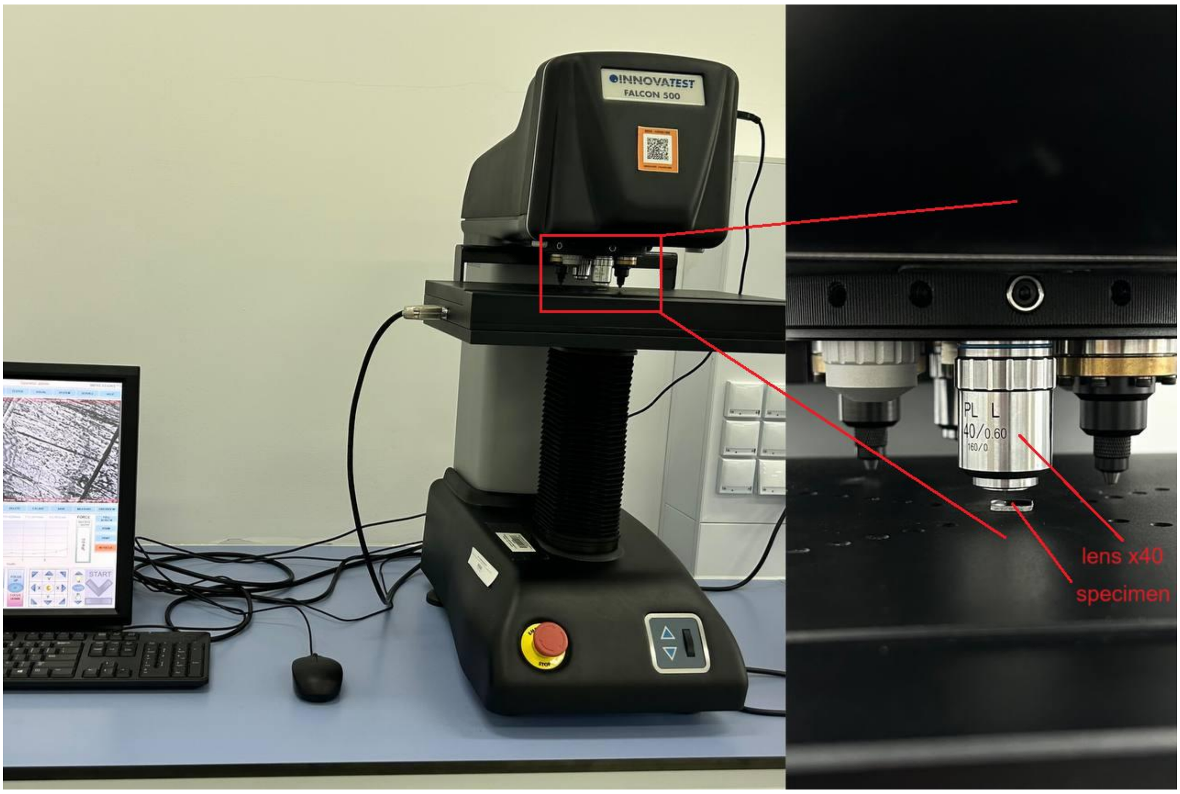

Figure 3.5: Hardness test setup

Table 3.4: Preparation procedure of the specimens for hardness test

Step	Paper	Liquid	Speed rate, rpm	Load, N	Time, min
Planar grinding	foil P320	H_20	250-300	25	until plane
Grinding	foil P600	H_20	250-300	25	1:30
Pre-polishing	APLHA	Dia Complete Ploy, 9 µm	120-150	30	5:00
Final polishing	OMEGA	Eposil F, 0.1 µm*	120-150	40	10:00

3.7 Corrosion test

The CS Series Electrochemical workstation Corrtest Potentiostat/galvanostat was used to measure the samples' corrosion. Ag/AgCl (1M KCl) and a platinum rod (Pt) served as the reference and counter electrodes, respectively. The polished specimens with an electrode area of 0.071 cm^2 were employed as working electrodes. Figure 3.6 illustrates how the corrosion test is set up. Open circuit potential (OCP) was monitored for one hour before corrosion measurements in order to stabilize the potential of the samples (working electrodes) in the NaCl solution (50 ml of distilled water and 3.5% NaCl).

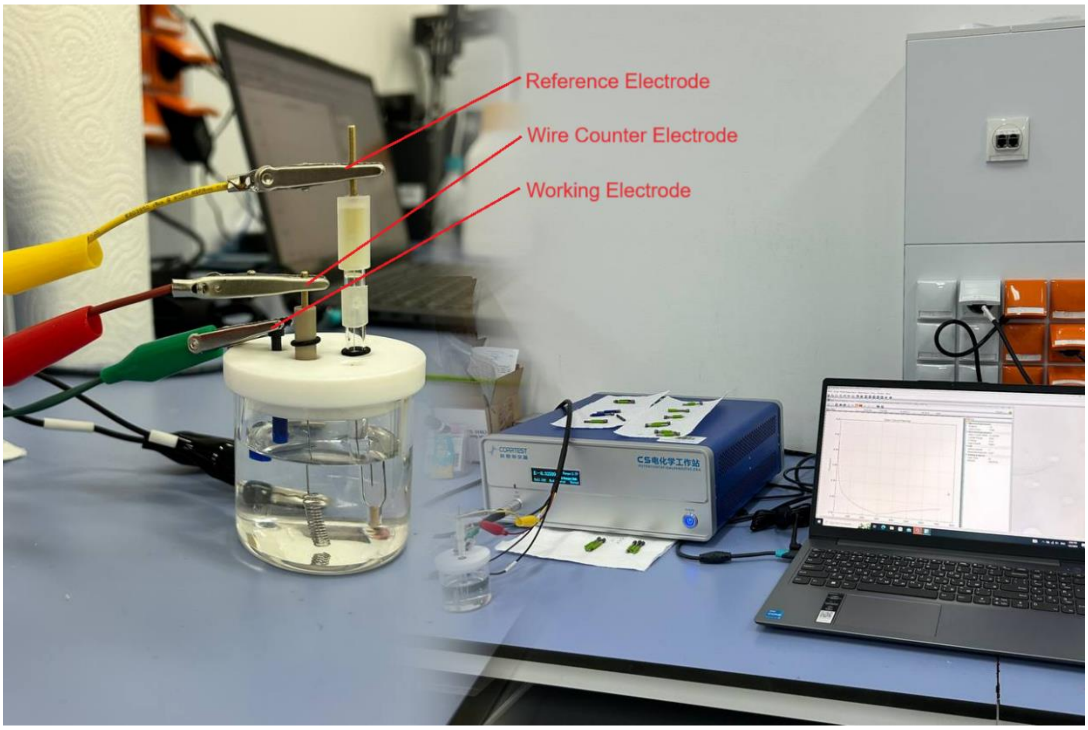

Figure 3.6: Corrosion test setup

Electrochemical Impedance Spectroscopy (EIS) versus frequency experiments were conducted by administering an alternating current (AC) potential of approximately 10 mV across a frequency spectrum ranging from 0.1 MHz to 100 kHz. All electrical potentials and currents in this study were benchmarked against the Ag/AgCl (1M KCl) reference electrode. In the potentiodynamic assessments, the potential at the working electrode was incrementally adjusted from -0.1 V to +1 V relative to the Open Circuit Potential (OCP) at a scanning velocity of 5 mV/s. This meticulous approach facilitated a comprehensive analysis of the electrochemical properties under varying conditions. The corrosion tests were repeated three times to improve the results, and the average was taken.

The Archimedes method was also used to identify the density of the specimens. The mass of each sample was proportioned to the volume of each sample in distilled water.

Current density is computed based on the Stern-Geary equation:

$$i_{corr} = \frac{\beta_a \times \beta_c}{\beta_a + \beta_c} \times \frac{1}{R_p} \tag{3.6}$$

where i_{corr}(A/cm^2) - current density,

β - Stern Geary coefficient,

R_p (Ohms/cm^2) - slope of the curve/polarization resistance.

The equation to find Stern Geary coefficient is:

$$\beta = \frac{\beta_a \times \beta_c}{\beta_a + \beta_c} = \frac{b_a \times b_c}{2.303 \times (b_a + b_C)} \qquad (3.7)$$

R_p was identified from the following diagram:

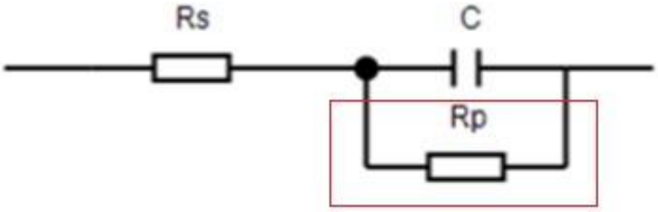

Figure 3.7: Corrosion test R_S(C-R_P) diagram: R_S - solution resistance, C - charge capacitance

3.8 Bacteria adhesion

The objective of this study was to determine the antibacterial effectiveness of Ti-6Al-4V and Ti-6Al-4V + 8% Ta against a range of bacterial strains, including Pseudomonas aeruginosa, Bacillus subtilis, Staphylococcus aureus ATCC 6538-P, and Escherichia coli (DH5α), by measuring the amount of biofilm that formed on the surface of various metal cubes 48 hours after the inoculation in broth culture. An initial optical density (OD 600) of 0.5 was obtained for each bacterial species in a fresh 24-hour liquid culture, which was then used to prepare the bacterial inoculum. Using a microplate reader, the OD 600 of the 24-hour culture broth was measured to ascertain the precise quantity of bacteria needed to be added to a fresh medium in a 50 mL Falcon tube to generate a final volume of 50 mL with an OD of 0.5.

A three-step procedure was used to sterilize every metal cube to guarantee that all possible pollutants were eliminated. The cubes were first exposed to 70% ethanol for 30 minutes. They are then cleaned with plasma for five minutes (using a plasma cleaner PDC-002-CE). Before growing the metal cubes with bacteria, they were thoroughly sanitized for 30 minutes under a UV lamp. Except for S. aureus, which was cultured in tryptone soy broth (TSB), a 50 mL Falcon tube was filled with Luria-Bertani (LB) broth to create the inoculum. The single species of bacteria in the culture medium was then contained in a separate 50 mL Falcon tube where each metal cube was suspended. In an aerobic environment, these tubes were kept in a shaker incubator at 37°C and a speed of 220 RPM for 48 hours.

After 48 hours of incubation, the broth was carefully decanted to dispose of any non-adherent (planktonic) bacteria. After removing any weakly attached cells, the metal cubes containing the biofilms were carefully washed in sterile distilled water to maintain the quality of the biofilm structure. To ensure consistency in the following staining processes, each metal cube was placed into a separate well of a 24-well plate and left to air-dry for 30 minutes.

The metal cube surface was covered with 1.3 mL of 0.1% crystal violet solution in each well for 60 minutes in order to see and measure the production of biofilms. To eliminate unbound color, excess crystal violet was carefully aspirated, and the metal cubes were triple washed with distilled water. A Zeiss AxioZoom V16 microscope was used to observe and take images of the samples. Red fluorescence and bright-field images were obtained with exposure periods of 400 ms and 20 ms, respectively. All images were stored in the CZI (Carl Zeiss Image) format for further examination using ImageJ software.

A 30% acetic acid solution was used to evaluate biofilm formation quantitatively. Each well in the 24-well plate holding a metal cube received 1.3 milliliters of the acetic acid solution to dissolve the crystal violet. The 24-well plate was put on a shaker and shaken for 30 minutes at 180 rpm to speed up the dissolution process. In order to prevent disturbing the solubilized dye solution, the metal cubes were cautiously taken out of the wells following this agitation procedure. 100 µL of the acetic acid solution, which now contained the dissolved crystal violet, was transferred from each well into the matching well of a 96-well plate to measure the biofilm biomass. The solutions' absorbance (OD 590) values in the 96-well plate were determined using a VICTOR Nivo multimode plate reader.

Chapter 4 – Results and Discussion

4.1 Overview

This section of the paper discusses the outcomes and observations from the experiments that were conducted. First, an analysis of the properties of unused Ti-6Al-4V ELI and Ti-6Al-4V-Ta powder is presented. Then, the analysis centers around the impact of dense and porous materials on mechanical properties and characteristics. Additionally, fractography is examined after a tension test on the cracked surface and a corrosion test and biomedical response.

4.2 Characterization of virgin powders

4.2.1 Ti–6Al–4V ELI

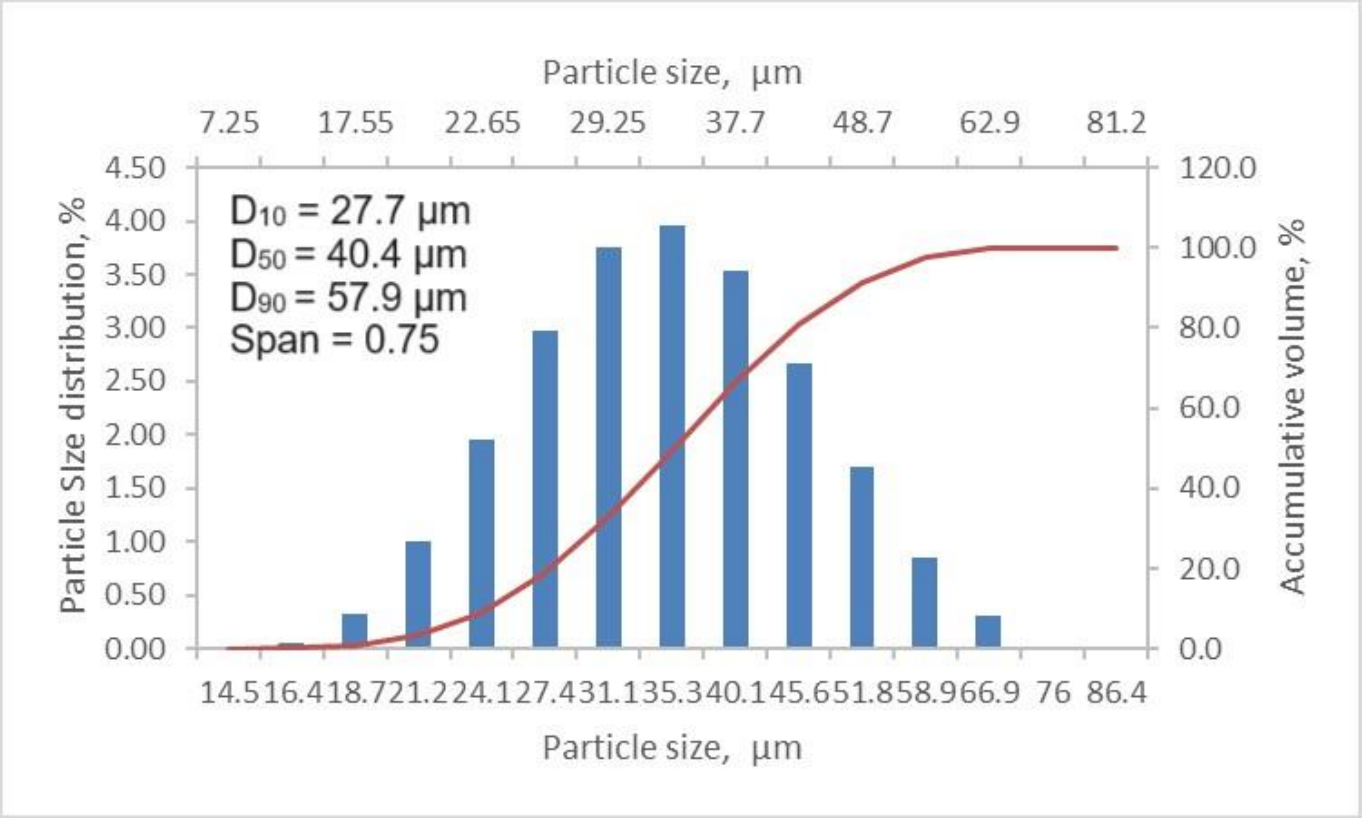

Figure 4.1 Particle size distribution of the virgin Ti-6Al-4V powder

The particle size distribution (PSD) of the virgin Ti–6Al–4V ELI powder ranged between 20 to 53 µm, with D_{10}, D_{50}, and D_{90} values of 27.7 µm, 40.4 µm, and 57.9 µm, respectively (Figure 4.1). The PSD showed a 0.75 span. Hence, the PSD results illustrate that the powder is coarse and has a wide particle size distribution, as shown in Figure 4.1.

The powder particle morphology exhibits good sphericity, but a small satellite presence is observed (Figure 4.2). The figures on the SEM were obtained using the magnification sizes of 20 μm and 100 μm, respectively (Figure 4.2).

Table 4.1 lists the outcomes of the EDS study performed on the virgin Ti-6Al-4V ELI powder and dense specimen using an SEM. The aluminum and vanadium concentrations of the Ti–6Al–4V ELI powder (5.87±0.02 and 4.17±0.02%) were within the specified range, as indicated by ASTM F136-13 (5.5–6.5% for Al and 3.5–4.5% for V). As a result, the same powder was utilized to produce DTi and LTi.

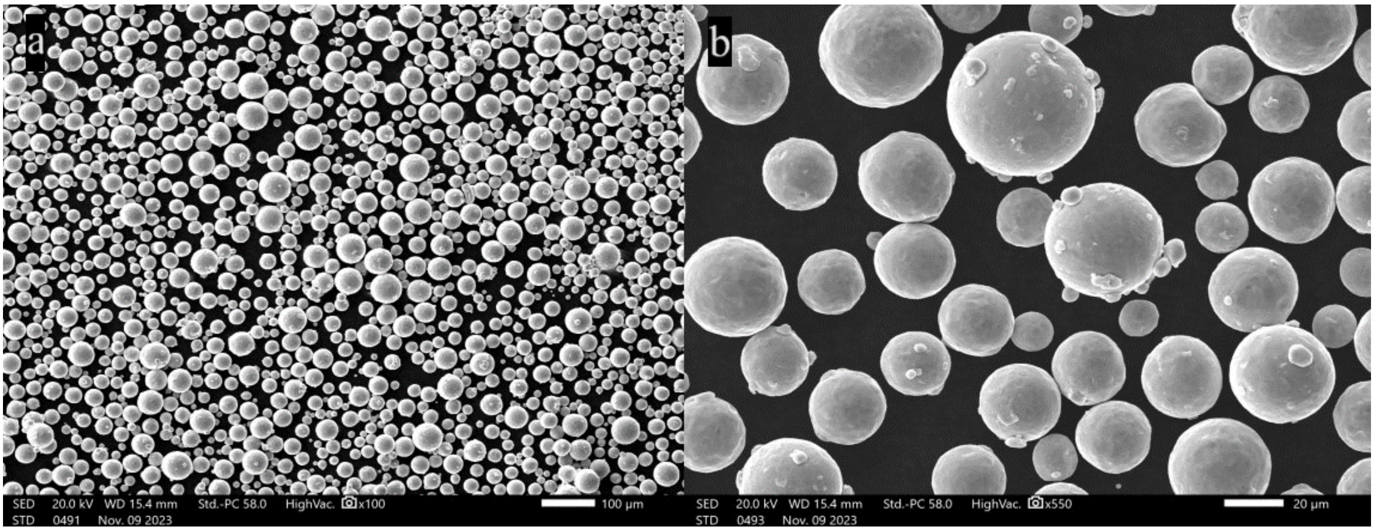

Figure 4.2: Powder morphology image of the virgin Ti-6Al-4V powder: (a) magnification size of 100 μm; (b) magnification size of 20 μm

Table 4.1: Chemical composition of the virgin Ti–6Al–4V ELI powder and dense specimen

%	Ti	Al	V	C
Ti-6Al-4V powder	89.97±0.07	5.87±0.02	4.17±0.02	<0.5
DTi-6Al-4V	89.55±0.06	6.47±0.02	3.97±0.02	<0.5

4.2.2 Ti–6Al–4V-Ta

The virgin Ti–6Al–4V–Ta powder had a PSD of 15–53 μm, with D_{10}, D_{50}, and D_{90} values of 28.3 μm, 40.3 μm, and 56.5 μm, in that order (Figure 4.3). A 0.69 span from the PSD was noted. Ti–6Al–4V–Ta powder is also coarse as Ti–6Al–4V and has a wide particle size distribution, as shown in Figure 4.3.

Although there is a slight satellite presence, the powder particle shape shows satisfactory sphericity (Figure 4.4). Magnification sizes of 100 μm and 20 μm, respectively, were used to acquire the SEM images (Figure 4.4). The only difference between Ti-6Al-4V (Figure 4.2) and Ti-6Al-4V-Ta (Figure 4.4), Ti-6Al-4V-Ta has lighter powder spheres which intricate to Ta.

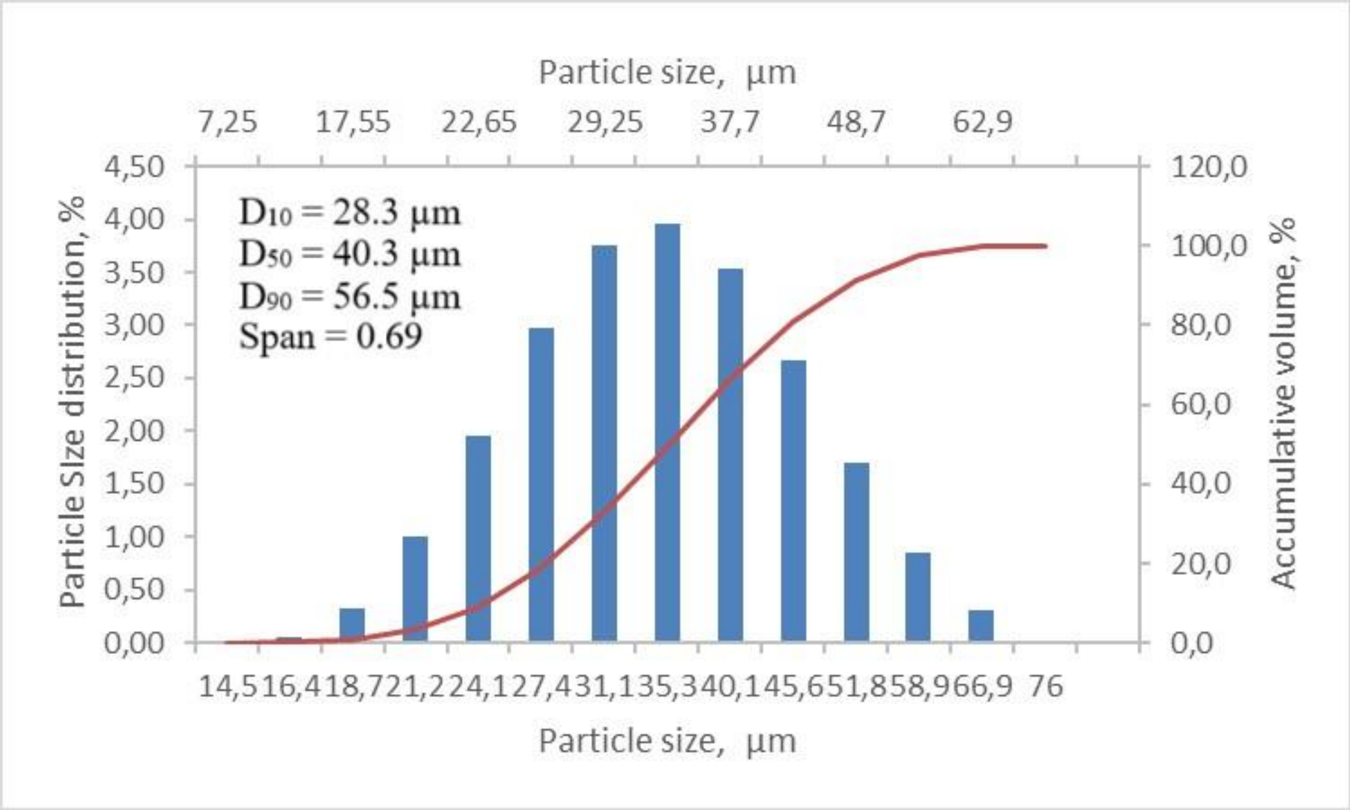

Figure 4.3 Particle size distribution of the virgin Ti-6Al-4V-Ta powder

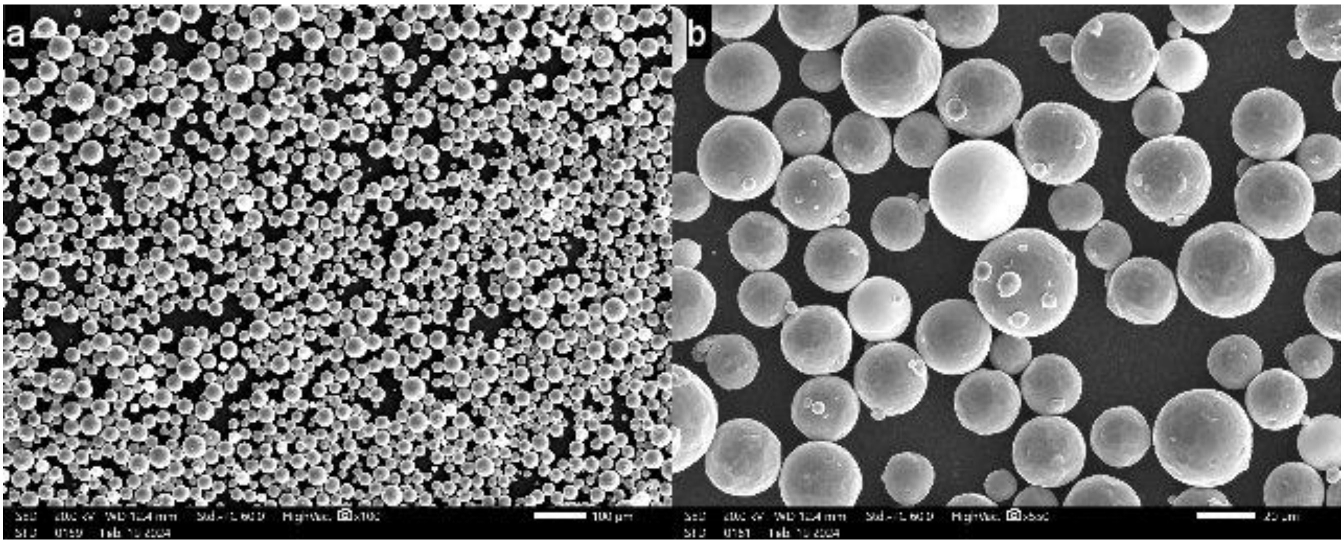

Figure 4.4: Powder morphology image of the virgin Ti-6Al-4V-Ta powder: (a) magnification size of 100 µm; (b) magnification size of 20 µm

Table 4.2 lists the outcomes of the EDS study performed on the virgin Ti-6Al-4V powder and dense specimen using an SEM. The aluminum and vanadium concentrations of the Ti–6Al–4V ELI powder were within the range of 4.89±0.05 and 3.91±0.06% wt, while Ti and Ta were 82.38±0.21 and 8.82±0.13. The same powder was utilized for the production of DTi and LTi.

Table 4.2: Chemical composition of the virgin Ti–6Al–4V-Ta powder and dense specimen

%	Ti	Al	V	Ta	C
Ti-6Al-4V-Ta	82.38±0.21	4.89±0.05	3.91±0.06	8.82±0.13	<0.5
DTi-6Al-4V-Ta	84.37±0.21	5.85±0.05	3.59±0.06	6.18±0.12	<0.5

4.3 Bulk Mechanical Properties and Crack investigations, Hardness test

4.3.1 Ti–6Al–4V ELI

Figure 4.5 illustrates the tensile tests of as-built Ti-6Al-4V samples. Experimental tensile testing results showed an ultimate tensile strength of 1241.58±5.97 MPa, while Yield Strength is 1151±5.66 MPa and Elastic Modulus is 116.63±4.35 GPa, as shown in Table 4.3. Moreover, Figure 4.6 illustrates the Stress-Strain values of tensile test results of the Ti-6Al-4V samples.

Figure 4.5: Tensile results of the Ti-6Al-4V samples

Table 4.3: Tensile test results of the Ti–6Al–4V dense parts

Experiment number	Yield Strength, MPa	Ultimate Tensile Strength, MPa	Elastic Modulus, GPa
1	1158.8±5.75	1225.75±5.99	118.15±3.25
2	1138.19±5.68	1250.85±6.05	116.09±1.15
3	1156.03±5.56	1248.13±5.87	115.65±8.66
average	1151±5.66	1241.58±5.97	116.63±4.35

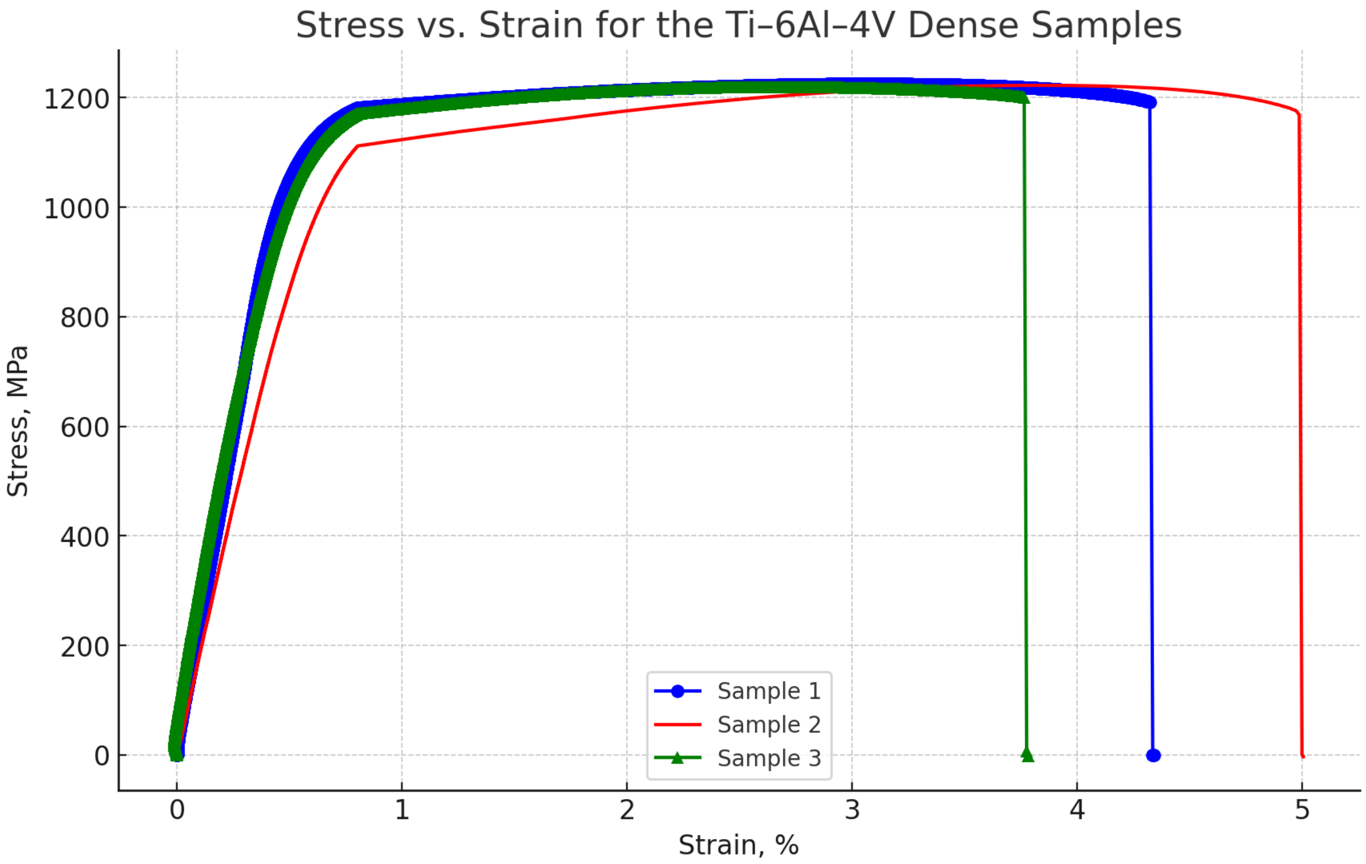

Figure 4.6: Tensile test results of the Ti–6Al–4V dense parts

After conducting the tensile test, the broken specimens after tension labeled five underwent analysis using a scanning electron microscope (SEM) to examine their fractography, as shown in Figure 4.7. The SEM images for Figure 4.7 revealed various features on the fractured surfaces, providing insights into the materials' behavior under stress of tension. Several defects were observed on the overall surface, including pores, dimples, tear ridges, and cleavage. These features collectively suggest a combination of ductile and brittle characteristics in the specimens [20]. Notably, the fractography of specimen DTi indicated a brittle nature, aligning with expected ductile traits within the cracks. In the paper of Suresh et al. [20], the specimens had the same features but with a negligible amount of unmelted powder. The trapped and unmelted particles on the side surface result from a lack of vacuuming of the powder after printing or improper cleaning. Furthermore, the appearance of unmelted powder in the fractured areas suggested potential problems with material uniformity [20]. The comprehensive fractography analysis provides valuable insights into the material's behavior and quality, highlighting areas for further investigation and improvement in the manufacturing process.

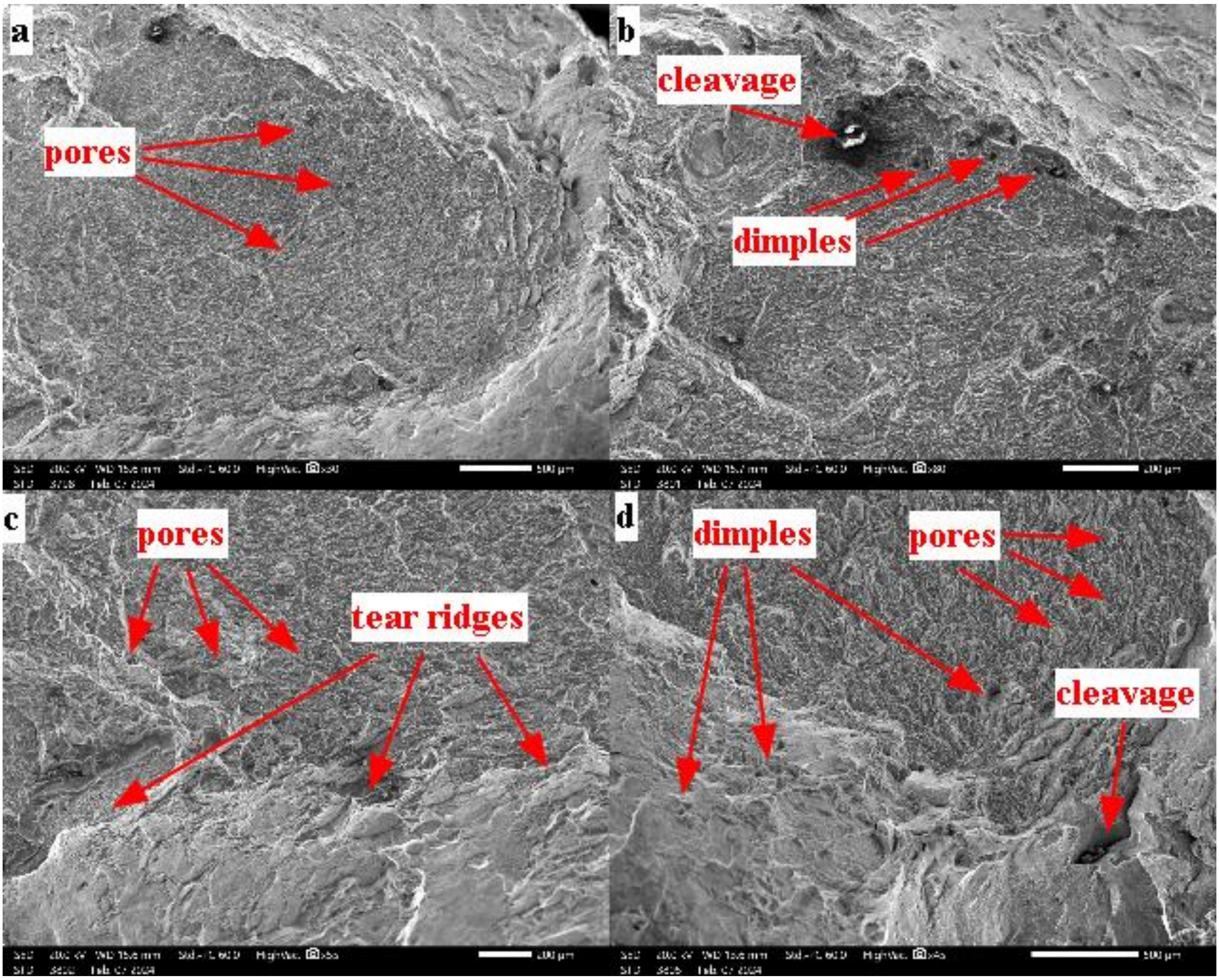

Figure 4.7: Fractography SEM images of the Ti-6Al-4V tensile fractured specimens with the magnifications of (a) x30; (b) x80; (c) x55;(d) x45

The Vickers microhardness was conducted on the 1G-62.5KGF Micro/Macro Vickers Knoop & Brinell hardness tester machine on the cross-sectioned specimens with 0-degree and 90-degree inclinations in the print. For each angle print, three tests were done, as presented in Table 4.4. The average value of the hardness for Ti-6Al-4V is 437.75±9.91 HV and 397.01±1.43 HV for 0 and 90 degrees, respectively.

Table 4.4: Hardness test results of the dense Ti-6Al-4V parts

Printing angle	Experiment 1, HV	Experiment 2, HV	Experiment 3, HV	Average, HV
0	455.09	420.77	437.39	437.75±9.91
90	397.64	394.28	399.12	397.01±1.43

4.3.2 Ti–6Al–4V-Ta

Figure 4.8 shows the tensile tests of the as-built Ti-6Al-4V-Ta samples. Additionally, Figure 4.9 shows the Stress-Strain values of the Ti-6Al-4V-Ta samples' tensile test results. According to Figure 4.9 and Table 4.5, the Ultimate Tensile Strength of the experimental tensile test was 1212.96±5.23 MPa, Yield Strength was 974.55±4.96 MPa, and Elastic Modulus was 180.24±1.27 GPa.

Figure 4.8: Tensile results of the Ti-6Al-4V-Ta samples

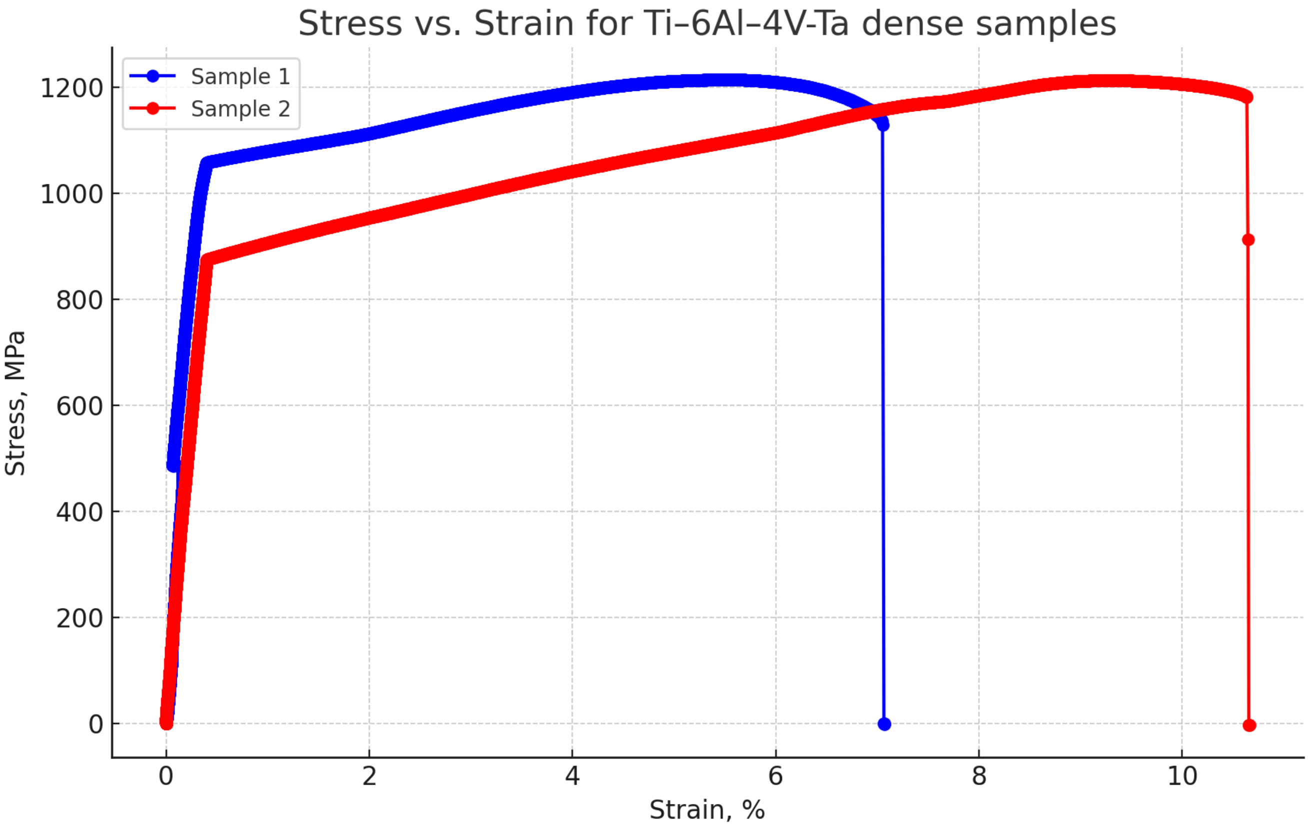

Figure 4.9: Tensile test results of the Ti–6Al–4V-Ta dense parts

Table 4.5: Tensile test results of the dense Ti-6Al-4V-Ta parts

Experiment number	Yield Strength, MPa	Ultimate Tensile Strength, MPa	Elastic Modulus, GPa
1	1064.01±4.59	1213.56±5.32	183.45±1.29
2	885.09±4.34	1212.36±5.13	177.02±1.25
average	974.55±4.96	1212.96±5.23	180.24±1.27

Comparing the tensile test results between Ti-6Al-4V and Ti–6Al–4V-Ta dense parts (Figure 4.10), it is visible that Ultimate and Yield stress values decrease by adding Ta to Ti–6Al–4V, while Elastic Modulus increases. This could be explained by the statement that pure Tantalum is more ductile than Ti-6Al-4V [8}. Hence, this could be stated as the Tantalum effect on Ti–6Al–4V.

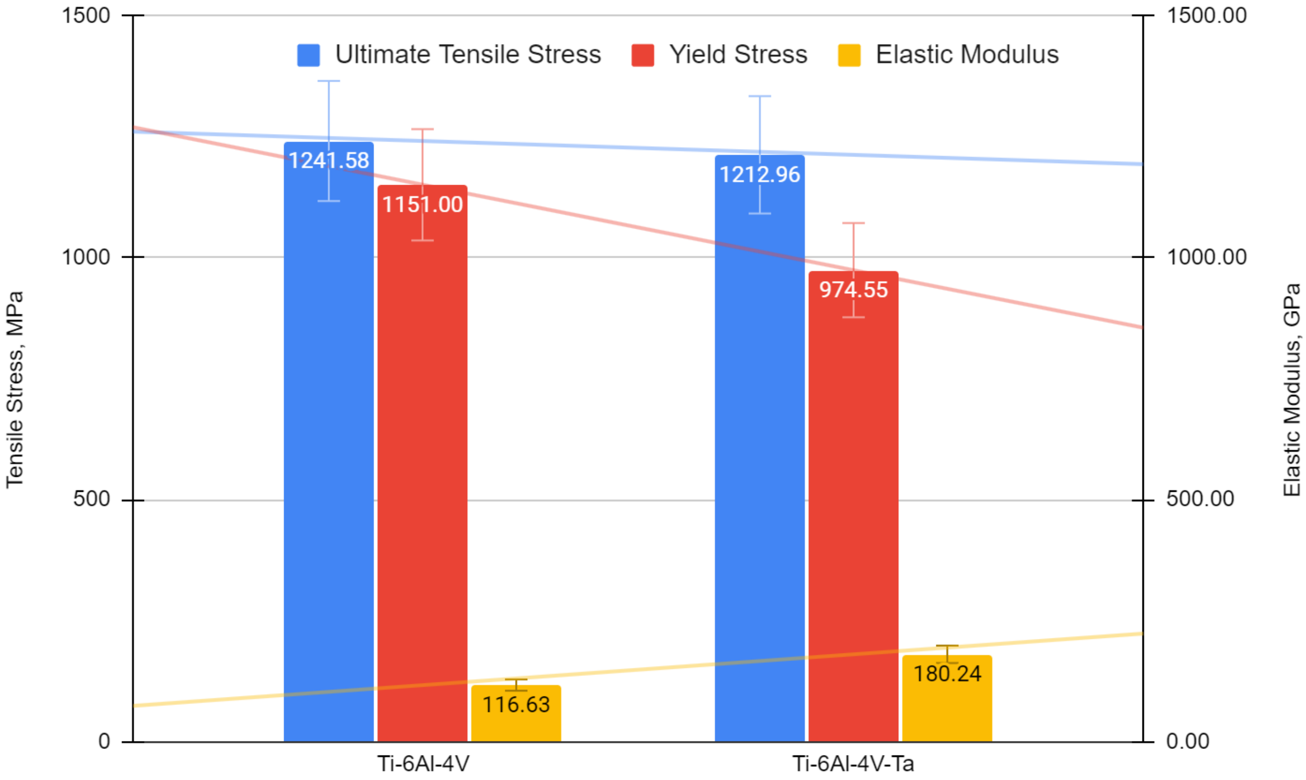

Figure 4.10: Tensile test results of the Ti-6Al-4V and Ti–6Al–4V-Ta dense parts

Tensile testing was followed by a scanning electron microscope (SEM) examination of the fractography of the broken specimens following tension labeling one, as illustrated in Figure 4.11. Pores, dimples, tear ridges, and cleavage were also for Ti-6Al-4V-Ta, as were Ti-6Al-4V, among the defects seen across the entire surface. However, comparing Figures 4.7 and 4.11, the surface of bulks made by Ti-6Al-

4V-Ta has more pores. These parameters, taken together, point to a combination of less brittleness and more ductile properties in the specimens of Ti-6Al-4V with Ta than without it [8, 20].

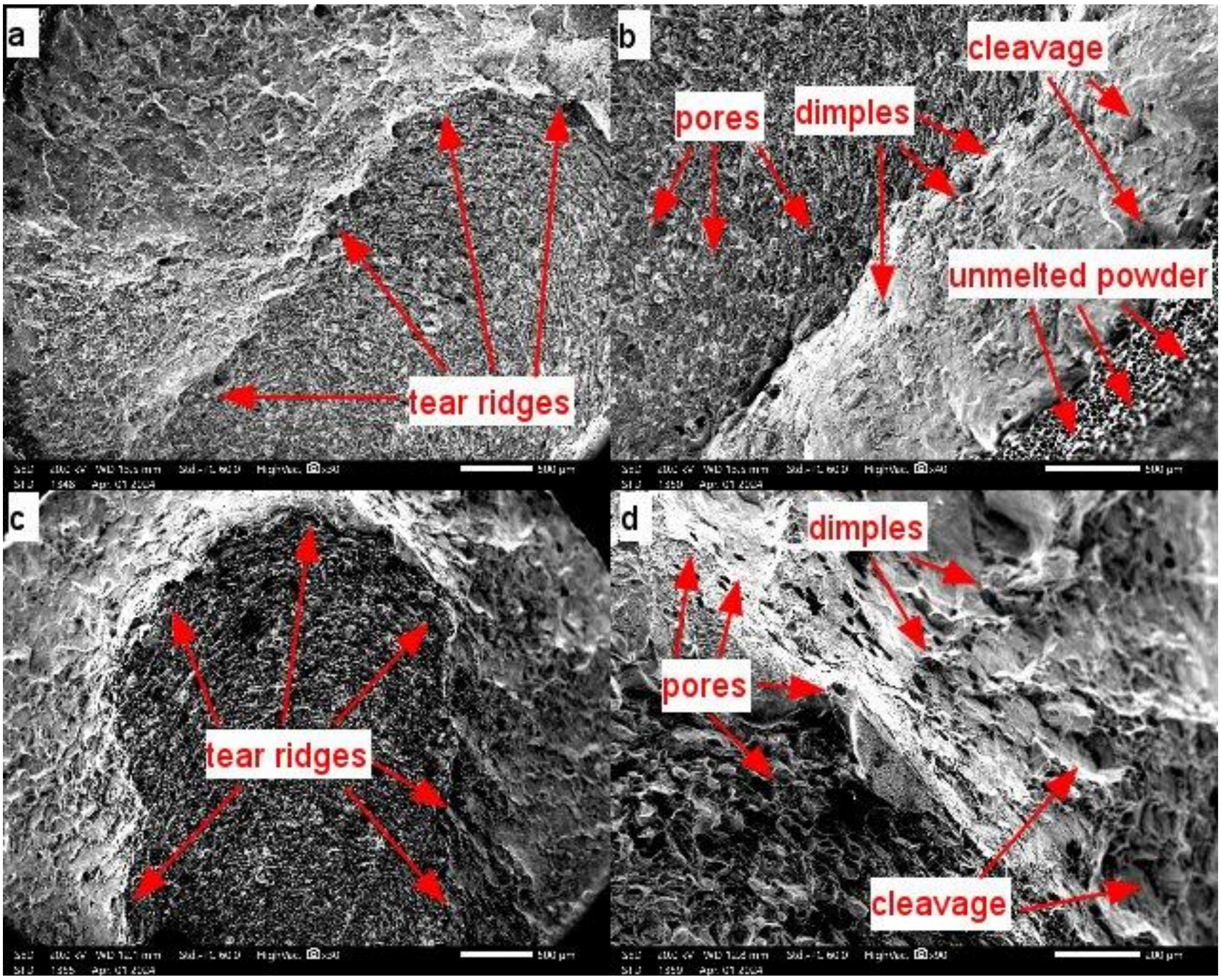

Figure 4.11: Fractography SEM images of the Ti-6Al-4V-Ta tensile fractured specimens with the magnifications of (a) x30; (b) x40; (c) x30 ;(d) x90

The Vickers microhardness test was also conducted on three specimens made of Ti-6Al-4V-Ta, as for Ti-6Al-4V, on cross-sectioned specimens with 0-degree and 90-degree inclinations in the print (table 4.4). Ti-6Al-4V-Ta has an average hardness of 428.79±5.15 HV at 0 degrees and 391.46±2.38 HV at 90 degrees, respectively. Overall, the obtained hardness test results for Ti-6Al-4V-Ta indicate slightly less hardness than Ti-6Al-4V.

Table 4.6: Hardness test results of the dense Ti-6Al-4V-Ta parts

Printing angle	Experiment 1, HV	Experiment 2, HV	Experiment 3, HV	Average, HV
0	419.58	429.40	437.39	428.79±5.15
90	393.55	394.12	386.7	391.46±2.38

4.4 Lattice Mechanical Properties

4.4.1 Ti–6Al–4V ELI

In Figure 4.12, SLM-printed lattice structures for compression tests are demonstrated. After printing, Diamond lattice structures had redundant materials at the corners, as shown in Figure 4.12. If these lattice structures are used for biomedical applications, they should be machined with an electro-discharged machine EDM or other equipment to resolve this side redundancy. However, the next printing was fine.

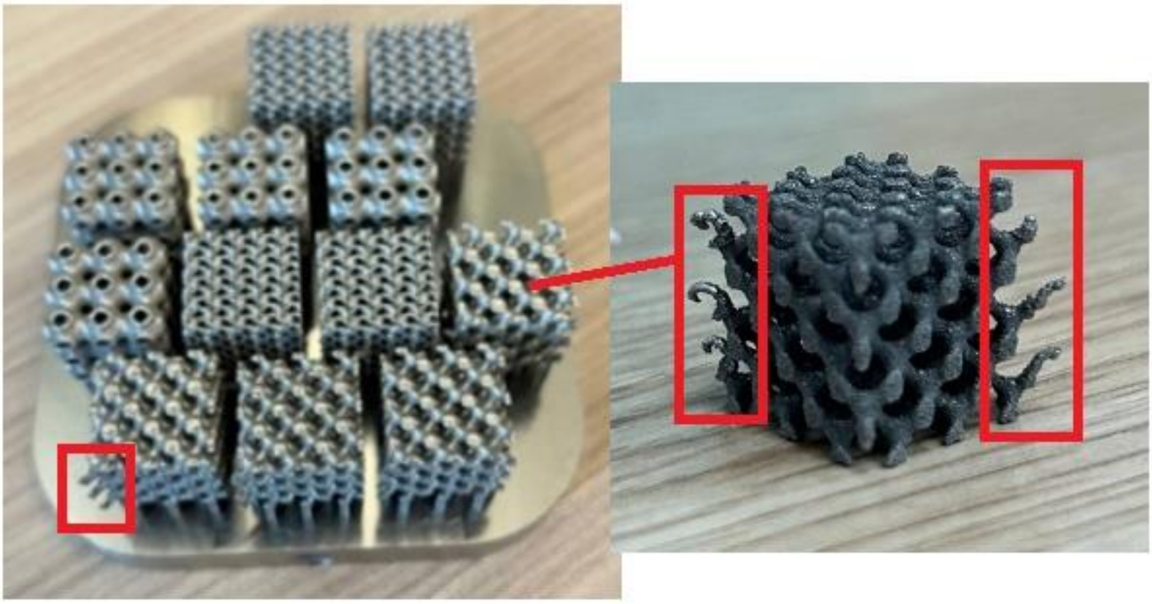

Figure 4.12: SLM-printed lattice samples for compression

The compression results of the lattice structures state that the mechanical properties of the lattices were below expectation, which is why there is a need for optimal density for the next printing. The human femur bone has a load-bearing capacity of 205 MPa when compressed along its length, as per its mechanical properties for Ultimate Compression Stress [18]. Future research aims to examine similar lattice structures within a 30- 40% density range. This is because, from the obtained results, it is discernable that Ultimate Compression Stress is doubled with differences in 20% and 30% of densities (table 4.7). From the given table, it is shown that the highest value of Ultimate Compression Stress belongs to the Gyroid structure (143.96±0.89 MPa), while the lowest value of the Ultimate Compression Stress has the Diamond structure with 20% density (46.89±0.43 MPa). The exact sequence is obtained in Yield Strength. However, it has the lowest value of Elastic Modulus (3.18±1.54 GPa). Moreover, if the Ultimate Compression Stress and Yield Strength values are compared regarding strength differences, Diamond structures with 20% density have close numbers. This is 46.32±0.38 MPa and 46.89±0.43 MPa of Yield and Ultimate Compression Stress, respectively. The other lattice types have around 5 MPa (Primitive, 20% density), 7 MPa (Diamond, 30%

density), 11 MPa (Primitive, 30% density), and 19 MPa (Gyroid, 30% density) of differences in strength value among Yield Strength and Ultimate Compression Stress. In addition, the highest number of Elastic Modulus is acquired for Diamond structures (≈13 GPa), continuing in the sequence of Primitive structures (≈4 GPa) and Gyroid structures.

Table 4.7: Compression results of the Ti-6Al-4V lattice structures

Tested lattice structures	Yield Strength, MPa	Ultimate Compression Stress, MPa	Elastic Modulus, GPa
Gyroid (30% density, UCS=3)	124.02±0.81	143.96±0.89	3.18±1.54
Diamond (20% density, UCS=5)	46.32±0.38	46.89±0.43	13.76±9.24
Diamond (30% density, UCS=5)	98.78±0.75	105.97±0.78	13.82±9.07
Primitive (20% density, UCS=5)	62.18±0.48	67.53±0.5	3.68±1.90
Primitive (30% density, UCS=5)	125.68±0.878	136.57±0.91	5.51±3.19

Figure 4.13 illustrates the bar chart with the stress-strain curves obtained after compressing the lattice structures. As can be seen in the chart, the lower strain value belongs to the Diamond lattice structures with 20% density for both strain-stress values, while the highest belongs to the Gyroid structure.

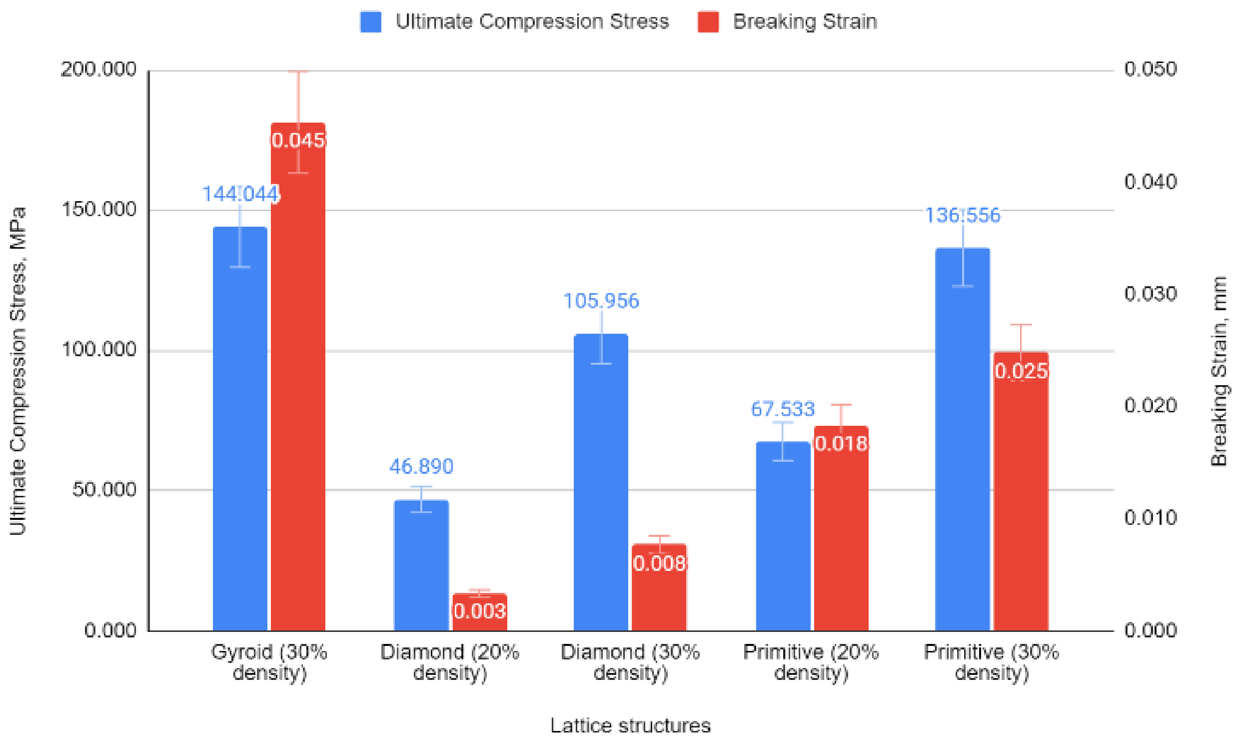

Figure 4.13: Compression results of the Ti-6Al-4V lattice structures

Using the Equations (3.3-3.5) of Energy absorption, Energy absorption efficiency, and Plateau stress were obtained and included in Table 4.8. The table demonstrates the Gyroid structures have good energy absorption (19.79±4.41 MJ/ m^3) and efficiency (2.05±0.18), as well as Plateau Stress (133.99±9.40 MPa), providing the highest value in comparison to other structures. Hence, considering Table 4.7 and Table 4.8, Gyroid structures have better mechanical properties than others. The lowest value of energy absorption and Plateau Stress have the Diamond structure with 20% density, which was the same in Ultimate Compression Stress and Yield Strength.

Table 4.8: Mechanical characterizations of the compressed Ti-6Al-4V lattice structures

Tested lattice structures	Energy absorption, MJ/ m^3	Energy absorption efficiency	Plateau stress, MPa
Gyroid (30% density, UCS=3)	19.79±4.41	2.05±0.18	133.99±9.40
Diamond (20% density, UCS=5)	2.62±1.14	1.8±0.56	46.61±3.23
Diamond (30% density, UCS=5)	7.24±4.41	1.75±0.53	102.38±7.17
Primitive (20% density, UCS=5)	4.64±2.57	1.65±0.46	129.71±9.10
Primitive (30% density, UCS=5)	12.33±8.01	1.77±0.54	131.13±9.20

Table 4.9 demonstrates the mechanical characterization of Ti-6Al-4V lattice structures for the following densities: 30%, 35%, and 40% with a unit cell size of 3 mm. This table presents the lattice structures' mechanical robustness and density by increasing yield strength and Ultimate Compression Stress at higher densities. The Diamond structure, for example, exhibits a significant increase in mechanical strength: Yield Strength increases from 107.89±1.61 MPa at 30% density to 168.2±2.52 MPa at 40% density, and Ultimate Compression Stress increases from 112.62±1.7 MPa to 180.02±2.63 MPa. The Gyroid and Primitive structures exhibit similar patterns in response, illustrating the relationship between increased density and mechanical effectiveness. Moreover, the Elastic Modulus differs in values among the studied lattice structures and densities, indicating the material's rigidity and deformation reaction under stress.

In contrast to other structures at higher densities, the Diamond lattice at 30% density exhibits a significantly higher Elastic Modulus of 6.17±0.12 GPa, indicating a stiffness modulation dependent on density. Although it does not meet the strength requirements considered essential for the best load-bearing bone support, this observation is consistent with theoretical expectations meant to minimize stress-shielding effects. However, in terms of Ultimate Tensile Strength (UTS) measurements, the Gyroid and Primitive lattice structures are more consistent with the biomechanical properties of human bone, suggesting that they could be used in situations involving the replacement or support of bone.

Table 4.9: Compression results of the Ti-6Al-4V lattice structures with UCS=3

Tested lattice structures	Yield Strength, MPa	Ultimate Compression Stress, MPa	Elastic Modulus, GPa
Diamond (30% density)	107.89±1.61	112.62±1.7	6.17±0.12
Diamond (35% density)	139.76±2.05	149.89±2.18	1.93±0.05
Diamond (40% density)	168.2±2.52	180.02±2.63	3.4±0.29
Gyroid (30% density)	137.81±1.76	153.14±1.96	2.38±0.27
Gyroid (35% density)	174.73±2.16	185.94±2.34	2.47±0.37
Gyroid (40% density)	209.33±2.45	219.3±2.57	3.2±0.14
Primitive (30% density)	144.7±2.08	154.61±2.23	2.2±0.14
Primitive (35% density)	176.98±2.43	193.36±2.63	2.41±0.29
Primitive (40% density)	220.55±3.11	229.11±3.19	2.73±0.19

Table 4.10 also illustrates the mechanical characterization of Ti-6Al-4V lattice structures for the following densities: 30%, 35%, and 40%, but with a UCS of 5. Similar to Table 4.9, an upward trend in both Yield Strength and Ultimate Compression Stress is observed as the density increases, indicating a consistent relationship between the density of the lattice structures and their mechanical capacities. However, a notable distinction arises in the Elastic Modulus values, which appear to be generally lower across all configurations and densities compared to those with a UCS of 3, suggesting that the larger unit cell size contributes to a decrease in stiffness, potentially offering a closer biomechanical match to natural bone and thereby reducing the risk of stress shielding. Analyzing Tables 4.9 and 4.10 reveals slight variations in mechanical behavior, particularly in elastic modulus. The two tables show the significant impact of density on mechanical strength. As an example, the Elastic Modulus of the Diamond structure with 40% density and UCS=3 is 3.4±0.29 GPa, which increases to 4.75±0.18 GPa with UCS=5. It indicates an implicit relationship between lattice density, cell size, and the resulting stiffness. On the other hand, gyroid structures exhibit a comparatively lower Elastic Modulus and a significant increase in both Yield and Ultimate Compression Stresss with higher UCS. Hence, it highlights the prospect of obtaining suitable mechanical integration with the surrounding biological tissue

by altering the UCS. For better visual understanding, Figure 4.14 represents the data from Tables 4.9 and 4.10, illustrating compression results of the Ti-6Al-4V lattice structures.

Table 4.10: Compression results of the Ti-6Al-4V lattice structures with UCS=5

Tested lattice structures	Yield Strength, MPa	Ultimate Compression Stress, MPa	Elastic Modulus, GPa
Diamond (30% density)	106.06±1.64	112.49±1.75	3.72±0.20
Diamond (35% density)	134.03±2.19	141.48±2.29	4.6±0.28
Diamond (40% density)	171.9±2.64	182.33±2.74	4.75±0.18
Gyroid (30% density)	128.74±1.89	149.71±2.03	1.65±0.25
Gyroid (35% density)	150.12±2.11	189.52±2.4	1.83±0.12
Gyroid (40% density)	188.70±1.20	220.49±1.37	3.22±0.16
Primitive (30% density)	129.6±2.02	140.31±2.14	2.45±0.32
Primitive (35% density)	169.24±2.58	184.94±2.7	3.03±0.02
Primitive (40% density)	213.35±1.32	222.49±1.37	2.65±0.25

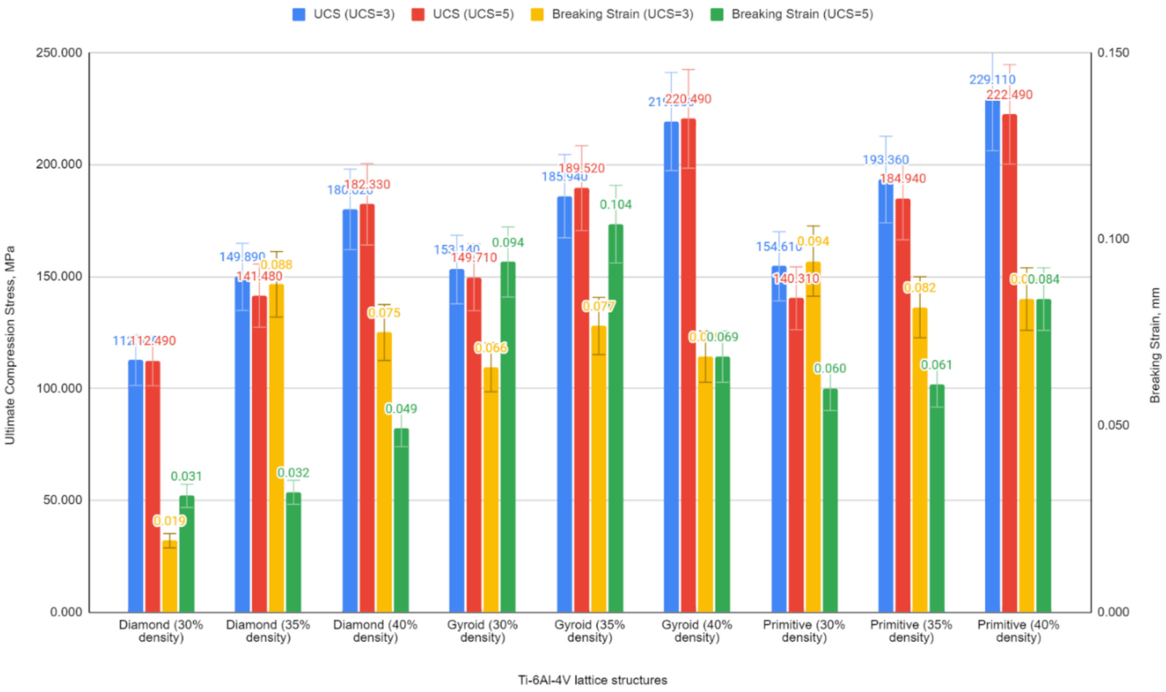

Figure 4.14: Compression results of the Ti-6Al-4V lattice structures

Table 4.11 provides the energy absorption properties of compressed Ti-6Al-4V lattice structures with the UCS of 3. It can be seen that the Gyroid lattice at 40% density has the maximum efficiency (0.67±0.24) and energy absorption (37.71±0.21 MJ/m^3) along with the highest plateau stress (146.08±0.06 MPa). The results show that the implant has an excellent energy absorption capacity and an efficient stress distribution, both desirable characteristics for implants that are expected to endure both impacts and physiological stresses. A drop in efficiency is observed in the Diamond design despite a progressive increase in energy absorption and plateau stress with density. This suggests that although the structure improves its energy absorption capacity, it does so less effectively at greater densities. The Primitive lattice structure exhibits a remarkable equilibrium between high energy absorption and efficiency, especially at 30% density, when it exhibits the highest efficiency (0.72±0.2) of all the investigated designs. This implies that under dynamic loading conditions, the Primitive structure at this density might provide the best possible combination of energy dissipation and stress distribution capabilities, lowering the probability of implant failure.

Table 4.11: Mechanical characterizations of the compressed Ti–6Al–4V lattice structures with UCS=3

Tested lattice structures	Energy absorption, MJ/ m^3	Energy absorption efficiency	Plateau stress, MPa
Diamond (30% density)	11.43±0.31	0.63±0.26	71.2±0.14
Diamond (35% density)	15.16±0.11	0.59±0.29	88.82±0.13
Diamond (40% density)	15.53±0.33	0.54±0.33	96.87±0.09
Gyroid (30% density)	21.83±0.12	0.57±0.3	87.71±0.2
Gyroid (35% density)	26.35±0.25	0.57±0.3	105.93±0.05
Gyroid (40% density)	37.71±0.21	0.67±0.24	146.08±0.06
Primitive (30% density)	21.12±0.08	0.72±0.2	110.72±0.2
Primitive (35% density)	23.11±0.08	0.54±0.33	104.58±0.3
Primitive (40% density)	22.11±0.08	0.57±0.31	130.24±0.17

Table 4.12 continues the discussion of the mechanical characterizations of Ti-6Al-4V lattice structures, but now for Diamond, Gyroid, and Primitive configurations at different densities (30%, 35%, and 40%), using a Unit Cell Size (UCS) of 5.

Table 4.12: Mechanical characterizations of the compressed Ti–6Al–4V lattice structures with UCS=5

Tested lattice structures	Energy absorption, MJ/ m^3	Energy absorption efficiency	Plateau stress, MPa
Diamond (30% density)	10.58±0.3	0.6±0.3	67.69±0.22
Diamond (35% density)	13.54±0.33	0.61±0.28	86.17±0.12
Diamond (40% density)	14.8±0.14	0.52±0.34	94.51±0.34
Gyroid (30% density)	15.42±0.3	0.47±0.37	70.53±0.38
Gyroid (35% density)	23.46±0.33	0.48±0.37	91.21±0.15
Gyroid (40% density)	25.43±0.3	0.62±0.27	137.64±0.26
Primitive (30% density)	12.86±0.1	0.52±0.34	73.11±0.08
Primitive (35% density)	15.87±0.1	0.48±0.37	89.47±0.33
Primitive (40% density)	25.43±0.3	0.62±0.27	137.64±0.26

The compression results reveal that the mechanical behavior of the lattice structures can be affected by an increase in UCS from 3 to 5. For example, Tables 4.12 and 4.11 demonstrate an insignificant decline in energy absorption efficiency (Figure 4.15). However, Table 4.12's Gyroid structure at 40% density is notable in both tables for its improved energy absorption capabilities and plateau stress (Figure 4.16). As a result, implants subjected to dynamic loads may benefit from the higher UCS's ability to sustain or improve the structure's capacity to absorb energy and endure higher plateau stresses, even though it may have a minor negative impact on energy dissipation efficiency.

In contrast, in Table 4.12, the Diamond structure demonstrates a slight reduction in energy absorption and efficiency as UCS increases. It suggests that cell size has a complex impact on the mechanical performance of these structures. A similar pattern can be seen in the Primitive structure, where energy absorption capabilities and efficiency alter due to a higher UCS. Hence, it affects its mechanical strength and energy distribution efficiency. The difference between Tables 4.11 and 4.12 shows the significance of unit cell size to the mechanical performance of lattice structures, especially in terms of how dynamically they respond to applied loads. Although the Gyroid and Primitive patterns are highlighted in both tables (Tables 4.11 and 4.12) as potentially better suited for applications, they require high energy absorption and stress distribution. The change in UCS indicates a compromise to withstand and distribute stresses and energy absorption efficiency. This study provides insights into optimizing lattice designs for particular mechanical needs in biomedical implants. As a result, this knowledge helps to customize implants for dynamic resilience as well as static mechanical compatibility with bone.

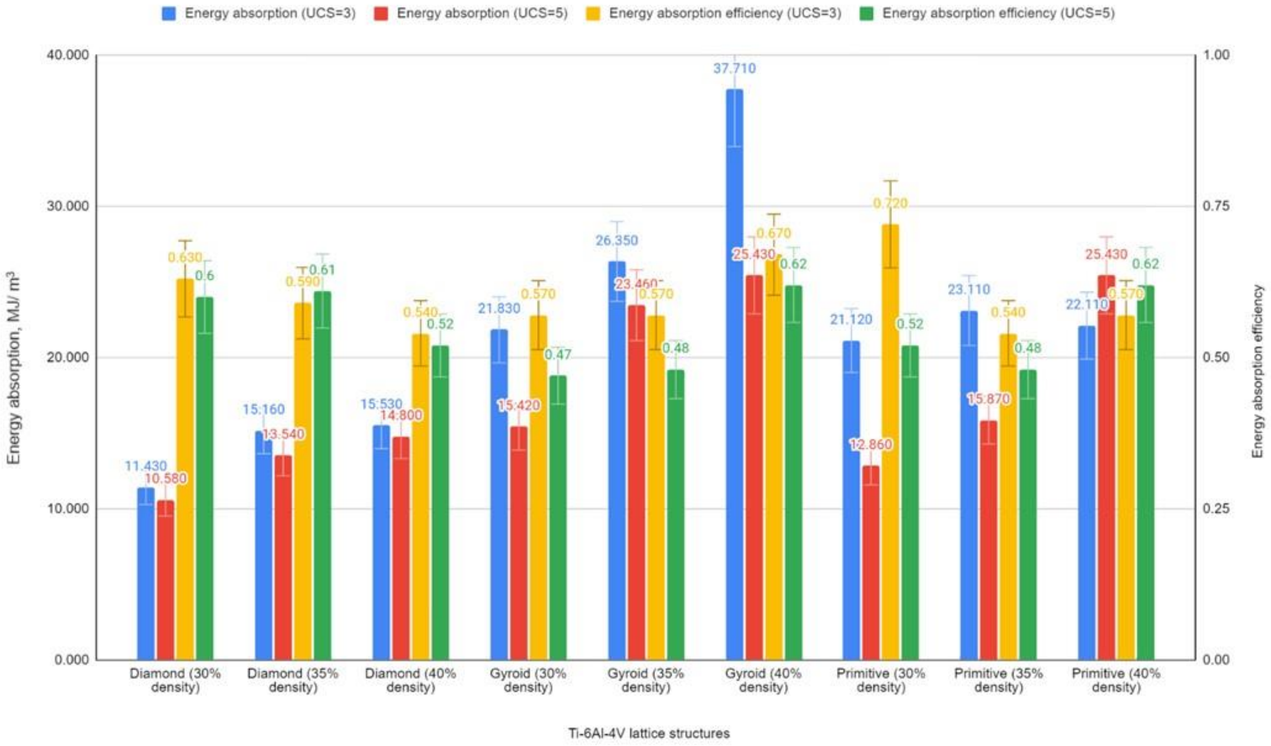

Figure 4.15: Energy absorption data of the compressed Ti–6Al–4V lattice structures

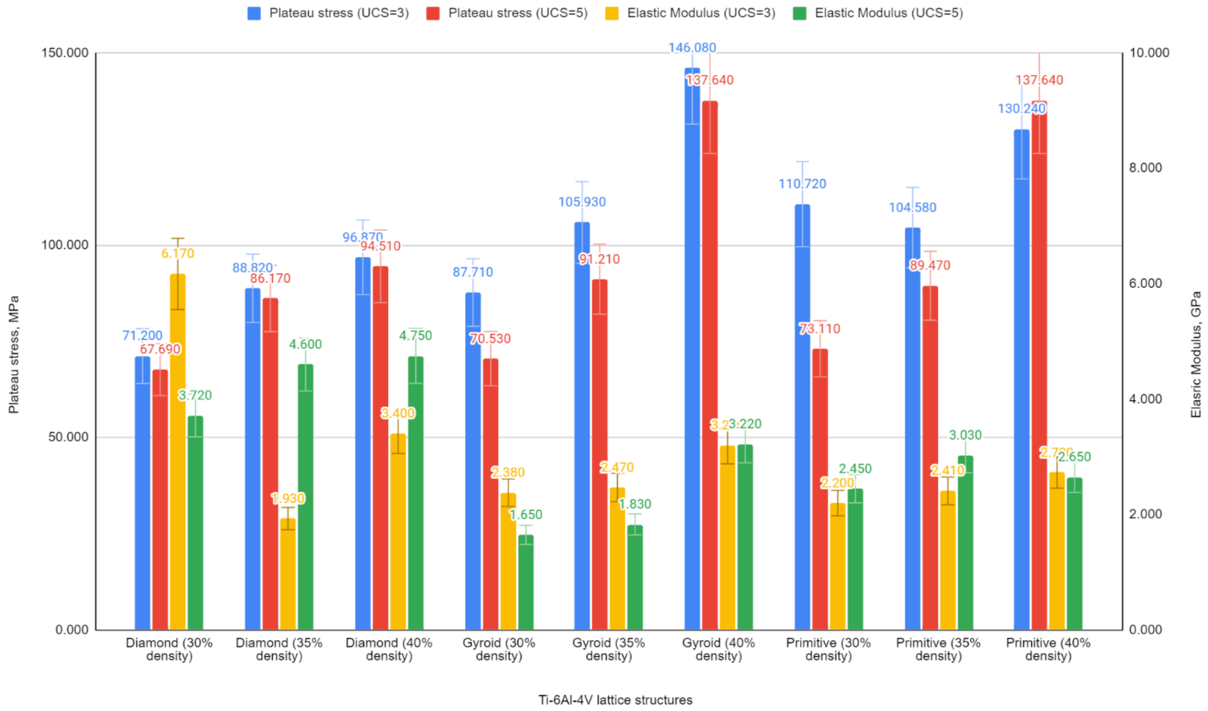

Figure 4.16: Plateau Stress and Elastic Modulus data of the Ti-6Al-4V lattice structures

4.4.2 Ti–6Al–4V-Ta

The mechanical properties of Ti-6Al-4V lattice structures alloyed with 8% Tantalum (Ta) addition are presented in Table 4.13. The densities of 30%, 35%, and 40% are covered, and the same Unit Cell Size of 3 remains as for Ti-6Al-4V lattice structures. Compared to the previously discussed pure Ti-6Al-4V structures in tables 4.9 and 4.10, this addition of Ta is to investigate its effect on the mechanical properties, particularly Yield Strength, Ultimate Compression Stress, and Elastic Modulus. Compared to pure Ti-6Al-4V compositions, adding 8% Ta tends to improve the mechanical strength of the lattice structures across all densities. For example, the Diamond structure in pure Ti-6Al-4V gradually increases strength with density; however, adding Ta improves these strength values even further, especially at higher densities, indicating that Ta alloying enhances the material's ability to support loads. In addition, Fig 4.17 visually illustrates the Stress-Strain results between compressed Ti-6Al-4V and Ti-6Al-4V-Ta lattice structures with UCS=3.

Table 4.13: Compression results of the Ti-6Al-4V-Ta lattice structures with UCS=3

Tested lattice structures	Yield Strength, MPa	Ultimate Compression Stress, MPa	Elastic Modulus, GPa
Diamond (30% density)	37.15±0.28	92.78±0.55	1.55±0.32
Diamond (35% density)	132.213±0.83	137.92±0.87	1.85±0.11
Diamond (40% density)	162.65±1.11	174.93±1.09	1.13±0.1
Gyroid (30% density)	113.28±0.5	144.89±0.84	1.67±0.24
Gyroid (35% density)	145.44±0.98	182.78±1.01	2.24±0.17
Gyroid (40% density)	162.26±0.88	226.705±1.08	1.6±0.29
Primitive (30% density)	132.63±0.84	143.98±0.93	2.08±0.06
Primitive (35% density)	166.54±1.04	182.19±1.13	2.37±0.26
Primitive (40% density)	214.27±1.26	226.32±1.33	4.03±0.02

As can be noticed from Table 4.13, the Ti-6Al-4V + 8% Ta structures exhibit a more comprehensive range of fluctuation in the elastic modulus. For instance, the Elastic Modulus (4.03±0.02 GPa) of the Primitive configuration at 40% density with Ta addition is significantly higher than that of its pure Ti-6Al-4V counterpart. This suggests a stiffer material, which may be less suitable for some implant applications because of the possibility of stress shielding. Nevertheless, Ta's addition alters mechanical properties, demonstrating a trade-off between obtaining more incredible mechanical strengths and maintaining an elastic modulus similar to natural bone. On the other hand, applications needing more mechanical support might benefit from this enhanced rigidity.

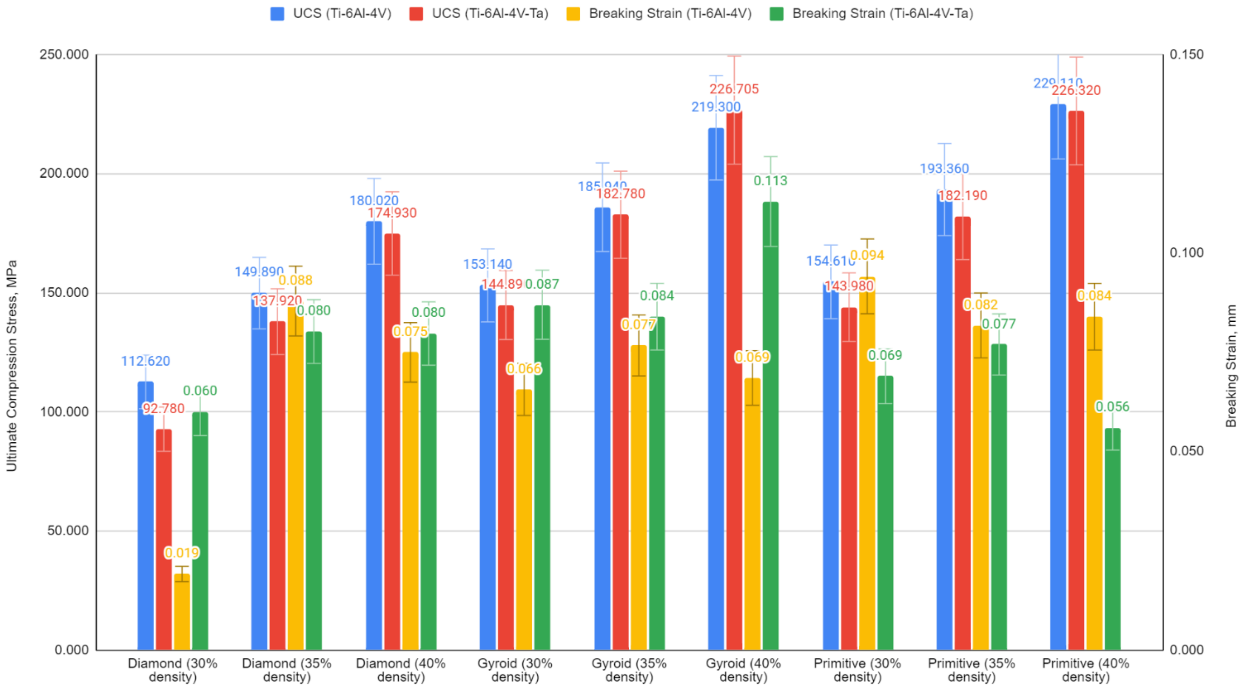

Figure 4.17: Compression results of the Ti-6Al-4V and Ti-6Al-4V-Ta lattice structures

The mechanical properties of Ti-6Al-4V lattice structures alloyed with 8% Tantalum (Ta) are reviewed in Table 4.14. The variables of interest are plateau stress, energy absorption efficiency, and energy absorption characteristics. All configurations are set to a uniform Unit Cell Size (UCS) of 3. Ta significantly improves the energy absorption capacity in all forms and densities. Compared to its pure Ti-6Al-4V counterparts, the Gyroid configuration at 40% density, for example, shows a significant increase in energy absorption (34.75±0.53 MJ/m^3). Hence, it suggests that Ta alloying improves the material's ability to dissipate energy, which is an acceptable attribute for implants meant to withstand dynamic loads. Ta increases energy absorption, but the energy absorption efficiency presents a more nuanced perspective. For example, the Diamond structure with 30% density exhibits an exceptionally high efficiency (0.88) by adding Ta. It demonstrates that the material composition may majorly affect its capacity to dissipate energy. This minor phenomenon highlights how crucial material composition is to improving the dynamic mechanical performance of implants. Ti-6Al-4V-Ta also increases the plateau stress, which measures the stress level at which the material deforms plastically under continuous load. For instance, compared to pure Ti-6Al-4V structures, the Gyroid structure with 40% density with Ta exhibits a higher plateau stress (143.24 MPa). Hence, it implies that the alloyed material may withstand higher stresses before experiencing permanent deformation. For a better visual representation of mechanical characterizations between compressed Ti–6Al–4Vand Ti-6Al-4V-Ta lattice structures with UCS=3, Figures 4.18 and 4.19 are given.

Table 4.14: Mechanical characterizations of the compressed Ti-6Al-4V-Ta lattice structures with UCS=3

Tested lattice structures	Energy absorption, MJ/ m^3	Energy absorption efficiency	Plateau stress, MPa
Diamond (30% density)	12.81±0.14	0.88±0.09	81.60±0.28
Diamond (35% density)	15.98±0.1	0.67±0.23	92.54±0.32
Diamond (40% density)	19.86±0.61	0.75±0.18	130.79±0.56
Gyroid (30% density)	18.17±012	0.65±0.24	94.72±0.51
Gyroid (35% density)	26.27±0.19	0.68±0.22	124.86±0.1
Gyroid (40% density)	34.75±0.53	0.63±0.26	143.24±0.17
Primitive (30% density)	17.4±0.28	0.62±0.27	89.81±0.13
Primitive (35% density)	22.88±0.08	0.62±0.27	112.62±0.27
Primitive (40% density)	29.21±0.15	0.63±0.26	142.97±0.02

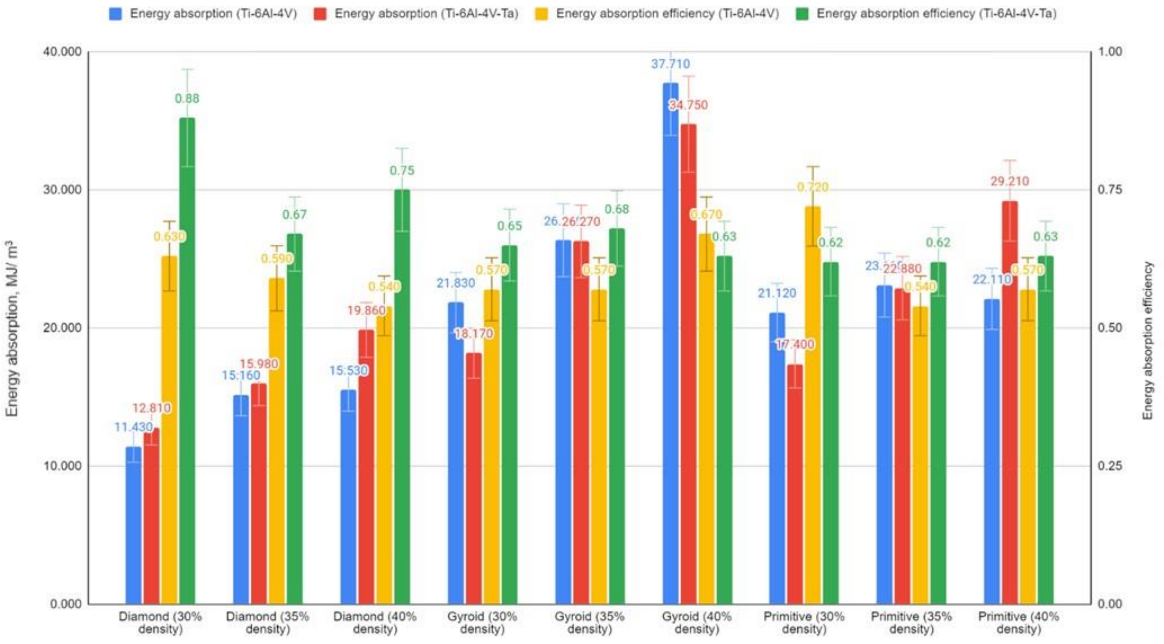

Figure 4.18: Energy absorption data of the compressed Ti–6Al–4Vand Ti-6Al-4V-Ta lattice structures

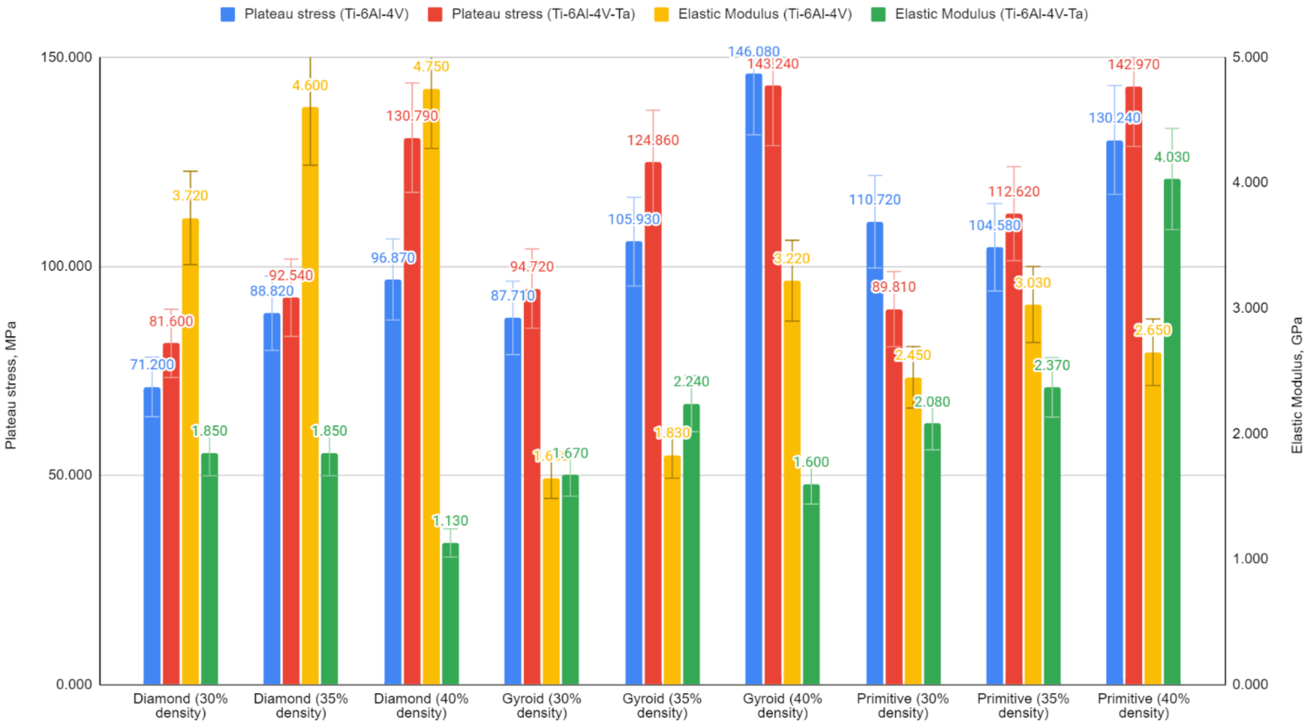

Figure 4.19: Plateau Stress and Elastic Modulus data of the compressed Ti–6Al–4Vand Ti-6Al-4V-Ta lattice structures

In contrast, Ta added to Ti-6Al-4V considerably improves the mechanical properties (as shown by the higher energy absorption and plateau stress in Table 4.14) and the static mechanical properties (as seen in Tables 4.9 and 4.10). This means that in applications such as load-bearing bone implants, where both high mechanical integrity and effective energy dissipation are crucial, Ti-6Al-4V + 8% Ta may perform better. In order to maximize the benefits of Ta alloying, implant designers require an individual strategy that prioritizes optimizing energy absorption efficiency across a range of geometry and densities.

4.5 Corrosion test

4.5.1 Ti–6Al–4V ELI

Table 4.15 reviews the electrochemical corrosion behaviors of SLM-printed Ti–6Al–4V alloys. This analysis carefully evaluates factors such as corrosion rates and sample density, which shed information about how well certain alloys withstand corrosive environments.

The densities of the samples used for the electrochemical corrosion tests vary between 4 and 5 g/cm by Archimedes. The corrosion current density (i_{corr}) values range from 5.63 µA/cm² to 8.19 µA/cm², which shows the alloy's potential dissolution rate in the surrounding media. Lower i_{corr} values, such as 5.63 µA/cm², suggest a less rapid dissolution rate and a stronger corrosion resistance. This study is further enhanced by using corrosion potential (E_{corr}), which has a spectrum ranging from -0.10 V to -0.13 V. Positively skewed materials tend to have a lower predisposition for active corrosion, indicating a natural durability in the material. With values ranging from 3212.18 Ω.cm² to 10765 Ω.cm², polarization resistance (R_p), according to the diagram in Figure 3, provides additional knowledge. The resistance to charge transfer and corrosion is strongly enhanced at the higher end of this scale, highlighting the alloys' capacity to retain their integrity in corrosive circumstances. The corrosion rates, which vary from 0.01 to 0.16, show how directly i_{corr} affects the longevity of materials; lower rates indicate a material's ability to resist corrosive degradation.

Table 4.15: Electrochemical parameters for the Ti–6Al–4V alloys

Sample number	Density, g/cm^3	i_{corr} (μA/cm^2)	E_{corr} (V)	R_p (Ω.cm^2)	Corrosion rate, mm/a	OCP, V
1	5	7.87	-0.10	10765	0.01	-0.01
2	4	5.63	-0.11	6309.9	0.11	-0.02
3	4	8.19	-0.13	3212.18	0.16	-0.04

A visual representation of the electrochemical corrosion of the alloys is provided in Figures 4.20, which supplement Table 4.15. The temporal stability and nobility of the alloys' surface potentials in a corrosive environment are shown by the OCP versus time curves in Figure 4.11, indicating a persistent passive coating that reduces corrosion vulnerability. Figure 4.21 shows the impedance across frequencies using Electrochemical Impedance Spectroscopy (EIS) curves. The impedance readings, particularly the ones that correspond with the higher Rp values in Table 4.15, highlight a strong defense against processes that promote corrosion. These high values indicate strong corrosion resistance. Potentiodynamic polarization curves, shown in Figure 4.22 based on OCP values in Table 4.15, identify the relation between applied potential and generated current to reveal the corrosion rate. The alloy's ability to maintain a protective oxide layer in the face of corrosive threats is demonstrated by reduced i_{corr} values, which suggest a lessened corrosion inclination.

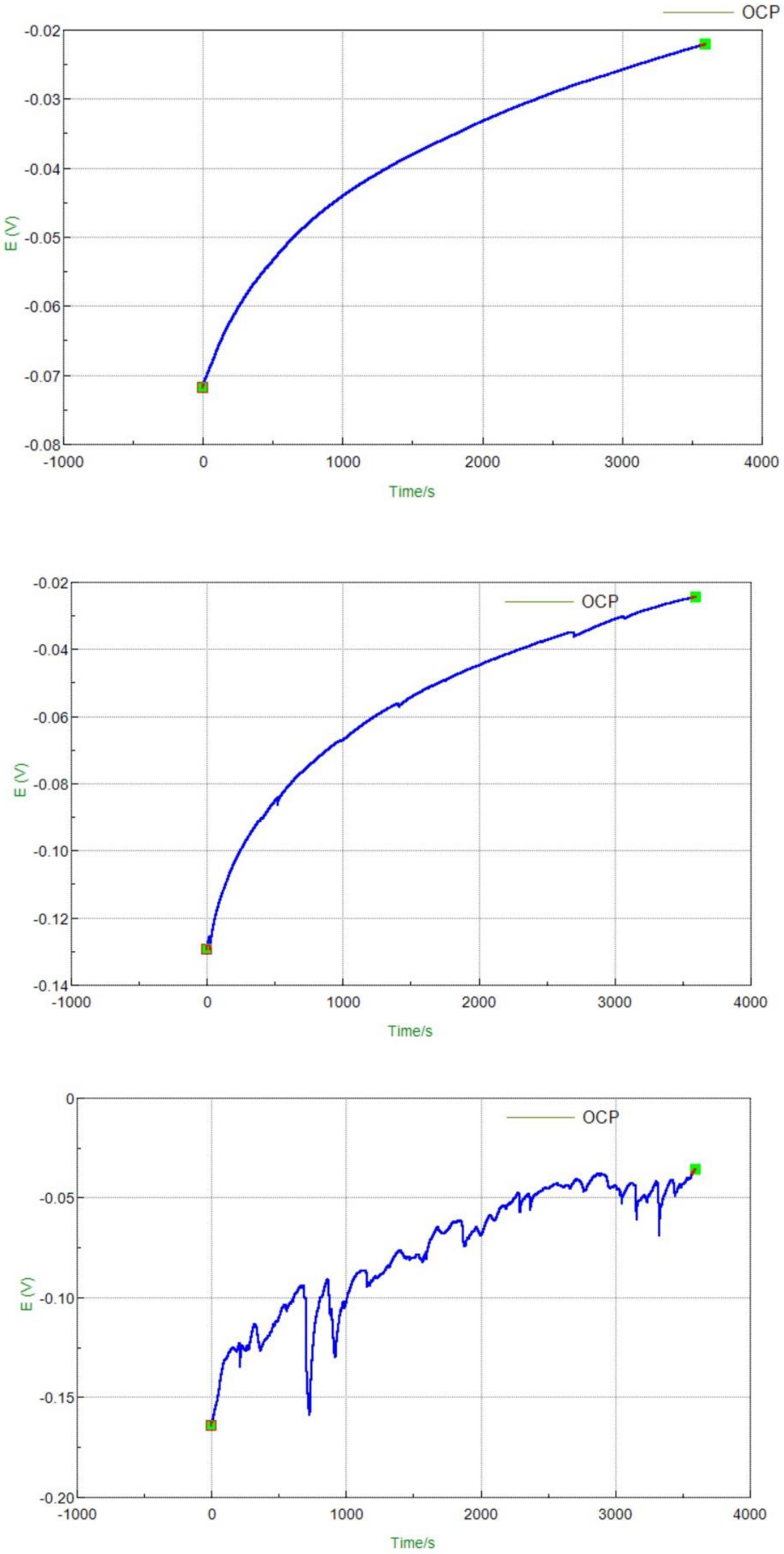

Figure 4.20: OCP vs. time curves of the Ti-6Al-4V samples

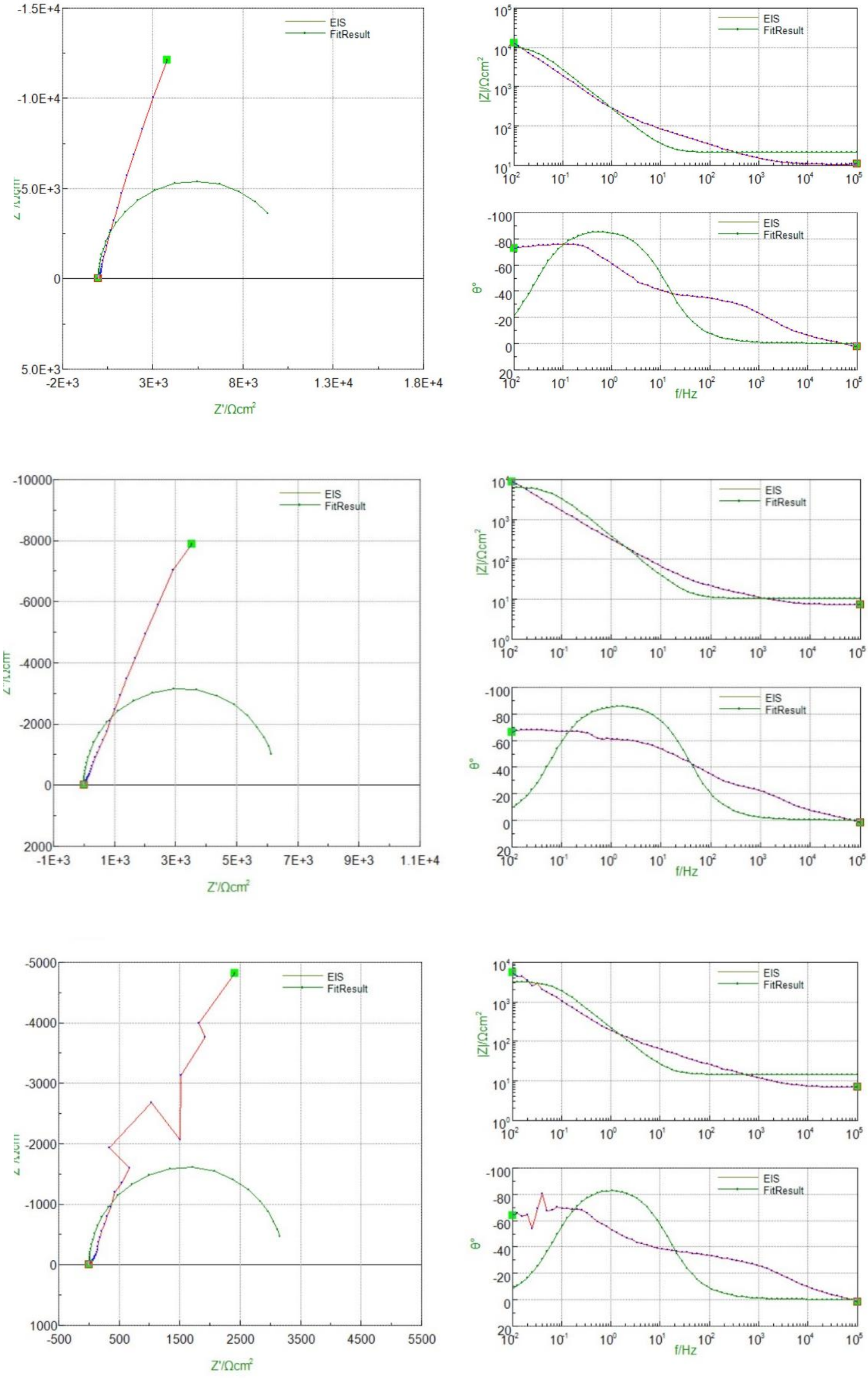

Figure 4.21: Electrochemical impedance spectroscopy curves of the Ti-6Al-4V samples

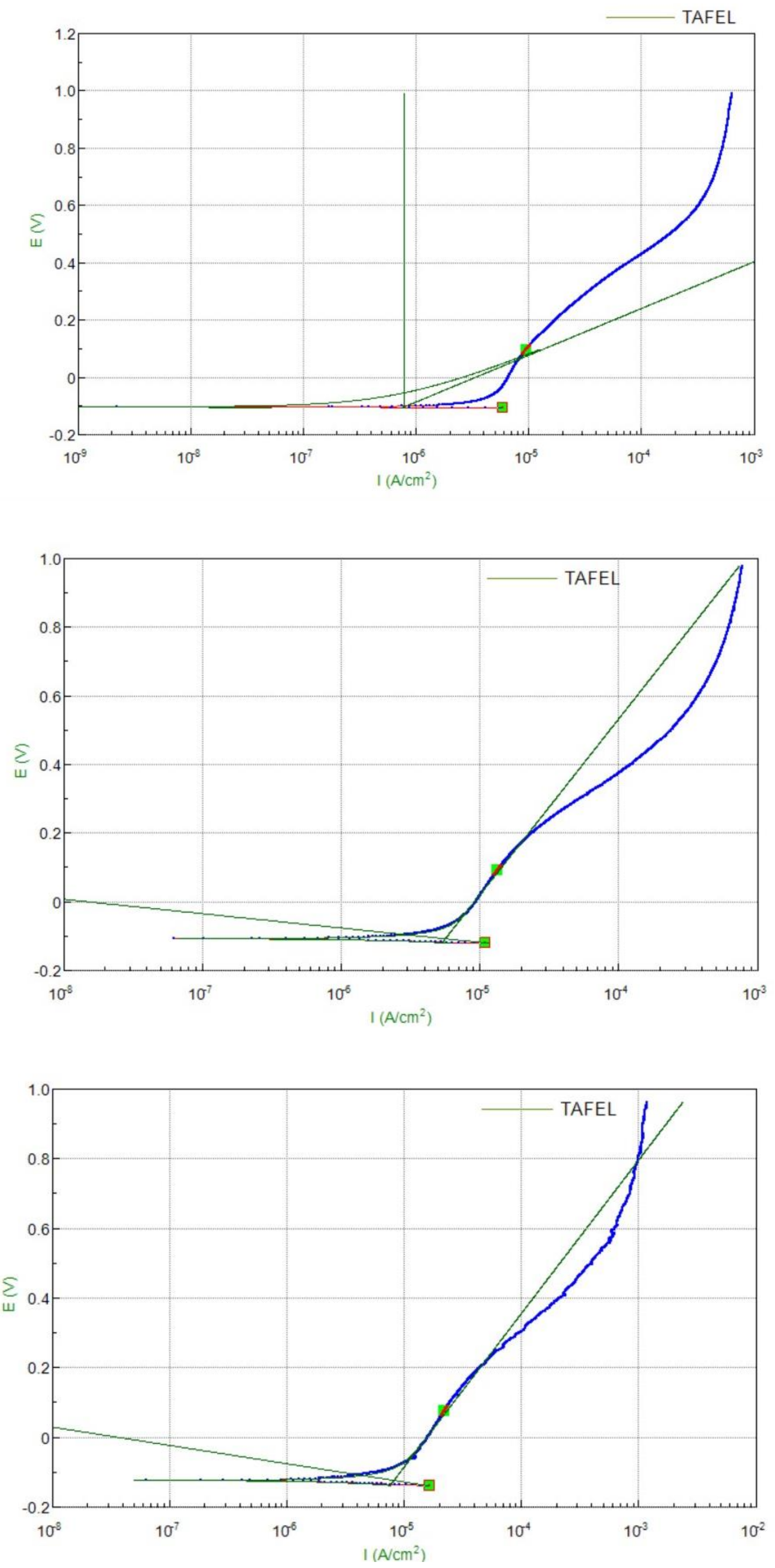

Figure 4.22: Potentiodynamic polarization curves of the Ti-6Al-4V samples

Integrating all of this information, the SLM-printed Ti–6Al–4V alloys may have remarkable corrosion resistance, as shown by their low corrosion rates, constant corrosion potentials, increased resistance to polarization, and the behaviors seen in electrochemical corrosion tests. These characteristics make the alloys suitable for use in biomedical implant situations.

Figure 4.23 represents the Surface morphology of the Ti-6Al-4V specimen after corrosion tests.

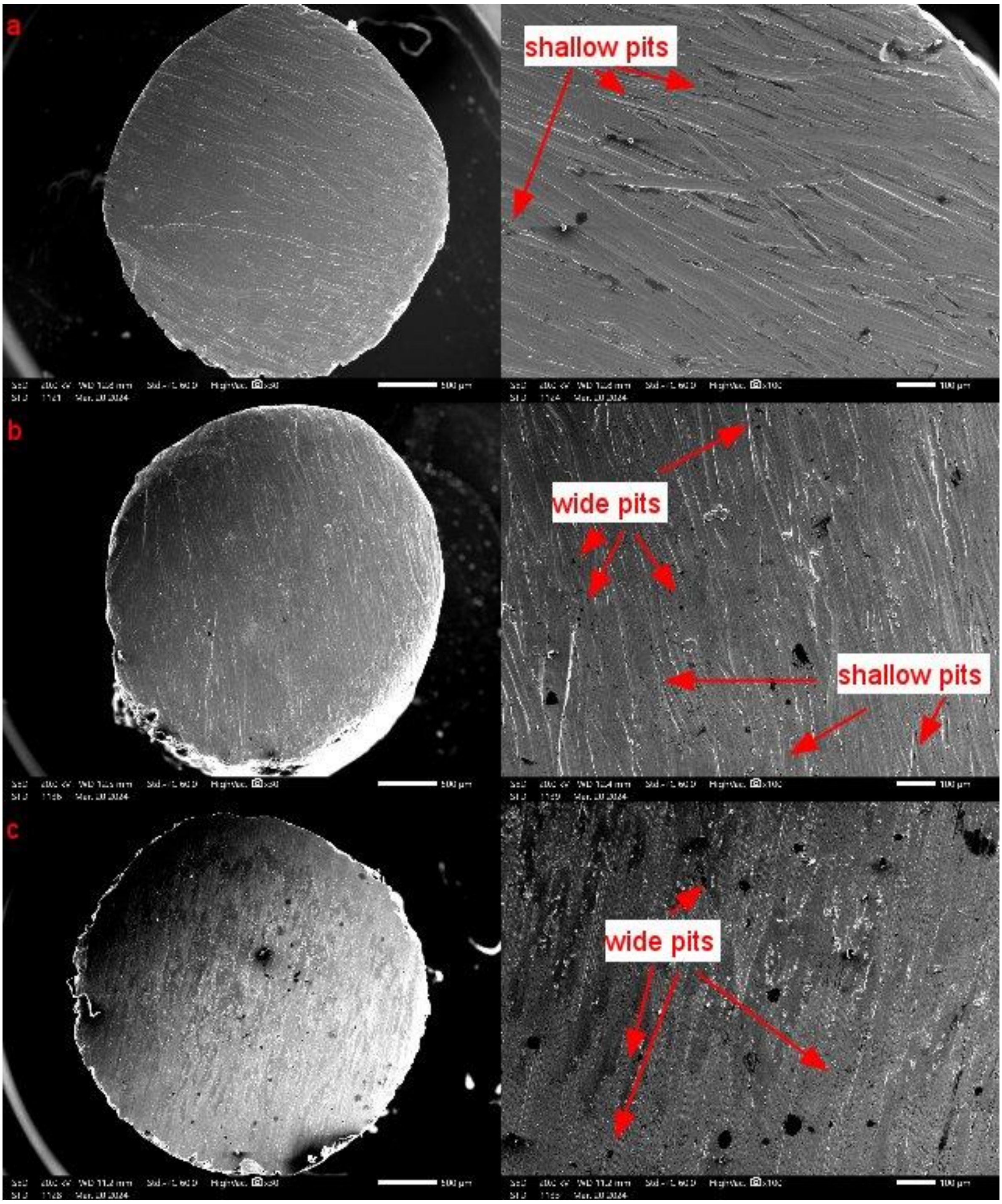

Figure 4.23: Surface morphology after corrosion tests of the Ti-6Al-4V samples

This Scanning Electron Microscopy (SEM) image set offers a detailed visual inspection of Ti-6Al-4V alloy samples with labels a, b, and c. Electrochemical corrosion testing is one of the most essential assessments these specimens have undertaken to determine their suitability for medical implantation. Initial observations made at 30x magnification provide information about the global surface morphology following corrosion, while a comprehensive analysis of the damage caused is made easier with higher magnification at 100x. The study demonstrates two primary forms of oxidation: wide and shallow pits. Wide pits indicate extensive material dissolution over larger areas and may be related to microstructural inconsistencies as phase variations or localized residual stresses inherent to the additive manufacturing process. On the other hand, shallow pits demonstrate superficial material removal, suggesting either a homogeneous corrosion process or the beginning of pitting corrosion [45]. The alloy's corrosion resistance uniformity was assessed by comparing the corrosion patterns of the three specimens, which provided high corrosion resistance of the SLM-printed samples.

4.5.2 Ti–6Al–4V-Ta

The electrochemical parameters (i.e., corrosion current density, corrosion potential, polarization resistance, corrosion rate) and results of corrosion assessments for the SLM Ti–6Al–4V–Ta alloys are presented in Table 4.16. These indices are essential for evaluating how resistant the alloy is to electrochemical degradation.

Table 4.16: Electrochemical parameters for the Ti–6Al–4V-Ta alloys

Sample number	Density, g/cm^3	i_{corr} (μA/cm^2)	E_{corr} (V)	R_p (Ω.cm^2)	Corrosion rate, mm/a	OCP, V
1	4.824	1.73	-0.33	31743	0.03	-0.24
2	4.432	1.62	-0.3	31389	0.03	-0.22
3	4.882	2.33	-0.29	10511	0.07	-0.34

The corrosion current density, or i_{corr} indicates the rate at which metal dissolves. Samples 1 and 2 have lower i_{corr} values of 1.73 and 1.62 μA/cm^2, respectively, indicating a slower rate of corrosion and significant corrosion resistance. Slightly higher than average i_{corr} value (3.9 μA/cm^2) for sample 3 is within the acceptable range for use in biomedicine, indicating a low metal loss rate. The Corrosion Potential (E_{corr}) indicates how likely an alloy is to corrode in a given environment. The negative values, which range from -0.33 V to -0.29 V, are typical of titanium alloys and suggest that the alloy adopts a more cathodic position, which is beneficial for preventing corrosion.

The measurement of polarization resistance (Rp) (Figure 3.7) indicates the effective passive film deposition on the surface of the alloy. It measures the barrier to charge exchange across the electrode-electrolyte interface. Sample 3 (10511 $\Omega.cm^2$) has a lower Rp metric, which suggests a decline in this defense but still highlights a high level of corrosion resistance. The exceptionally low corrosion rates (0.03 mm/year for samples 1 and 2 and 0.07 mm/year for sample 3) indicate that the material is depleted trivially over time. In a physiological situation, implant materials that require lasting stability and completeness must have this minimal corrosion rate.

Open Circuit Potential vs. Time is shown in Figure 4.24. Consistency and amplitude of the OCP results (Figure 4.13), in agreement with the Ecorr data presented in Table 4.16, support the formation of a stable and shielding passive layer on the Ti-6Al-4V-Ta interface. Electrochemical Impedance Spectroscopy is illustrated in Figure 4.25. The wide semicircles or high impedance values shown in Figure 4.25 agree with the high R_p values in Table 4.16, indicating even more strength in the alloy's resistance to corrosion. Potential-dynamic Polarization is depicted in Figure 4.26 based on OCP values in Table 4.16. Explaining the passivation behavior and pitting resistance helps highlight the alloy's robustness against localized and broad corrosion processes, especially when combined with Table 4.16's low corrosion metrics.

Figure 4.27 offers the SEM images of Ti-6Al-4V-8Ta alloy samples after chemical corrosion tests at 30x and 100x magnifications, respectively. Throughout all of the corrosion-tested specimens made of Ti-6Al-4V-8Ta, "shallow pits" appear. It suggests localized corrosion events that only show surface penetration. This may indicate the beginning of pitting corrosion or a propensity for more passive corrosion tendencies, possibly due to the tantalum infusion. In contrast, "wide pits" reveal more substantial material degradation over larger areas. It indicates either electrochemical instability or compositional inhomogeneities in the alloy matrix. These variations in corrosion morphology, which range from narrow to large pits, are crucial for determining how tantalum addition affects the alloy to resist the corrosive demands of the environment inside the human body.

The Ti-6Al-4V-8Ta alloy exhibits better corrosion resistance than the Ti-6Al-4V alloy, which is probably because tantalum stabilizes the oxide layer and promotes passivity. This can be seen by examining the SEM images for both alloys after corrosion testing. If the micrographs show fewer pits and smaller pit sizes in the Ti-6Al-4V-8Ta samples than in the Ti-6Al-4V samples, this would indicate that the material is less vulnerable to localized corrosive effects. The Ti-6Al-4V-8Ta alloy is now positioned as a better option for such crucial applications, indicating a longer service life and a reduced chance of corrosion-related problems. This development is vital for medical implants.

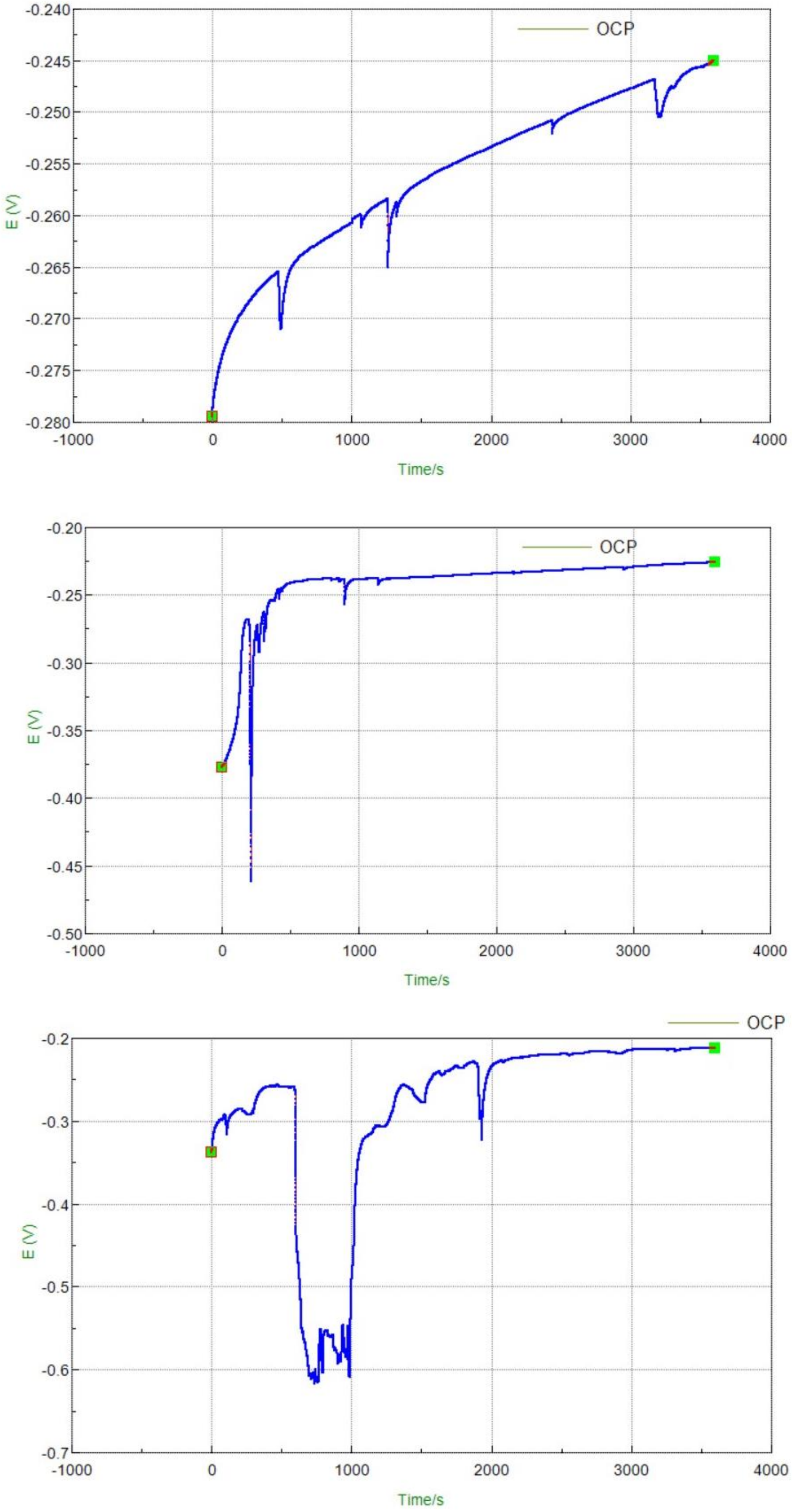

Figure 4.24: OCP vs. time curves of the Ti-6Al-4V-Ta samples

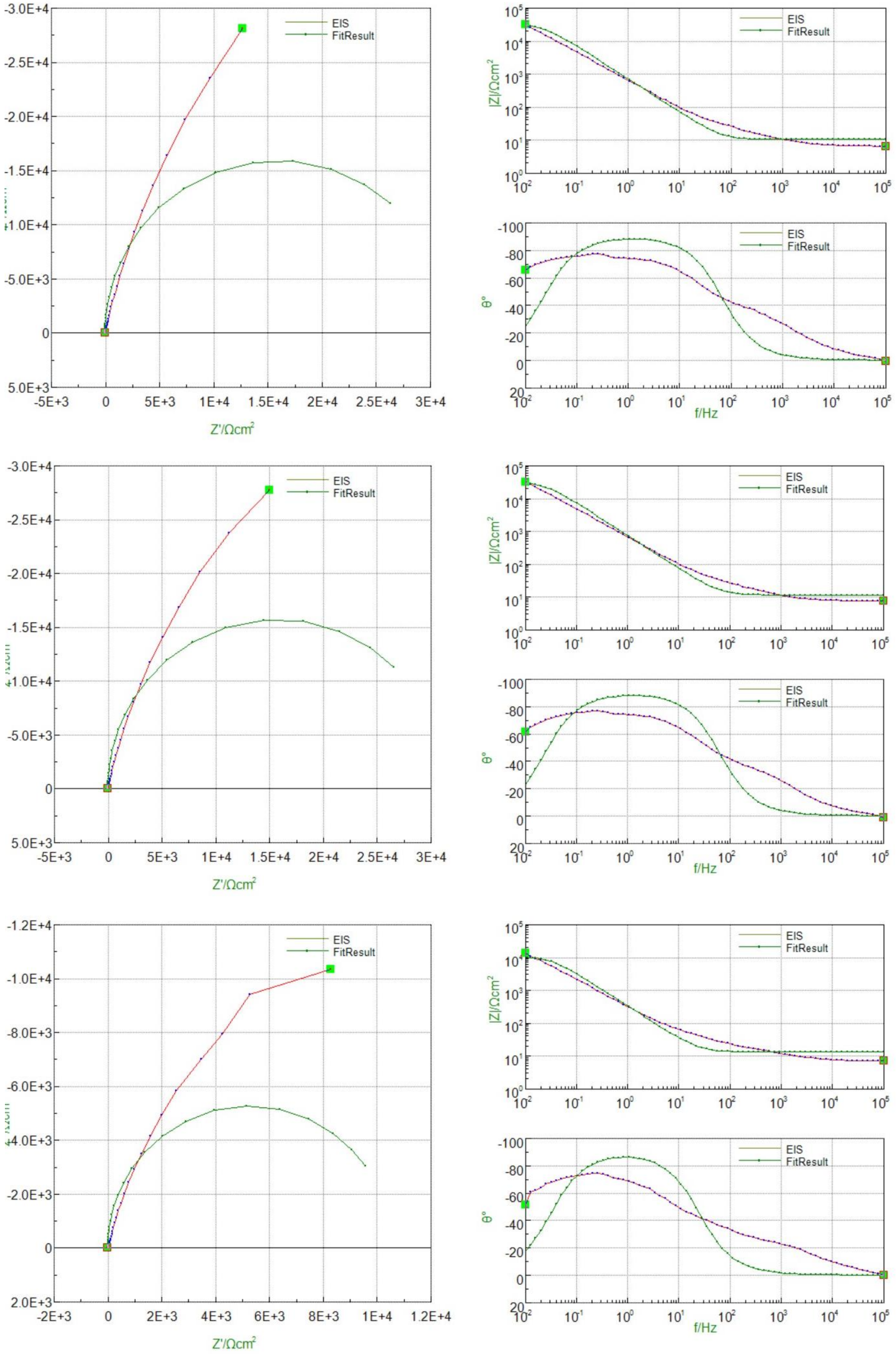

Figure 4.25: Electrochemical impedance spectroscopy curves of the Ti-6Al-4V-Ta samples

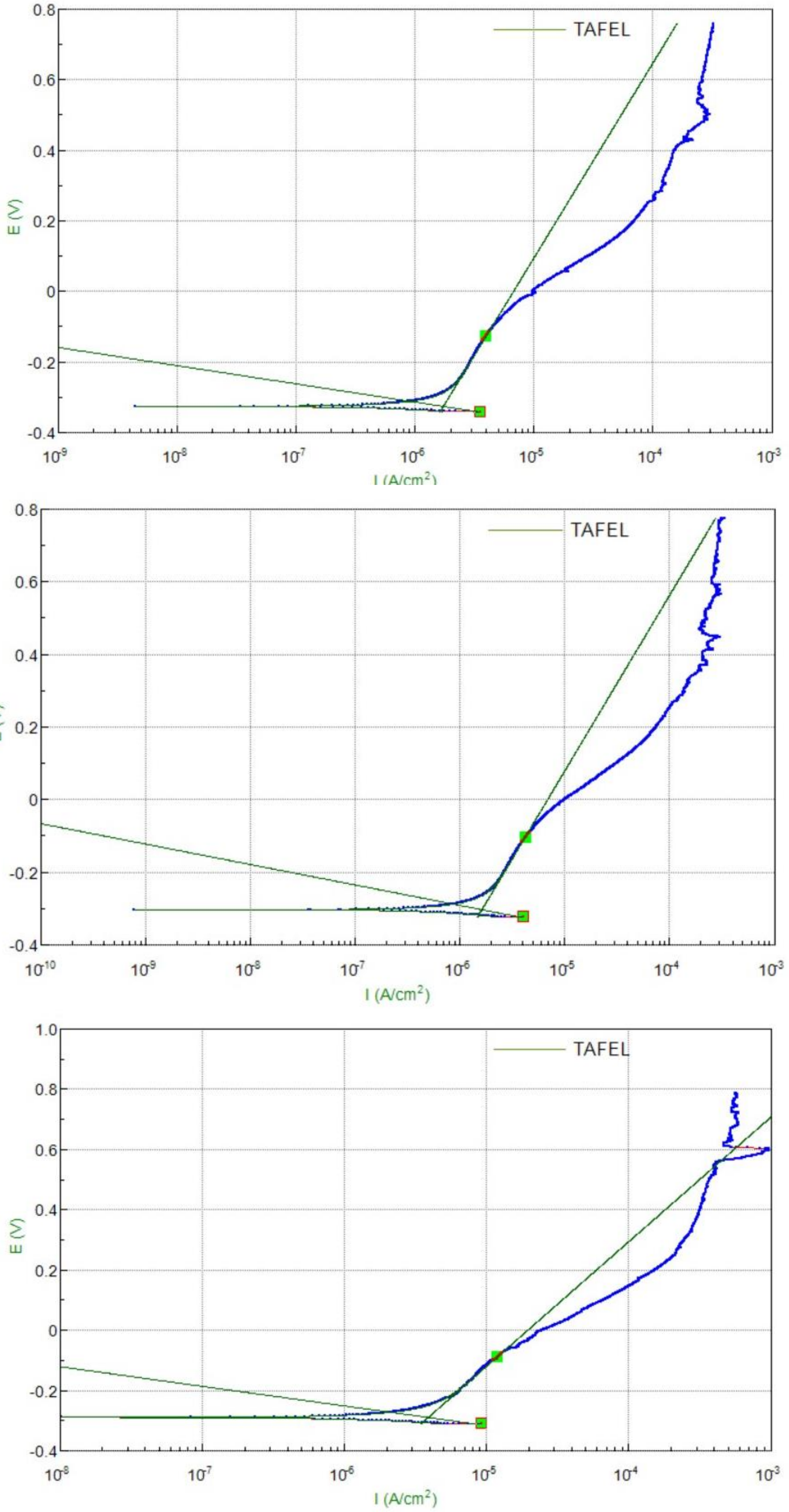

Figure 4.26: Potentiodynamic polarization curves of the Ti-6Al-4V-Ta samples

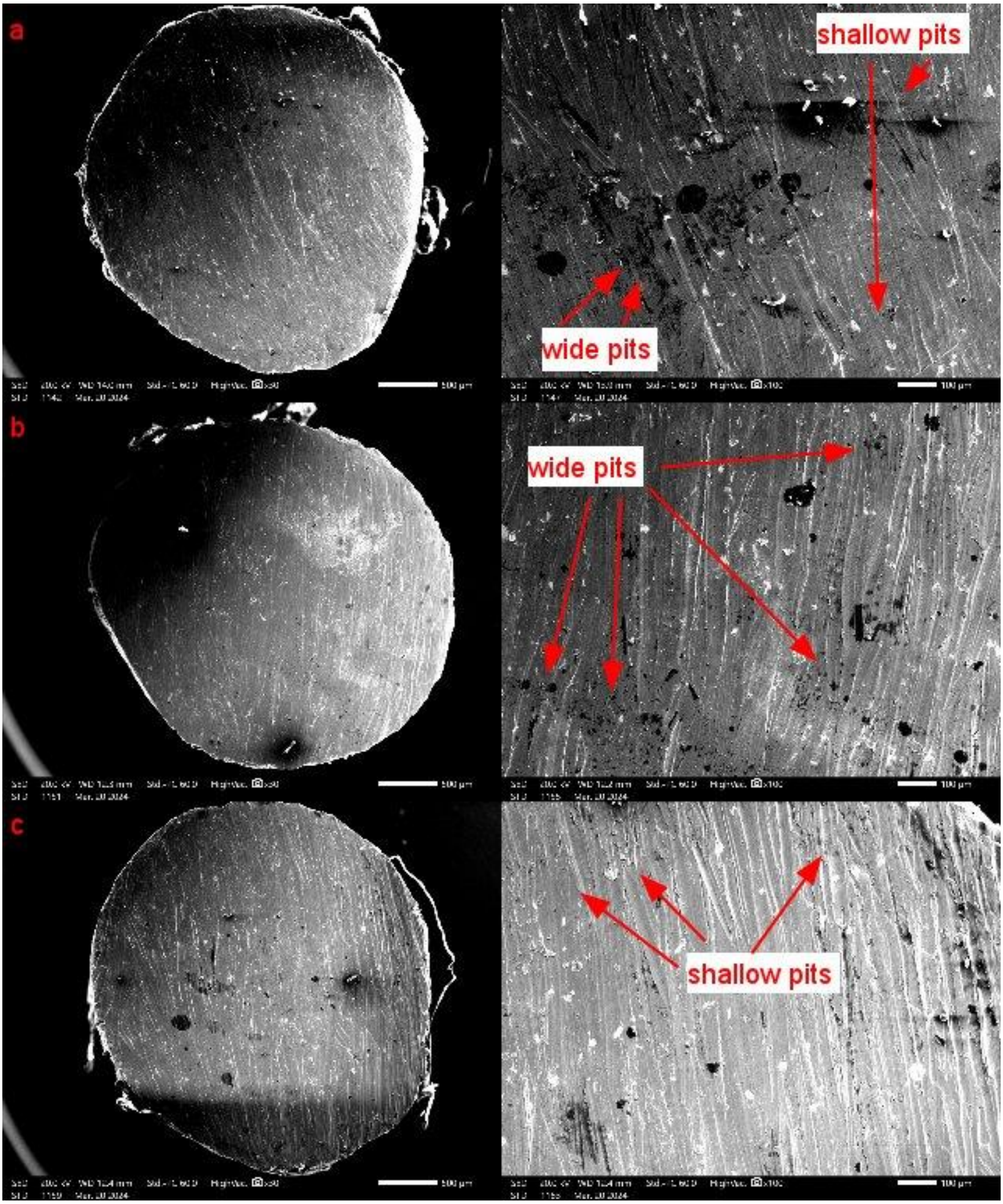

Figure 4.27: Surface morphology after corrosion tests of the Ti-6Al-4V-Ta samples

4.6 Bacteria adehesion

In order to clarify the capacity of bacterial strains frequently linked to healthcare conditions, S. aureus, P. aeruginosa, and E. coli (DH5α) were grown on 3D-printed Ti-6Al-4V metal cubes.

		Ti–6Al–4V ELI			
		E.coli	*P. aeruginosa*	*S. aureus*	*B. subtilis*
Gyroid 40% density	**Bright Field**	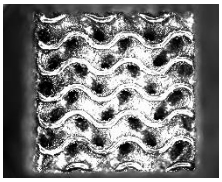	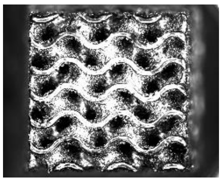	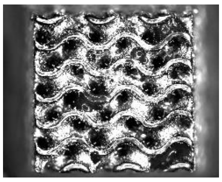	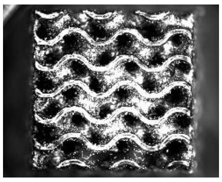
	Crystal Violet	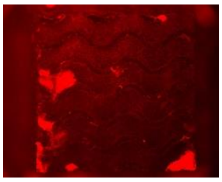	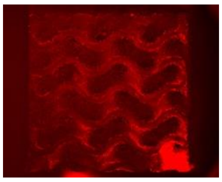	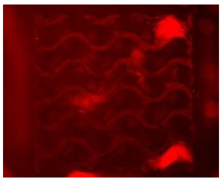	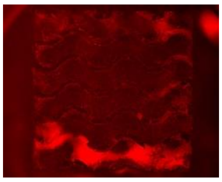
	Merged	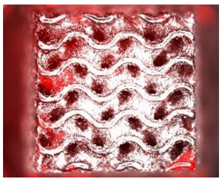	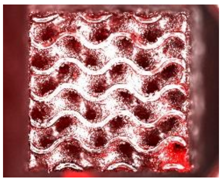	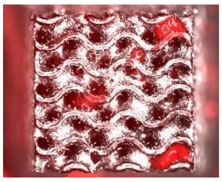	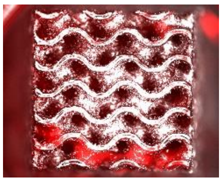
Primitive 40% density	**Bright Field**	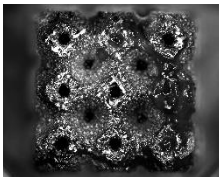	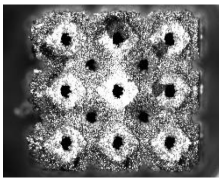	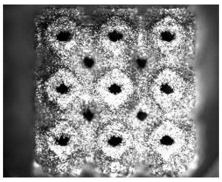	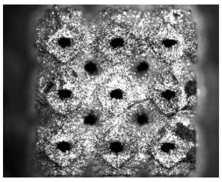
	Crystal Violet	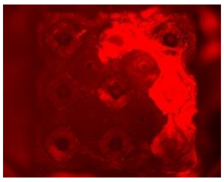	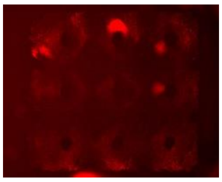	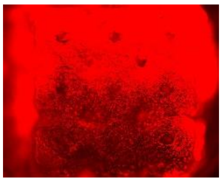	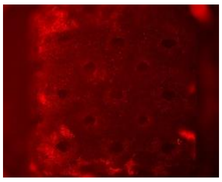
	Merged	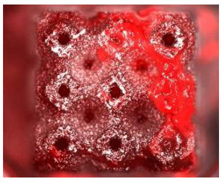	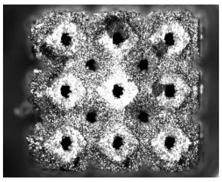	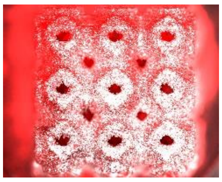	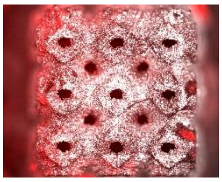

		Ti–6Al–4V-Ta			
		E.coli	***P.aeruginosa***	***S.aureus***	***B.subtilis***
Gyroid 40% density	**Bright Field**	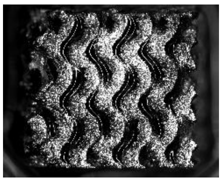	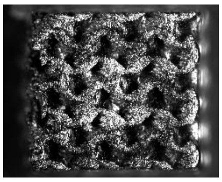	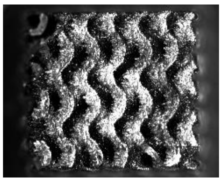	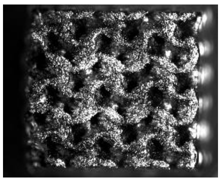
	Crystal Violet	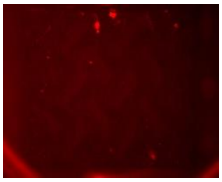	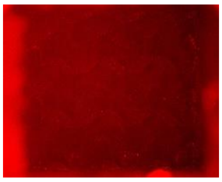	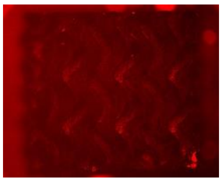	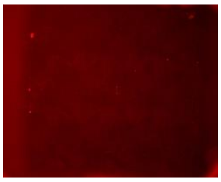
	Merged	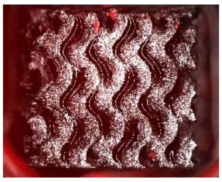			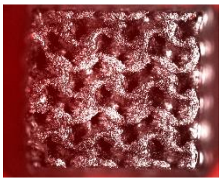
Primitive 40% density	**Bright Field**	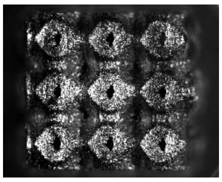	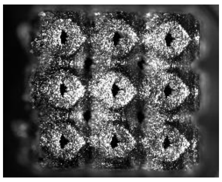	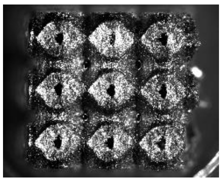	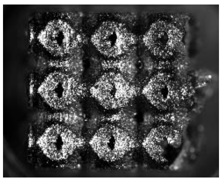
	Crystal Violet	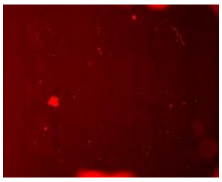	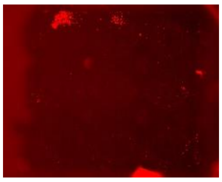	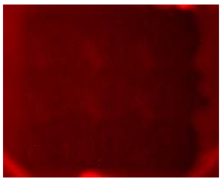	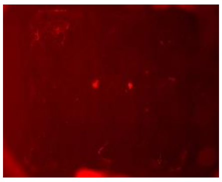
	Merged	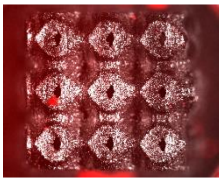	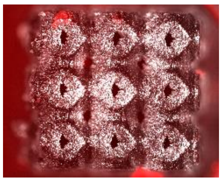	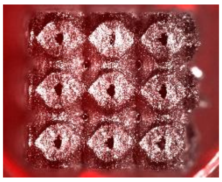	

As a benign control bacterium, Bacillus subtilis was included. It is commonly found in soil and other gastrointestinal settings. Two different surface topologies were examined: the Primitive 40% density and the Gyroid 40% density, with and without an 8% Ta (titanium acid) coating. Bacterial adhesion was more likely on the Primitive 40% and Gyroid 40% Ti-6Al-4V surfaces, according to quantitative research using crystal violet staining. Furthermore, a topology-specific interaction was found to affect bacterial adherence: Staphylococcus aureus formed slightly more biofilms on Primitive 40% density surfaces, whereas Bacillus subtilis accumulated more biofilms on Gyroid 40% density surfaces (Figure 4.28–4.29). This implies that depending on the type of bacterium, the more complex gyroid structures may have a specific effect on biofilm formation. This variation indicates that surface topography may be crucial in the bacterial colonization of medical device materials and emphasizes the complex nature of biofilm formation dynamics.

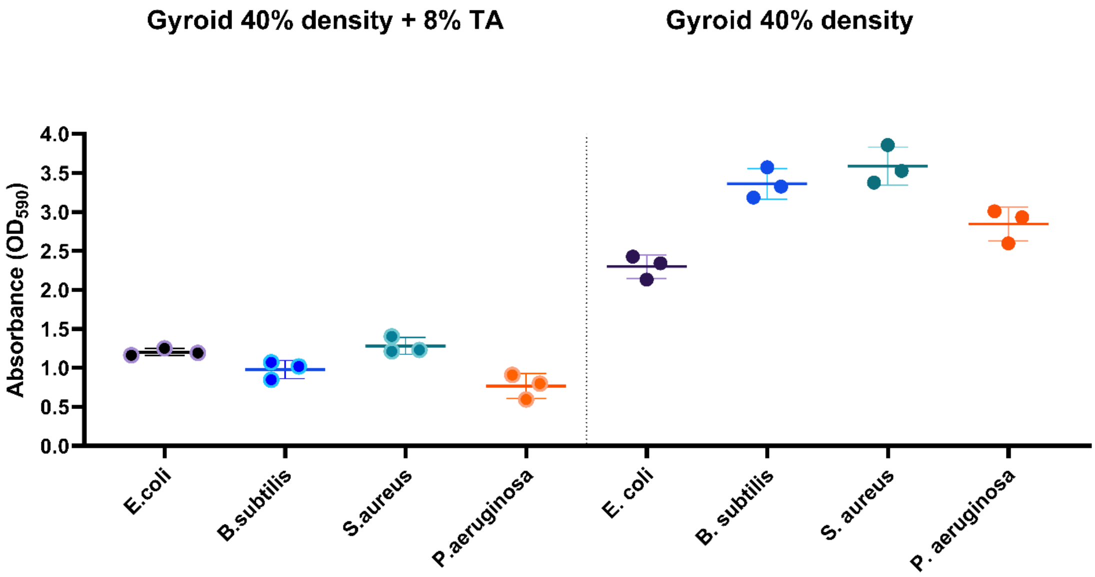

Figure 4.28: Biofilm formation on Gyroid 40% Ti-6Al-4V with and without Ta

The titanium alloy surfaces with and without the 8% Ta augmentation showed that the Ta-modified surfaces generally had less biofilm development. This result was similar for every strain of bacteria examined, suggesting that Ta may prevent the formation of biofilms on certain metal alloys. Ta's anti-biofilm capabilities were found to be surface-dependent, as evidenced by the considerable reduction in biofilm development seen in the presence of Ta for Pseudomonas aeruginosa on Gyroid 40% density surfaces.

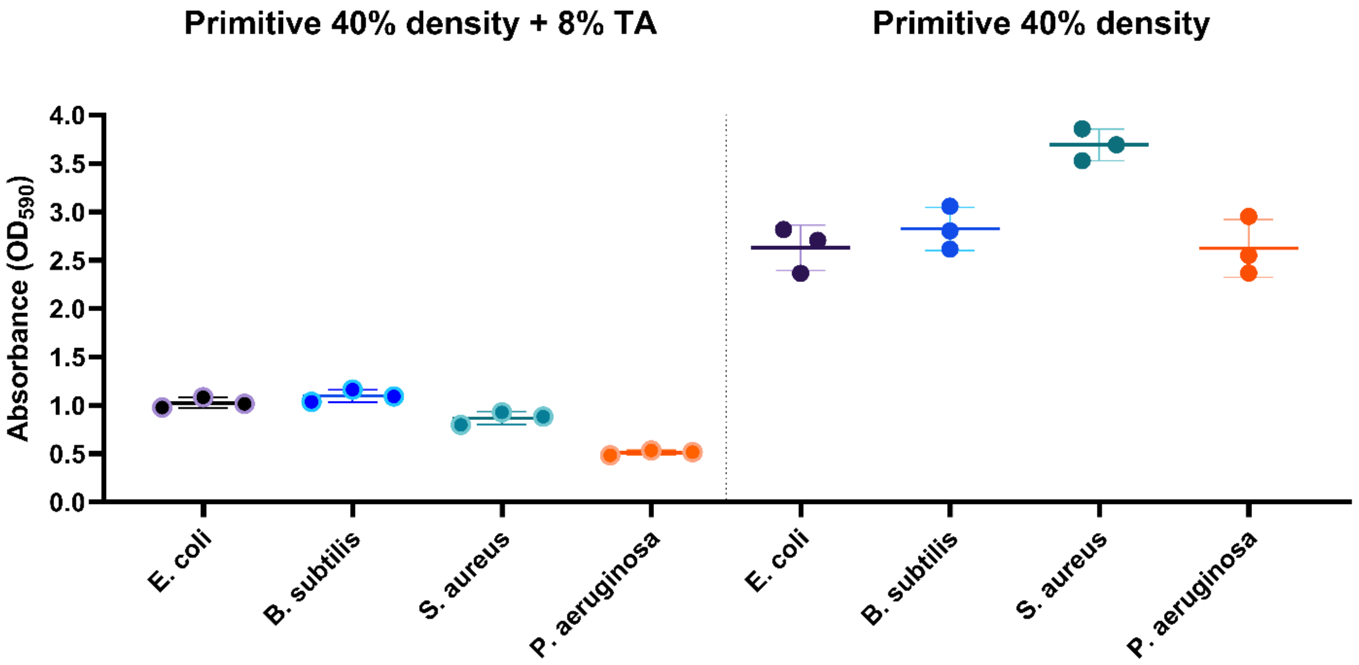

Figure 4.29: Biofilm formation on Primitive 40% Ti-6Al-4V with and without Ta

In conclusion, the data point to the importance of surface topology and Ta treatment in the development of biofilms. The Gyroid 40% density surfaces' more extensive surface area and intricacy may allow them to withstand higher levels of bacterial adherence than the Primitive 40% surfaces. On Ti-6Al-4V implants, however, the application of an 8% Ta coating reduces this impact, providing a potential way of preventing biofilm formation. More investigation is necessary to determine the medical significance of these findings in the context of controlling infections and to investigate the molecular foundations of these findings.

Chapter 6 – Conclusion

In this study, TPMS lattice structures such as Diamond, Gyroid, and Primitive were generated by MSLattice software and then printed by SLM printer for initial investigation of mechanical properties and characteristics of Ti–6Al–4V ELI and Ti-6Al-4V-Ta. Also, dense Ti-6Al-4V specimens were studied for mechanical properties, hardness, corrosion test, bacteria adhesion, fractography, and morphology under SEM. The main findings of the experiment are as follows:

• The DTi's tensile test results of Ti-6Al-4V revealed a UTS of 1241.58±23.92 MPa, a YS of 1151±8.6 MPa, and an Elastic Modulus of 116.63±4.35 GPa. According to the tensile test findings of the as-built Ti-6Al-4V-Ta samples, the ultimate tensile strength was 1212.96±5.23 MPa, its yield strength was 974.55±4.96 MPa, and its elastic modulus was 180.24±1.27 GPa. It is evident from Figure 4.10 that adding Ta to Ti–6Al–4V reduces Ultimate and Yield stress levels while increasing Elastic Modulus in the tensile test results between Ti-6Al–4V and Ti–6Al–4V-Ta dense components. The crack surface of DTi after tension displayed various features, such as pores, dimples, tear ridges, and cleavage in the fracture pattern after mechanical testing. Comparing the surface morphology of the specimens made of Ti-6Al-4v and Ti-6Al-4V-Ta reveals that the surface of bulks composed of Ti-6Al-4V-Ta has a sufficiently porous surface than Ti-6Al-4V, suggesting that they have more ductile and less brittle qualities than those without Ta. The hardness of DTi for Ti-6Al-4V alloy in this experiment was 437.75±9.91 HV and 397.01±1.43 HV for specimens with 0° and 90° printing angles, respectively. In contrast, the average hardness values of Ti-6Al-4V-Ta are 428.79±5.15 HV at 0 degrees and 391.46±2.38 HV at 90 degrees, respectively. Hence, adding Ta decreased the hardness but with a slight difference.

• A foray into the mechanical realm revealed that the Gyroid and Primitive lattice structures, at a judicious 40% density, stand out with their superior ultimate compressive strength, marking a significant stride towards emulating the biomechanical harmony of bone. This is complemented by a detailed examination of fracture surfaces through the discerning lens of SEM, where the interplay of ductility and strength was theatrically displayed in the aftermath of tensile stresses. The elastic modulus of the Ti-6Al-4V + 8% Ta structures fluctuates across a more extensive range. For example, compared to its pure Ti-6Al-4V cousin, the Elastic Modulus (4.03 GPa) of the Primitive arrangement at 40% density with Ta addition is much greater. This implies a stiffer material, which, given the potential for stress shielding, would be less appropriate for use in particular implant applications. For instance, the Gyroid arrangement at 40% density notably improves energy absorption (34.75 MJ/m^3) compared to its pure Ti-6Al-4V equivalents. Therefore, it implies that the Ta alloying enhances the material's energy dissipation capacity, a desirable quality for implants that tolerate dynamic loads. In addition, Ti-6Al-4V-Ta raises the plateau stress, a measurement of the stress at which a material deforms plastically under continuous load. For example, the Gyroid structure with 40% density with Ta shows more significant plateau stress (143.24 MPa) than pure Ti-6Al-4V structures. Therefore, the alloyed material may tolerate higher stresses before permanent deformation occurs.

- The Ti-6Al-4V-8Ta alloy is more corrosion-resistant than the Ti-6Al-4V alloy, most likely due to the passivity and oxide layer stabilization caused by tantalum. Examining the SEM pictures of the two alloys following corrosion testing demonstrates this. The Ti-6Al-4V-8Ta samples are less susceptible to localized corrosive effects since the micrographs reveal fewer pits and smaller pit diameters than those of the Ti-6Al-4V samples. Ti-6Al-4V-8Ta alloy is now considered a superior choice for these critical applications since it has a longer service life and less chance of corrosion-related issues.
- According to biomedical response research, Ta treatment and surface topology play a significant role in the production of biofilms. The Gyroid 40% density surfaces' more significant surface area and intricacy may allow them to withstand higher levels of bacterial adherence than the Primitive 40% surfaces. On Ti-6Al-4V implants, however, the application of an 8% Ta coating seems to reduce this impact, providing a potential way of preventing biofilm formation. More investigation is necessary to determine the biological significance of these findings in the context of infection management and to investigate the molecular foundations of these discoveries.
- Overall, this thesis offers critical new insights into developing next-generation implant materials, making a substantial contribution to the rapidly expanding field of additive manufacturing for medical purposes. The results open new directions for materials science and biomedical engineering research and development and better patient outcomes through improved implant designs. This study represents a significant advancement in the ongoing effort to revolutionize implant technology.

Future Works

- For further development, this study needs more investigations despite these encouraging outcomes. In order to improve the accuracy and consistency of the implants, further research may investigate the improvement of SLM process parameters. Furthermore, broadening the scope of biocompatibility testing to incorporate prolonged in vivo investigations would offer a more profound understanding of how the alloys function inside a living thing over protracted periods. It is essential to carefully assess the possible effects of increasing the production of Ti-6Al-4V-Ta alloy implants on the environment and the economy to ensure that these cutting-edge materials' advantages can be realized economically and sustainably. Nevertheless, heat treatment and microstructural analysis studies are other experimental work that must be covered. Also, to fully understand biomedical response investigations, this study suggests further investigation covering Cell Culture analysis.

References

[1] N. Soro, H. Attar, E. Brodie, M. Veidt, A. Molotnikov, and M. S. Dargusch, “Evaluation of the mechanical compatibility of additively manufactured porous Ti–25Ta alloy for load-bearing implant applications,” *Journal of the Mechanical Behavior of Biomedical Materials*, vol. 97, pp. 149–158, Sep. 2019, doi: https://doi.org/10.1016/j.jmbbm.2019.05.019.

[2]V. S. A. Challa, S. Mali, and R. D. K. Misra, “Reduced toxicity and superior cellular response of preosteoblasts to Ti-6Al-7Nb alloy and comparison with Ti-6Al-4V,” *Journal of Biomedical Materials Research Part A*, vol. 101A, no. 7, pp. 2083–2089, Jan. 2013, doi: https://doi.org/10.1002/jbm.a.34492.

[3] Y. Zhang *et al.*, “Effect of vanadium released from micro-arc oxidized porous Ti6Al4V on biocompatibility in orthopedic applications,” *Colloids and Surfaces B: Biointerfaces*, vol. 169, pp. 366–374, Sep. 2018, doi: https://doi.org/10.1016/j.colsurfb.2018.05.044.

[4] E. Chlebus, B. Kuźnicka, T. Kurzynowski, and B. Dybała, “Microstructure and mechanical behaviour of Ti—6Al—7Nb alloy produced by selective laser melting,” *Materials Characterization*, vol. 62, no. 5, pp. 488–495, May 2011, doi: https://doi.org/10.1016/j.matchar.2011.03.006.

[5] Y. Li, C. Yang, H. Zhao, S. Qu, X. Li, and Y. Li, “New Developments of Ti-Based Alloys for Biomedical Applications,” *Materials*, vol. 7, no. 3, pp. 1709–1800, Mar. 2014, doi: https://doi.org/10.3390/ma7031709.

[6] A. Lúcia, P. Hammer, Luis Geraldo Vaz, and L. A. Rocha, “Are new TiNbZr alloys potential substitutes of the Ti6Al4V alloy for dental applications? An electrochemical corrosion study,” *Biomedical Materials*, vol. 8, no. 6, pp. 065005–065005, Nov. 2013, doi: https://doi.org/10.1088/1748-6041/8/6/065005.

[7] [20] S. Suresh, C.-N. Sun, S. Tekumalla, V. Rosa, S. M. Ling Nai, and R. C. W. Wong, “Mechanical properties and in vitro cytocompatibility of dense and porous Ti–6Al–4V ELI manufactured by selective laser melting technology for biomedical applications,” Journal of the Mechanical Behavior of Biomedical Materials, vol. 123, p. 104712, Nov. 2021, doi: https://doi.org/10.1016/j.jmbbm.2021.104712.

[8] S. L. Sing, F. E. Wiria, and W. Y. Yeong, “Selective laser melting of titanium alloy with 50 wt% tantalum: Effect of laser process parameters on part quality,” *International Journal of Refractory Metals and Hard Materials*, vol. 77, pp. 120–127, Dec. 2018, doi: https://doi.org/10.1016/j.ijrmhm.2018.08.006.

[9] J. Ureña *et al.*, “Role of beta-stabilizing elements on the microstructure and mechanical properties evolution of modified PM Ti surfaces designed for biomedical applications,” *Powder Metallurgy*, vol. 61, no. 2, pp. 90–99, Jan. 2018, doi: https://doi.org/10.1080/00325899.2018.1426185.

[10] S. L. Sing, F. E. Wiria, and W. Y. Yeong, “Selective laser melting of lattice structures: A statistical approach to manufacturability and mechanical behavior,” *Robotics and Computer-Integrated Manufacturing*, vol. 49, pp. 170–180, Feb. 2018, doi: https://doi.org/10.1016/j.rcim.2017.06.006.

[11] M. Geetha, A. K. Singh, R. Asokamani, and A. K. Gogia, “Ti based biomaterials, the ultimate choice for orthopaedic implants – A review,” *Progress in Materials Science*, vol. 54, no. 3, pp. 397–425, May 2009, doi: https://doi.org/10.1016/j.pmatsci.2008.06.004.

[12] A. Basalah, “Additive Manufacturing of Porous Titanium Structures for Use in Orthopaedic Implants,” *uwspace.uwaterloo.ca*, Aug. 04, 2015. http://hdl.handle.net/10012/9499 (accessed Aug. 28, 2023).

[13] N. Taniguchi *et al.*, “Effect of pore size on bone ingrowth into porous titanium implants fabricated by additive manufacturing: An in vivo experiment,” *Materials Science and Engineering: C*, vol. 59, pp. 690–701, Feb. 2016, doi: https://doi.org/10.1016/j.msec.2015.10.069.

[14] S. Kanagaraja, A. Wennerberg, C. Eriksson, and H. Nygren, “Cellular reactions and bone apposition to titanium surfaces with different surface roughness and oxide thickness cleaned by oxidation,” *Biomaterials*, vol. 22, no. 13, pp. 1809–1818, Jul. 2001, doi: https://doi.org/10.1016/s0142-9612(00)00362-8.

[15] C. Li *et al.*, “Architecture design of periodic truss-lattice cells for additive manufacturing,” *Additive Manufacturing*, vol. 34, p. 101172, Aug. 2020, doi: https://doi.org/10.1016/j.addma.2020.101172.

[16] A. Dehghan-Manshadi, J. Venezuela, A. G. Demir, Q. Ye, and M. S. Dargusch, “Additively manufactured Fe-35Mn-1Ag lattice structures for biomedical applications,” *Journal of Manufacturing Processes*, vol. 80, pp. 642–650, Aug. 2022, doi: https://doi.org/10.1016/j.jmapro.2022.06.010.

[17] F. S. L. Bobbert *et al.*, “Additively manufactured metallic porous biomaterials based on minimal surfaces: A unique combination of topological, mechanical, and mass transport properties,” *Acta Biomaterialia*, vol. 53, pp. 572–584, Apr. 2017, doi: https://doi.org/10.1016/j.actbio.2017.02.024.

[18]S. Van Bael *et al.*, “The effect of pore geometry on the in vitro biological behavior of human periosteum-derived cells seeded on selective laser-melted Ti6Al4V bone scaffolds,” *Acta Biomaterialia*, vol. 8, no. 7, pp. 2824–2834, Jul. 2012, doi: https://doi.org/10.1016/j.actbio.2012.04.001.

[19]F. Deng, L. Liu, Z. Li, and J. Liu, “3D printed Ti6Al4V bone scaffolds with different pore structure effects on bone ingrowth,” *Journal of Biological Engineering*, vol. 15, no. 1, Jan. 2021, doi: https://doi.org/10.1186/s13036-021-00255-8.

[20]C. Yan, L. Hao, A. Hussein, and P. Young, “Ti–6Al–4V triply periodic minimal surface structures for bone implants fabricated via selective laser melting,” *Journal of the Mechanical Behavior of Biomedical Materials*, vol. 51, pp. 61–73, Nov. 2015, doi: https://doi.org/10.1016/j.jmbbm.2015.06.024.

[21]D. Zhao *et al.*, “Effect of pore geometry on the fatigue properties and cell affinity of porous titanium scaffolds fabricated by selective laser melting,” *Journal of the Mechanical Behavior of Biomedical Materials*, vol. 88, pp. 478–487, Dec. 2018, doi: https://doi.org/10.1016/j.jmbbm.2018.08.048.

[22]G. Yu *et al.*, “The select of internal architecture for porous Ti alloy scaffold: A compromise between mechanical properties and permeability,” *Materials & Design*, vol. 192, p. 108754, Jul. 2020, doi: https://doi.org/10.1016/j.matdes.2020.108754.

[23]W. Wei-hui, Y. Yong-qiang X. Dong-ming, C. Chang-yong, and M. Gui-sheng, “Pore forming results of controllable ultra-light structured parts by selective laser melting,” *Optics and Precision Engineering*, vol. 25, no. 6, pp. 1547–1556, 2017, doi: https://doi.org/10.3788/ope.20172506.1547.

[24] C. Song et al., “Research progress on the design and performance of porous titanium alloy bone implants,” Journal of Materials Research and Technology, vol. 23, pp. 2626–2641, Mar. 2023, doi: https://doi.org/10.1016/j.jmrt.2023.01.155.

[25] H. Chen, Q. Han, C. Wang, Y. Liu, B. Chen, and J. Wang, “Porous Scaffold Design for Additive Manufacturing in Orthopedics: A Review,” *Frontiers in Bioengineering and Biotechnology*, vol. 8, Jun. 2020, doi: https://doi.org/10.3389/fbioe.2020.00609.

[26] O. Al-Ketan, R. Rowshan, and R. K. Abu Al-Rub, “Topology-mechanical property relationship of 3D printed strut, skeletal, and sheet based periodic metallic cellular materials,” *Additive Manufacturing*, vol. 19, pp. 167–183, Jan. 2018, doi: https://doi.org/10.1016/j.addma.2017.12.006.

[27] L. J. Gibson, “Cellular Solids,” *MRS Bulletin*, vol. 28, no. 4, pp. 270–274, Apr. 2003, doi: https://doi.org/10.1557/mrs2003.79.

[28] H. Lee, C. H. J. Lim, M. J. Low, N. Tham, V. M. Murukeshan, and Y.-J. Kim, “Lasers in additive manufacturing: A review,” *International Journal of Precision Engineering and Manufacturing-Green Technology*, vol. 4, no. 3, pp. 307–322, Jul. 2017, doi: https://doi.org/10.1007/s40684-017-0037-7.

[29] T. Maconachie *et al.*, “SLM lattice structures: Properties, performance, applications and challenges,” *Materials & Design*, vol. 183, p. 108137, Dec. 2019, doi: https://doi.org/10.1016/j.matdes.2019.108137.

[30] H.-J. Wilke and D. Volkheimer, “Basic Biomechanics of the Lumbar Spine,” *Biomechanics of the Spine*, pp. 51–67, 2018, doi: https://doi.org/10.1016/b978-0-12-812851-0.00004-5.

[31] W. M. Kohrt, A. A. Ehsani, and S. J. Birge, “Effects of Exercise Involving Predominantly Either Joint-Reaction or Ground-Reaction Forces on Bone Mineral Density in Older Women,” *Journal of Bone and Mineral Research*, vol. 12, no. 8, pp. 1253–1261, Aug. 1997, doi: https://doi.org/10.1359/jbmr.1997.12.8.1253.

[32] C. Chua, S. L. Sing, and C. K. Chua, “Finite element analysis on titanium-tantalum lattice structures fabricated using selective laser melting,” *Materials Today: Proceedings*, Oct. 2022, doi: https://doi.org/10.1016/j.matpr.2022.09.619.

[33] C. Chua, S. L. Sing, and C. K. Chua, “Characterisation of in-situ alloyed titanium-tantalum lattice structures by laser powder bed fusion using finite element analysis,” *Virtual and Physical Prototyping*, vol. 18, no. 1, Nov. 2022, doi: https://doi.org/10.1080/17452759.2022.2138463.

[34] C. Shang, X. Hou, Y. Lu, R. Zhang, X. Lu, and C. Yuan, “Simultaneous improvement of strength and ductility of laser additively produced Ti6Al4V by adding tantalum,” Journal of Alloys and Compounds, vol. 976, pp. 173171–173171, Mar. 2024, doi: https://doi.org/10.1016/j.jallcom.2023.173171.

[35] S. Van Bael et al., “The effect of pore geometry on the in vitro biological behavior of human periosteum-derived cells seeded on selective laser-melted Ti6Al4V bone scaffolds,” Acta Biomaterialia, vol. 8, no. 7, pp. 2824–2834, Jul. 2012, doi: https://doi.org/10.1016/j.actbio.2012.04.001.

[36] F. Deng, L. Liu, Z. Li, and J. Liu, “3D printed Ti6Al4V bone scaffolds with different pore structure effects on bone ingrowth,” Journal of Biological Engineering, vol. 15, no. 1, Jan. 2021, doi: https://doi.org/10.1186/s13036-021-00255-8.

[37] C. Yan, L. Hao, A. Hussein, and P. Young, “Ti–6Al–4V triply periodic minimal surface structures for bone implants fabricated via selective laser melting,” Journal of the Mechanical Behavior of Biomedical Materials, vol. 51, pp. 61–73, Nov. 2015, doi: https://doi.org/10.1016/j.jmbbm.2015.06.024.

[38] D. Zhao et al., “Effect of pore geometry on the fatigue properties and cell affinity of porous titanium scaffolds fabricated by selective laser melting,” Journal of the Mechanical Behavior of Biomedical Materials, vol. 88, pp. 478–487, Dec. 2018, doi: https://doi.org/10.1016/j.jmbbm.2018.08.048.

[39] G. Yu et al., “The select of internal architecture for porous Ti alloy scaffold: A compromise between mechanical properties and permeability,” Materials & Design, vol. 192, p. 108754, Jul. 2020, doi: https://doi.org/10.1016/j.matdes.2020.108754.

[40] W. Wei-hui, Y. Yong-qiang X. Dong-ming, C. Chang-yong, and M. Gui-sheng, “Pore forming results of controllable ultra-light structured parts by selective laser melting,” Optics and Precision Engineering, vol. 25, no. 6, pp. 1547–1556, 2017, doi: https://doi.org/10.3788/ope.20172506.1547.

[41] C. Song et al., “Research progress on the design and performance of porous titanium alloy bone implants,” Journal of Materials Research and Technology, vol. 23, pp. 2626–2641, Mar. 2023, doi: https://doi.org/10.1016/j.jmrt.2023.01.155.

[42] T. Yang *et al.*, “Laser powder bed fusion of AlSi10Mg: Influence of energy intensities on spatter and porosity evolution, microstructure and mechanical properties,” *Journal of Alloys and Compounds*, vol. 849, p. 156300, Dec. 2020, doi: https://doi.org/10.1016/j.jallcom.2020.156300.

[43] L. Xue et al., “Controlling martensitic transformation characteristics in defect-free NiTi shape memory alloys fabricated using laser powder bed fusion and a process optimization framework,” Acta Materialia, vol. 215, p. 117017, Aug. 2021, doi: https://doi.org/10.1016/j.actamat.2021.117017.

[44] R. Wauthle *et al.*, “Additively manufactured porous tantalum implants,” *Acta Biomaterialia*, vol. 14, pp. 217–225, Mar. 2015, doi: https://doi.org/10.1016/j.actbio.2014.12.003.\

[45] A. Sharma, M. C. Oh, J.-T. Kim, A. K. Srivastava, and B. Ahn, “Investigation of electrochemical corrosion behavior of additive manufactured Ti–6Al–4V alloy for medical implants in different electrolytes,” Journal of Alloys and Compounds, vol. 830, p. 154620, Jul. 2020, doi: https://doi.org/10.1016/j.jallcom.2020.154620.